Chair of Functional Materials and Materials Systems

Doctoral Thesis
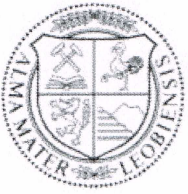
Novel Multifunctional Coatings for Advanced Tribological Applications

Dipl.-Ing. Nikolaus Jäger

December 2020

MONTANUNIVERSITÄT LEOBEN

www.unileoben.ac.at

EIDESSTATTLICHE ERKLÄRUNG

I declare on oath that I wrote this thesis independently, did not use other than the specified sources and aids, and did not otherwise use any unauthorized aids.

I declare that I have read, understood, and complied with the guidelines of the senate of the Montanuniversität Leoben for "Good Scientific Practice".

Furthermore, I declare that the electronic and printed version of the submitted thesis are identical, both, formally and with regard to content.

Datum 07.12.2020

_____
Signature Author
Nikolaus Jäger

Acknowledgements

Abstract

Hard, wear-resistant coatings for the protection of surfaces exposed to wear have been in the focus of research for several decades. However, ever-increasing demands in modern machining applications like high-speed cutting or dry-cutting require advanced coating materials with extraordinary properties. Besides the mechanical properties, thermal stability and resistance against corrosion and oxidation are of utmost importance, as the coatings regularly face very high temperatures above 1000 °C during operation. Within the scope of this thesis, several novel multifunctional coatings with specific compositional, microstructural and residual stress designs were developed and investigated by modern, advanced characterization methods.

In a first approach, alternating layers of hard $Al_{70}Cr_{30}N$ with cubic, and soft $Al_{90}Cr_{10}N$ with hexagonal crystal structure were combined in a multi-layered coating with specific architecture. The coating was studied in the as-deposited state and after vacuum annealing at 1000 °C by cross-sectional X-ray nanodiffraction in order to access the microstructure, texture, phase composition and residual stress state and their changes upon annealing. The results reveal the influence of the complex coating architecture as the columnar grain growth is interrupted at the interfaces of layers exhibiting different phases, the decomposition of the metastable cubic phase is governed and a residual stress depth distribution with pronounced stress gradients is formed.

The second approach is based on nanocomposite coatings consisting of immiscible nitrides. Three AlCr(Si)N coatings with Si-contents of 0 at.%, 2.5 at.% and 5 at.% Si were synthesized and investigated regarding their thermal stability by in-situ high-temperature high-energy grazing incidence transmission X-ray diffraction. The results reveal a change from a columnar to a nanocomposite microstructure, a diminished decomposition of CrN into Cr_2N and an increase of lattice defects accompanied by higher compressive residual stress with increasing Si-content. Furthermore, the addition of Si to AlCrN resulted in enhanced mechanical properties at elevated temperatures, demonstrated by an increase in hardness of the Si-containing coatings, while the hardness for AlCrN decreased after annealing.

Finally, the oxidation behavior of the nanocomposite AlCr(Si)N coatings was investigated by

differential scanning calorimetry, thermogravimetric analysis and ex-situ X-ray diffraction. The results reveal an improved oxidation behavior with increasing Si-content by a retarded onset of oxidation to higher temperatures from 1100 °C to 1260 °C and a simultaneously decelerated oxidation process. Additionally, a sample of the AlCrSiN coating with 5 at.% Si was partially oxidized by annealing it at 1400 °C in ambient air to study the elemental and structural changes along the coating thickness by scanning transmission electron microscopy and cross-sectional X-ray nanodiffraction. Outwards diffusion of Cr, Al and Si to the surface and inward diffusion of oxygen resulted in the development of three zones throughout the coating. An oxide layer consisting of an Al-rich and a Cr-rich part formed at the very top, followed by a transition zone with fine grains and incomplete oxidation and a non-oxidized zone depleted of Cr underneath.

Overall, this thesis presents several successful attempts to improve the mechanical properties, thermal stability and oxidation behavior of wear-protective coatings by sophisticated microstructural and compositional designs. The results establish a deeper understanding of the process–structure–property correlations of coatings with a complex, multi-layered architecture or a nanocomposite structure. Simultaneously, the study points out the necessity of advanced, position resolved and in-situ characterization techniques for the analysis of coatings with structural and compositional heterogeneities.

Kurzfassung

Beschichtungen zum Schutz von verschleißbeanspruchten Oberflächen stehen seit mehreren Jahrzehnten im Fokus der Forschung. Die steigenden Anforderungen in modernen Zerspanungsanwendungen wie Hochgeschwindigkeits- oder Trockenzerspanung erfordern jedoch fortschrittliche Beschichtungswerkstoffe mit außergewöhnlichen Eigenschaften. Neben den mechanischen Eigenschaften sind die thermische Stabilität und die Beständigkeit gegen Korrosion und Oxidation von größter Bedeutung, da die Beschichtungen während der Anwendung regelmäßig hohen Temperaturen von über $1000\,°C$ ausgesetzt sind. Im Rahmen dieser Arbeit wurden verschiedene multifunktionelle Beschichtungen entwickelt und mit modernen Charakterisierungsmethoden untersucht.

In einem ersten Ansatz wurden abwechselnd harte $Al_{70}Cr_{30}N$-Lagen und weiche $Al_{90}Cr_{10}N$-Lagen in einer mehrlagigen Beschichtung mit spezifischer Architektur kombiniert. Die Beschichtung wurde im abgeschiedenen Zustand und nach einer Glühung im Vakuum bei $1000\,°C$ mittels Röntgen-Nanodiffraktion positionsaufgelöst über die Schichtdicke untersucht, um die Mikrostruktur sowie den Eigenspannungszustand und deren Veränderungen nach dem Glühen zu ermitteln. Die Ergebnisse zeigen den Einfluss der komplexen Beschichtungsarchitektur auf die Mirkostuktur durch eine Unterbrechung des Kornwachstums an den Grenzflächen der Einzellagen mit unterschiedlicher Kristallstruktur und durch die Ausbildung eines komplexen Eigenspannungsverlaufs über die Schichtdicke.

Der zweite Ansatz beruht auf Beschichtungen mit Nanokompositstruktur auf Basis von nicht mischbaren Nitriden. Es wurden drei AlCr(Si)N-Schichten mit Si-Gehalten von $0\,at.\%$, $2.5\,at.\%$ und $5\,at.\%$ Si synthetisiert und am Synchrotron in-situ bei Temperaturen bis zu $1100\,°C$ hinsichtlich ihrer thermischen Stabilität untersucht. Die Ergebnisse zeigen einen Wechsel der Mikrostruktur von säulenförmigen Körnern zu einem Nanokomposit, eine verminderte Zersetzung von CrN in Cr_2N und eine Zunahme von Gitterdefekten, begleitet von höheren Druckeigenspannungen mit steigendem Si-Gehalt. Darüber hinaus führte der Zusatz von Silizium zu AlCrN zu verbesserten mechanischen Eigenschaften bei hohen Temperaturen, gezeigt Anhand eines Anstiegs der Härte der Si-haltigen Schichten nach dem Glühen, während die Härte für AlCrN nach dem Glühen sank.

Darüber hinaus wurde das Oxidationsverhalten der AlCr(Si)N-Schichten untersucht. Die Ergebnisse zeigen verbesserte Oxidationseigenschaften der Schichten mit steigendem Si-Gehalt durch einen verzögerten Oxidationsbeginn und einen gleichzeitig verlangsamten Oxidationsprozess. Zusätzlich wurde eine Probe der AlCrSiN-Schicht mit 5 at.% Si teilweise oxidiert, indem sie bei 1400 °C in Luft geglüht wurde, um die Änderungen der Zusammensetzung und der Struktur positionsaufgelöst über die Schichtdicke mittels Transmissionselektronenmikroskopie und Röntgen-Nanodiffraktion zu untersuchen. Die Diffusion von Schichtelementen wie Cr, Al und Si an die Oberfläche der Schicht und die Diffusion von Sauerstoff in das Schichtmaterial hinein resultierte in drei unterschiedliche Zonen innerhalb der Schicht. An der Oberfläche bildete sich eine dichte Oxidschicht, gefolgt von einer Übergangszone mit feiner Kornstruktur und unvollständiger Oxidation, und einer nicht oxidierten, an Chrom verarmten Zone darunter.

Insgesamt werden in dieser Arbeit mehrere erfolgreiche Ansätze vorgestellt, um die mechanischen Eigenschaften, die thermische Stabilität und das Oxidationsverhalten von Verschleißschutzschichten zu verbessern. Die Ergebnisse führen zu einem tieferen Verständnis der Zusammenhänge zwischen der Synthese, der Mikrostruktur und schlussendlich den Eigenschaften von Schichtenmit komplexem Aufbau. Gleichzeitig zeigt diese Arbeit die Notwendigkeit der Verwendung von ortsaufgelösten Charakterisierungstechniken für die Analyse von Beschichtungen mit, hinsichtlich ihrer Zusammensetzung und Struktur heterogenem Schichtaufbau.

Contents

Contents

CHAPTER 1

Introduction

Hard and wear resistant coatings find widespread use for cutting tools, dies and molds. The coatings with a thickness of only a few micrometers improve the performance of those tools substantially. The first protective hard coatings introduced to the market in the early 1980s were single-phased materials like TiN, TiC and CrN [1–3]. Especially TiN is still popular as it combines good mechanical properties and wear resistance with a decorative gold colour [4]. However, with respect to enhanced production throughputs and prolonged tool lifetime with a concomitant demand to reduce costs and energy consumption, the requirements on hard and wear resistant coatings constantly increase. Nowadays, ternary nitrides, such as AlTiN or AlCrN, represent state-of-the-art materials. In these coatings, Al substitutes Ti or Cr and a favourable cubic structure is formed even at high Al concentrations, which is characterized by a high hardness and excellent wear properties [5].

Although ceramic hard coatings typically exhibit a high hardness, good wear resistance and excellent oxidation behaviour at high temperatures [6–9], they often suffer from their brittleness. Therefore, an approach for developing hard yet tough materials, which are commonly exclusive material's properties, is presented within the first part of this thesis. A multilayered AlCrN-based coating consisting of alternating hard, cubic and soft, hexagonal layers was synthesized and investigated in terms of microstructure, residual stress development and thermal stability. The strategy to combine materials varying in their mechanical properties to form damage-tolerant coatings with structural and compositional heterogeneities is inspired by nature [10, 11] as it is often observed in biological materials like wood [12], bone [13], or nacre [14]. The enhancement in fracture toughness in such materials is caused by multiple crack deflection at interfaces of constituents differing in their microstructure and physical properties [15].

The characterization of coatings with a complex, multi-layered microstructure is not straight forward and requires advanced depth resolving analysis techniques. The recently developed cross-sectional synchrotron X-ray nano-diffraction method [16, 17] was used to study the

1

multi-layered coating system depth resolved across the coating thickness with a resolution of 50 nm. Besides crystal structure, also crystallographic texture, crystallite size and the strain development of the individual components of the complex coating architecture were determined.

Not only the mechanical properties, but also the chemical and thermal stability of coatings are of utmost importance, as increasing cutting speeds and feed rates or the reduction of using harmful coolants and lubricants are coupled with increasing temperatures during advanced applications [4, 18]. To further improve the high-temperature properties of the coatings, the influence of several alloying elements in the AlTiN and AlCrN systems has been studied, mainly with the aim to stabilize the cubic phase at high temperatures in order to improve the mechanical and wear properties or to enhance the oxidation resistance of the coatings [19, 20]. A concept for thermodynamically stable superhard coatings is based on alloying Si to the AlTiN and AlCrN coating systems. As Si is immiscible in AlTiN and AlCrN, it tends to segregate along grain boundaries and a new class of coatings with a so-called nanocomposite structure is developed. These nanocomposite coatings consist of AlMeN crystallites embedded in an amorphous (a-)Si_xN_y tissue phase [21–24], and are characterized by an extraordinary high hardness, a high thermal stability and a good oxidation resistance.

The impact of Si on the microstructural evolution of the AlCr(Si)N-system and the resulting coating properties with a focus on thermal stability is presented within the second part of this thesis. For that purpose, AlCr(Si)N coatings with varying Si-content were synthesized. In a first step, the coatings were investigated by conventional differential scanning calorimetry (DSC) and thermogravimetric analysis (TGA) measurements combined with ex-situ X-ray diffraction (XRD). Additionally, the coatings were studied by the newly developed in-situ high-temperature high-energy grazing incidence transmission X-ray diffraction (HT-HE-GIT-XRD) method, providing simultaneously access to numerous temperature-dependent material properties such as microstructure, residual stress state, thermal expansion coefficient and phase stability [25, 26].

Finally, the third part of this thesis focuses on the oxidation behaviour of AlCr(Si)N coatings. Coatings with varying Si-content were investigated by DSC and TGA measurements in ambient air. Furthermore, the coating showing the highest oxidation resistance during DSC/TGA investigations was used to study local elemental and structural changes occurring during oxidation. Therefore, a partially oxidized sample was prepared and investigated along the coating cross-section by X-ray nano-diffraction and transmission electron microscopy.

Overall, the results presented in this thesis should emphasize the potential of coatings with defined multi-layered architectures and advanced alloying concepts for modern cutting and forming applications.

Coating materials

2.1 The AlCrN system

AlCrN coatings are nowadays well established in industry for advanced machining tools (e.g. dry cutting and high-speed applications), due to their excellent physical, chemical and mechanical properties [27–29]. The main advantage of AlCrN compared to AlTiN is the superior oxidation behaviour, as the formation of porous rutile-type TiO_2 is prevented and a dense Al_2O_3/Cr_2O_3 oxide layer is formed at high temperatures [7].
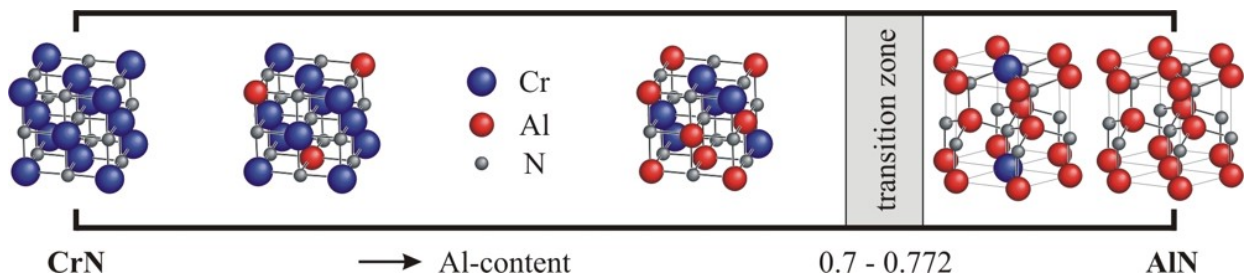
Figure 2.1: Structural development of the AlCrN-system as a function of Al-content. The fcc rock-salt structure is formed for Al-contents below ∼0.7, at high Al-contents the hexagonal wurtzite modification is obtained [5].

The crystal structure of the AlCrN system strongly depends on the Al-content, as shown in Fig. 2.1 [5] and Fig. 2.2. The stoichiometric binary CrN crystallizes in the face centered cubic (fcc) (NaCl-type) structure, where N occupies the octahedral sites of the unit cell formed by Cr [30]. AlN exhibits a hexagonal wurtzite (ZnS-type) structure. Although the quasi-binary CrN-AlN-system exhibits a large miscibility gap, AlCrN coatings can be stabilized in a fcc solid solution by physical vapor deposition (PVD) techniques, where the atomic assembly kinetics are limited as the coatings grow under highly non-equilibrium conditions [31]. Depending on the process conditions, the maximum solubility limit of Al in cubic AlCrN is about 0.7 (on the metal sublattice). At higher Al-contents, a dual phase (cubic +

hexagonal) or a pure hexagonal crystal structure is achieved (Fig. 2.2) [5, 30].
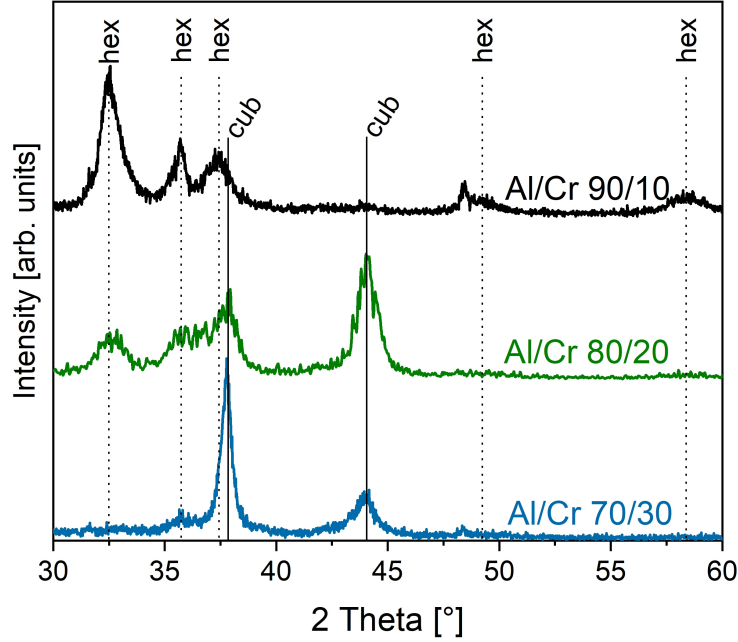
Figure 2.2: X-ray diffractograms of AlCrN coatings with varying Al/Cr ratio. A purely cubic crystal structure is obtained for the coating with the lowest Al/Cr ratio of 70/30. The amount of hexagonal phase increases with increasing Al-content. While the coating with an Al/Cr ratio of 80/20 has a dual phase structure (cubic + hexagonal), the coating with an Al/Cr ratio of 90/10 is purely hexagonal [own work].

The mechanical properties of AlCrN coatings strongly depend on their crystal structure. The hardness and elastic modulus of AlCrN coatings with different phase composition depending on their Al/Cr ratio are shown in Table 2.1. The coating with an Al/Cr ratio of 70/30 and purely cubic crystal structure has the highest hardness and elastic modulus of 33 GPa and 528 GPa, respectively. As the amount of hexagonal phase increases with increasing Al-content, hardness and elastic modulus of the coatings decrease reaching a minimum of 24 GPa and 350 GPa, respectively, for the $Al_{90}Cr_{10}N$ exhibiting a purely hexagonal crystal structure. While pure CrN decomposes in a two-step reaction into Cr_2N and finally Cr at

Table 2.1: Mechanical properties of AlCrN coatings depending on their Al/Cr ratio and the resulting crystal structure [own work].

AlCrN coating	Crystal structure	Hardness [GPa]	Elastic modulus [GPa]
$Al_{70}Cr_{30}N$	cubic	33	528
$Al_{80}Cr_{20}N$	cubic + hexagonal	26	403
$Al_{90}Cr_{10}N$	hexagonal	24	350

temperatures above 1000 °C accompanied by the release of N_2 [32], AlN is thermally stable in the hexagonal crystal structure [33]. The thermally stability of CrN can be enhanced by

alloying Al, which shifts the onset temperature of decomposition to higher temperatures, as the thermally stable AlN acts as diffusion barrier and raises the effective nitrogen partial pressure (outward diffusion of nitrogen is prohibited) [8, 9].

AlCrN coatings with optimized Al-content have good mechanical properties, a good thermal stability and a high resistance against oxidation. Besides adjusting the Al/Cr ratio of AlCrN coatings, also architectural concepts show huge potential to further improve the coatings. Especially multi-layered architectures, nanocomposite structures or micro-structural and stress design represent promising approaches for coatings with enhanced mechanical properties and thermal stability. Some of these concepts based on the AlCrN-system will be introduced in the following sections and are also subject of the publications related to this thesis.

2.2 Multi-layered coatings based on AlCrN

Multi-layered coatings are systems with two or more layers of different materials combined to a coating with a thickness of several micrometers. The typical thickness of the individual layers can range from a few nanometers (often referred as superlattices) to several micrometers, and the individual layers usually have a uniform composition. Advantages of multi-layered coatings arise from the combination of materials with different properties (e.g. combine materials with high hardness and good oxidation resistance) or from the distinct interfaces between adjacent layers. Three mechanisms can contribute to an enhancement in fracture toughness in multi-layered coatings: (1) crack deflection, (2) ductile interlayer ligament bridging, and (3) crack tip blunting (Fig. 2.3) [34]. Prerequisite to activate these mechanisms is the combination of materials differing in their microstructure and mechanical properties, especially with a large difference in elastic modulus [35, 36].
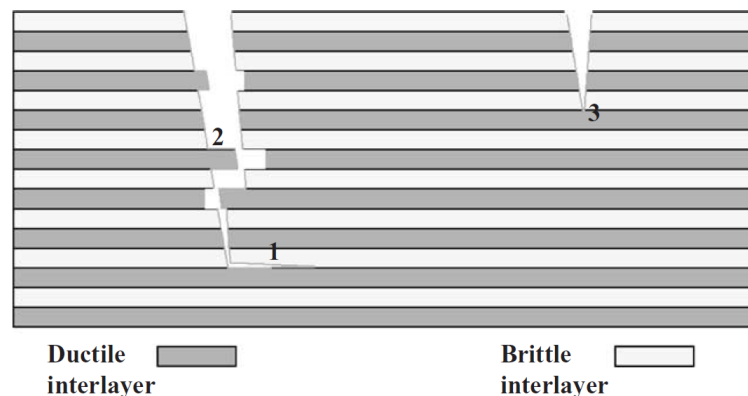
Figure 2.3: Toughening mechanisms in multi-layered coatings: (1) crack deflection, (2) ductile interlayer ligament bridging, and (3) crack tip blunting [34].

The AlCrN-system is a promising candidate for the development of damage-tolerant coat-

ings with high fracture toughness, as multi-layered coatings with hard, stiff and soft, elastic layers can be easily synthesized by only changing the Al/Cr ratio of the individual layers, as the mechanical properties of AlCrN strongly depend on its crystal structure. As mentioned before, AlCrN exhibits a high hardness and stiffness when it is cubic, and it is significantly softer and less stiff in its hexagonal modification at high Al-contents (Table 2.1). An example for such an AlCrN-based multi-layered coating is given in Fig. 2.4. The SEM micrograph shows a part of a multi-layered coating consisting of individual layers with varying Al/Cr ratio, together with the corresponding Al and Cr content obtained by energy dispersive X-ray spectroscopy (EDX). The different Al/Cr ratio results in alternating layers with hexagonal (for high Al/Cr ratios) and cubic crystal structure (for low Al/Cr ratios), respectively. While there are plenty of well-established methods to study monolithic coatings, the
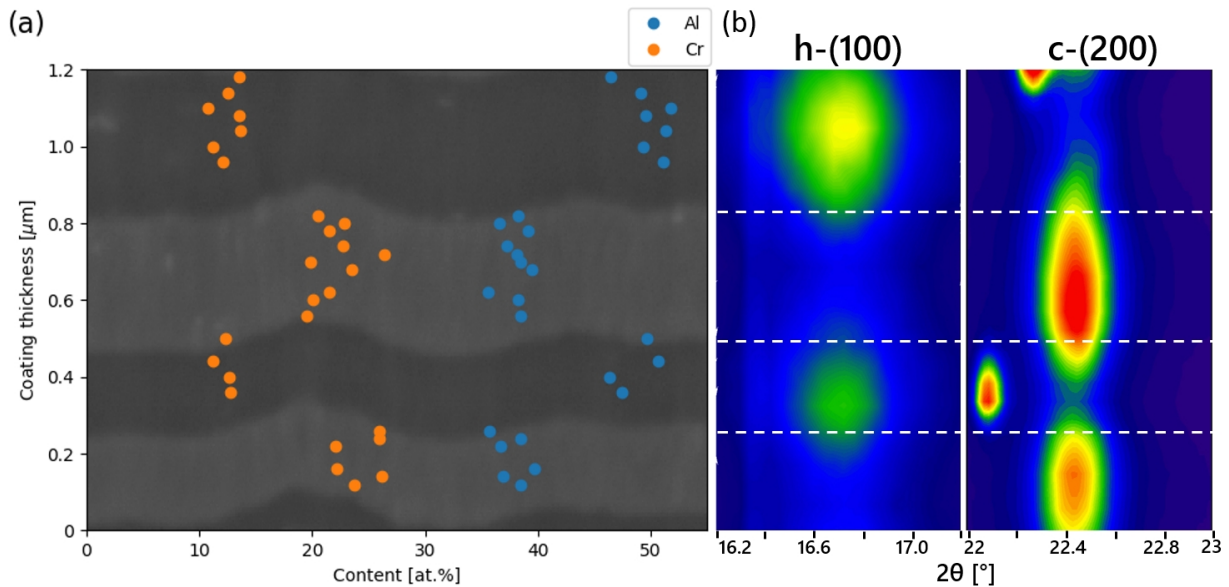
Figure 2.4: (a) SEM micrograph showing a part of an AlCrN-based multi-layered coating with four individual layers differing in their Al/Cr ratio, together with the Al and Cr content as a function of coating thickness obtained by EDX and (b) the corresponding diffraction intensity of the 100 (left) and the 200 reflection (right) stemming from the hexagonal and the cubic phase, respectively [own work].

analysis of multi-layered coatings with complex architectures and elemental and structural heterogeneities along the coating thickness is not straight forward and requires advanced, position-resolved characterization methods. Within this thesis, an approach based on the recently developed synchrotron X-ray nano-diffraction method [16] is demonstrated, where it was used to study the microstructure and residual stress development of an AlCrN-based multi-layered system [37] and of a partially oxidized nanocomposite AlCrSiN coating.

2.3   Nanocomposite coatings

A nanocomposite is defined as a heterogeneous multiphase material where at least one of the phases has dimensions in the nanometer range. Contrary to multi-layered coatings, where the different materials are stacked in layers, an example for a nanocomposite material is a comprising nanocrystallites embedded in an amorphous or quasi-amorphous matrix (schematic in Fig. 2.5). The formation of such a nanocomposite structures is principally attributed to the segregation of one phase at the grain boundaries of another phase. This may be obtained for a combination of materials exhibiting a miscibility gap in the solid state, e.g. $TiN-Si_3N_4$ [38], Ti–B–N [39] etc. Since grain growth is hindered as the second phase segregates at the grain boundaries, the individual grains are too small for Frank–Read dislocation sources to operate and plastic deformation due to multiplication, movement and pile-up of dislocations is highly limited. Thus, deformation of nanocomposite materials occurs mainly due to sliding events in the grain boundary phase [40].
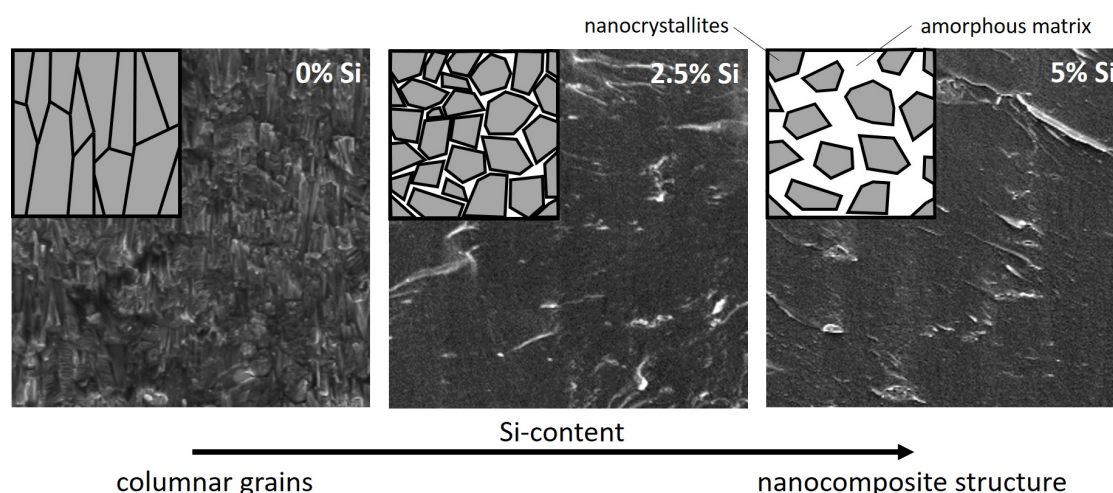
Figure 2.5: Development of the microstructure of the AlCr(Si)N system as a function of Si-content. While AlCrN exhibits a typical columnar grain morphology, a nanocomposite structure is obtained for the Si-containing coatings, resulting in a glassy and featureless fracture cross-section [own work taking into account the model of Patscheider [41]].

Besides exceptional mechanical properties, the nanocomposite microstructure may also lead to superior oxidation resistance. While a continuous diffusion path for the inward diffusion of oxygen exists along the grain boundaries of coatings with typical columnar grain morphology, this diffusion path is blocked in nanocomposite coatings by the amorphous tissue phase encapsulating the individual crystallites [42].

A nanocomposite microstructure can develop in the AlCrN system by alloying with Si. Since Si has a low solubility limit in AlCrN and segregates along the grain boundaries, already small amounts result in the formation of a nanocomposite structure with AlCrN crystal-
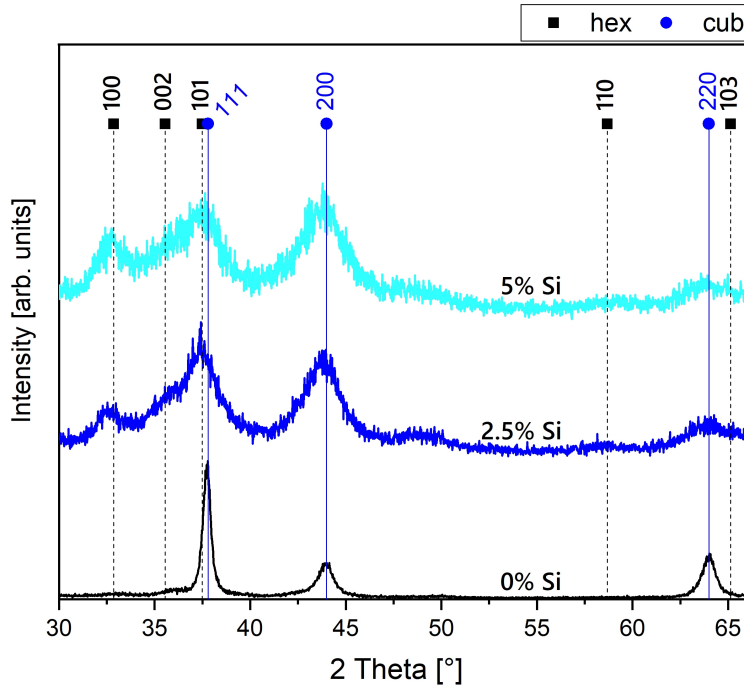
Figure 2.6: X-ray diffractograms of AlCr(Si)N coatings with 0 at.%, 2.5 at.% and 5 at.% Si, respectively. While the AlCrN coatings is purely cubic, the Si-containing coatings have a mixed (hexagonal + cubic) crystal structure [own work].

lites embedded in an amorphous Si_3N_4 tissue phase. Fig. 2.5 demonstrates the structural evolution of the AlCr(Si)N system as a function of the Si-content. While a typical columnar morphology forms for AlCrN, the addition of 2.5 at.% and 5 at.%, respectively, results in the formation of a nanocomposite microstructure, evidenced by the glassy and featureless fracture cross-section. The formation of the nanocomposite structure is accompanied by a significant reduction in grain size as evidenced by X-ray diffraction (Fig. 2.6). The X-ray diffractograms of the Si-containing coatings exhibit peaks with much larger FWHM compared to AlCrN.

Within the last chapter, the AlCrN coating system including multi-layered and nanocomposite coatings will be briefly introduced. The next chapter focuses on the thermal stability of nanostructured nitride coatings and on methods characterizing the high-temperature behavior of these coatings. Special attention will be drawn on the challenges of analyzing heterogeneous coating systems with complex architectures.

Thermal stability of nanostructured nitride coatings

Nanostructured nitride coatings synthesized by PVD techniques exhibit a wide variety of elemental compositions and microstructures including phase composition, grain size, defect density, residual stress development, texture and surface morphology [43, 44]. Additionally, structural inhomogeneities and gradients over the coating thickness are typically implemented during the deposition process [15, 17, 37]. For coatings synthesized by PVD techniques at temperatures far below their melting points, the thermodynamic equilibrium can not be achieved during deposition [4]. Cooling rates in the range of $10^{15}\,\mathrm{K\,s^{-1}}$ during coating growth result in kinetic limitations which allow for synthesis of metastable phases [37]. While nanostructured nitride coatings benefit from their metastable nature resulting in unique properties not accessible in their bulk material counterparts, this metastability often limits their application at elevated temperatures [45]. Temperatures of coated tools in modern applications may exceed 1000 °C during operation [46] and coatings can consequentially be subjected to recovery, recrystallization and grain growth, phase separation, interdiffusion, phase transformation and oxidation [45, 47]. Since the properties of nanostructured nitride coatings are strongly related to their microstructure, a comprehensive understanding of microstructural changes occurring at elevated temperatures is of vital importance.

To study the thermal stability of nitride coatings and its underlying mechanisms, many methods ranging from simple annealing treatments of coated samples to advanced in-situ high-temperature XRD experiments have been developed [45, 47]. The methods used to study the thermal stability within this work are shortly described in the following sections, and their advantages and limits briefly discussed. It has to be mentioned though, that the focus lies more on the comparison of the methods, rather than on a detailed introduction to the basics of thermal analysis or the underlying theory.

3.1 Differential scanning calorimetry and thermogravimetric analysis

Differential scanning calorimetry is a well-established method to study exothermic and endothermic reactions during annealing of coatings by measuring the energy released or consumed by the sample as a function of temperature [48]. DSC measurements are often combined with thermogravimetric analysis to get additional information about changes in sample mass at elevated temperatures [32, 45]. To achieve sufficient DSC and TGA signals and to avoid any superposition of signals stemming from substrate and coating, the substrate material has to be removed prior to the measurements. For this purpose, the coating is deposited on a dissoluble substrate, e.g. on a thin low-alloyed steel foil (Fig. 3.1(a)). Afterwards, the steel foil is chemically removed by 10% nitric acid and free-standing flakes of the coating are obtained (Fig. 3.1(b)). Dissolution is done at $\sim80\,°C$ and constant stirring to accelerate the process. With non-magnetic coating materials, the complete dissolution of the iron foil can be easily checked during the process using a magnet as only incompletely dissolved particles of the steel foil are attracted by the magnet. Alternatively, NaCl substrates [49] or a thermoplastic resin interlayer [50] may be used, subsequently dissolved by water or trichloromethane, respectively. The use of a steel foil as a metallic substrate comes closest to the substrates for nitride hard coatings used in industry (high-speed steel, cemented carbide). The resulting coating flakes are washed using distilled water and acetone and then dried. In order to get a particle size as uniform as possible, the coating flakes are milled in an agate mortar to a fine powder (Fig. 3.1(c)).
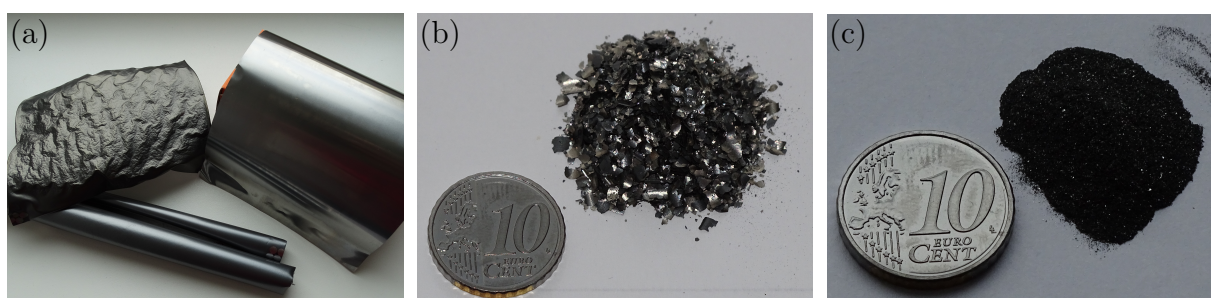
Figure 3.1: Procedure to obtain a powdered coating without substrate material. In (a) coated low-alloyed steel foils rolled-up or deformed due to the compressive residual stress of the coatings, (b) flakes of the coatings after removal of the substrate material with nitric acid and (c) the fine powder after grinding in an agate mortar to obtain uniformly sized particles are shown [own work].

To get sufficient signals from DSC and TGA measurements, a minimum amount of coating material is required (e.g. $20\,mg$ - $30\,mg$). To measure the thermal stability of the materials against microstructural changes, inert atmospheres such as argon or nitrogen have to be used, for oxidation studies synthetic air or pure oxygen is required. It has to be mentioned

that different atmospheres have an impact on the measurement as some reactions depend on the partial pressure of the gases used [51]. For measurements in an inert atmosphere, each measurement is immediately followed by a second run, serving as a baseline for the first one. For measurements in oxidative atmospheres, better results have been obtained within this thesis using a second, independent measurement with empty crucibles to subtract the background.

Since many structural changes may occur almost simultaneously in relatively small temperature ranges in nanostructured nitride coatings, it is difficult to unravel the individual reactions from the superimposed DSC/TGA signals. To overcome this issue, complementary ex-situ XRD measurements of samples annealed at various temperatures are often performed additionally. In Fig. 3.2, an exemplary set of data is presented, showing the heat flow, the mass change and the ex-situ X-ray diffractograms of an $Al_{90}Cr_{10}N$ coating obtained by DSC, TGA and XRD, respectively. The coating forms a solid solution with a hexagonal crystal structure thermally stable up to 1000 °C, which starts to decompose into AlN and Cr_2N (accompanied by the release of nitrogen) above this temperature. Such a conclusion is difficult to make based solely on the DSC data, since many reactions like defect recovery, grain growth, etc. contribute to the signal and no distinct (exothermic) peak can be assigned to the decomposition (Fig. 3.2(a)). In combination with the mass signal from TGA, where a slight decrease resulting from the release of nitrogen can be observed above 1000 °C, and the supplementary information from XRD, where an additional reflection corresponding to Cr_2N develops for the powder annealed at 1080 °C (Fig. 3.2(b)), a more comprehensive understanding of the ongoing processes can be obtained.
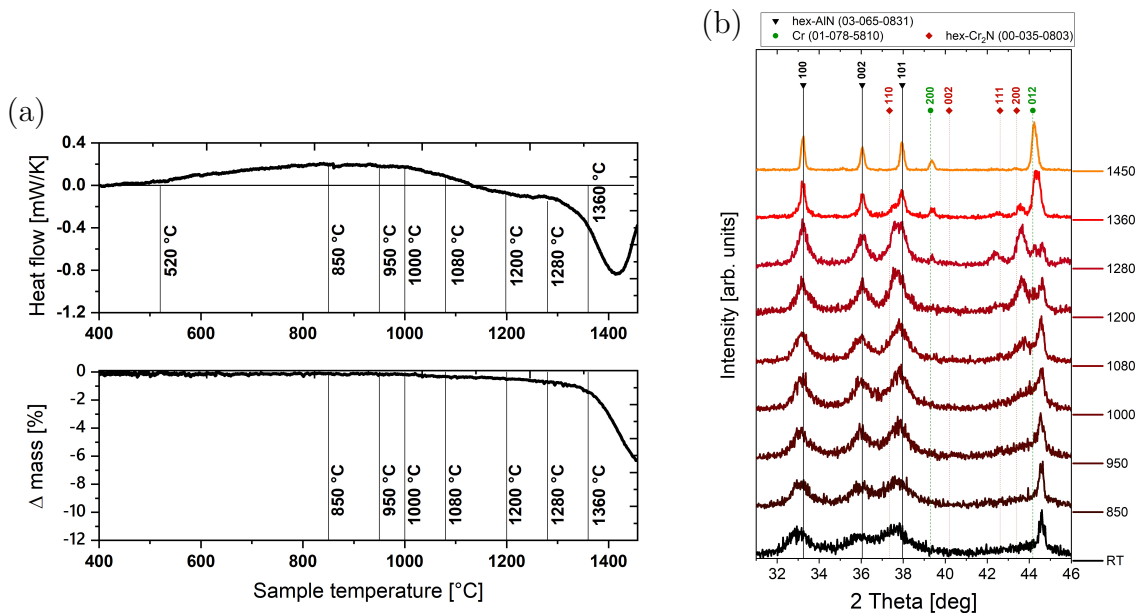
Figure 3.2: (a) Heat flow and relative mass change as a function of temperature of a powdered AlCrN coating and (b) the corresponding ex-situ X-ray diffractograms [own work].

3.2   In-situ high-temperature high-energy grazing incidence transmission synchrotron X-ray diffraction

Within the last section, DSC and TGA were briefly described as a method to determine the thermal stability of coating materials. While DSC and TGA provide information about the reactions taking place and the corresponding mass change of the materials at elevated temperatures, respectively, in-situ high-temperature X-ray diffraction represents an alternative approach focusing on microstructural changes as a function of temperature. In this work, the recently developed in-situ HE-HT-GIT-XRD method was used to characterize the thermal stability of AlCrSiN coatings [26, 52]. The main advantages using synchrotron X-ray radiation arise from the high brilliance and the high energy of the X-ray beam, which facilitates the use of small beam sizes, short measurement times and the measurement of relatively thick samples in transmission geometry. The use of an X-ray beam with a diameter of only 30 nm to study stress, texture and defect density across a multi-layered coating [17], the microstructural characterization of a TiN coating on a cutting edge recording a total number of 270,541 2D-diffractogramms in an area of 27.5 x 24.5 μm^2 [52] or the investigation of a 5 mm thick coated sample in transmission geometry using an X-ray beam with 87.1 keV [52] may illustrate the possibilities of using advanced characterization techniques at synchrotron facilities.
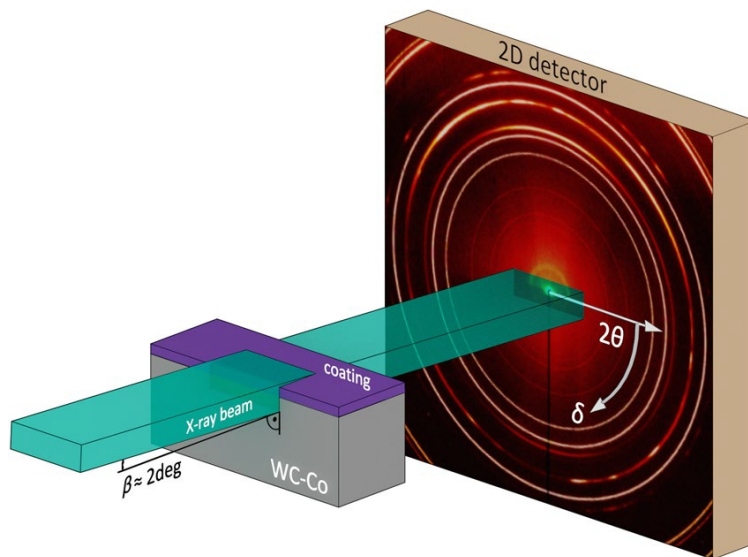
Figure 3.3: Experimental set-up at the P07B beamline of the PETRA III synchrotron source. A 5 mm thick coated sample is measured in transmission geometry using a pencil-shaped X-ray beam with a size of 400 x 100 μm^2 and an energy of 87.1 keV [52].

The above mentioned in-situ HE-HT-GIT-XRD method was also used to study the thermal stability of AlCr(Si)N coatings within this thesis, and will be now briefly described. The experiments were performed at the P07B beamline of the PETRA III synchrotron source

in Hamburg (D). The principle set-up for these experiments is shown in Fig. 3.3. The samples are mounted into a dilatometer (DIL 805 TA Instruments), which allows for heating the samples to temperatures up to 1200 °C and simultaneously measuring them in transmission geometry. To probe a large coating volume whilst maintaining minimal intensities of reflections stemming from the substrate, the sample surface can be slightly tilted (e.g. 2°) with respect to the primary beam. A pencil-shaped X-ray beam with a size of 400 x 100 µm² and an energy of 87.1 keV allows for examining large coating volumes and relatively thick samples. While the temperature is increased continuously, two-dimensional (2D) X-ray diffraction patterns are recorded using a Perkin-Elmer detector (Fig. 3.3a, b). Since the evaluation of the data is very sensitive to the experimental set-up (sample-to-detector distance, beam center on the detector, detector tilt, rotation angle of the tilt plane, etc.), an additional measurement using a standard material (e.g. LaB_6-powder) has to be done for a subsequent calibration.
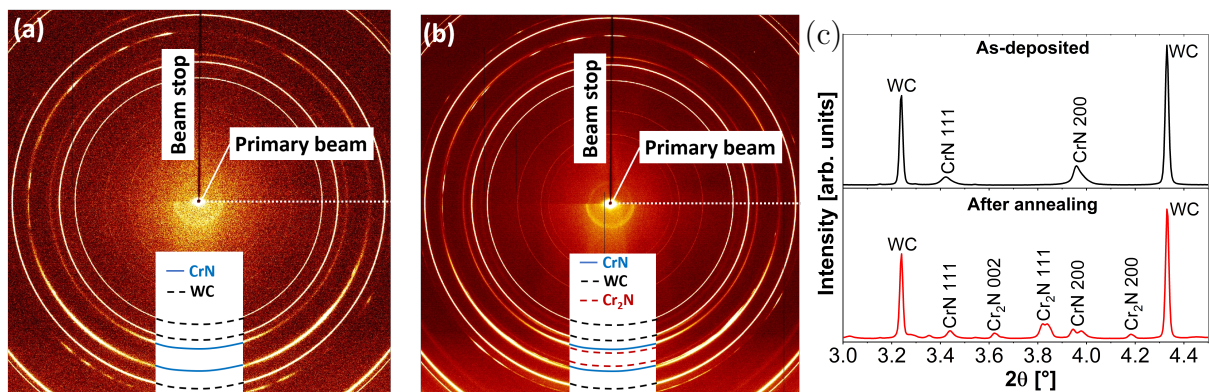
Figure 3.4: 2D X-ray diffraction patterns of an (a) as-deposited AlCrN coating and (b) after annealing and (c) the corresponding one-dimensional X-ray diffraction patterns at $\delta = 0°$ (marked by a dotted line in (a) and (b) [own work].

After measuring the samples at the beamline, an extensive data processing and evaluation is necessary, which can be done using the pyFAI software package [53]. In a first step, the 2D diffraction signals are integrated along the azimuthal angle δ resulting in phase plots representing the crystallographic evolution as a function of temperature (see Fig. 4 in Publication 2 [45]). Fig. 3.3 shows the recorded set of Debye-Scherrer rings of the as-deposited state at the very beginning of the experiments Fig. 3.4(a), after annealing Fig. 3.4(b) and the corresponding one-dimensional X-ray diffraction patterns at $\delta = 0°$, respectively. In the as-deposited state, reflections from the thermodynamically metastable cubic solid solution and from the tungsten carbide substrate can be seen (Fig. 3.4(a)a,c), after annealing additional reflections stemming from the Cr_2N phase formed during decomposition of CrN can be found (Fig. 3.4(a)b,c).

The strength of the in-situ HT-HE-GIT-XRD arises from the large amount of information,

3.2 In-situ high-temperature high-energy grazing incidence transmission synchrotron X-ray diffraction
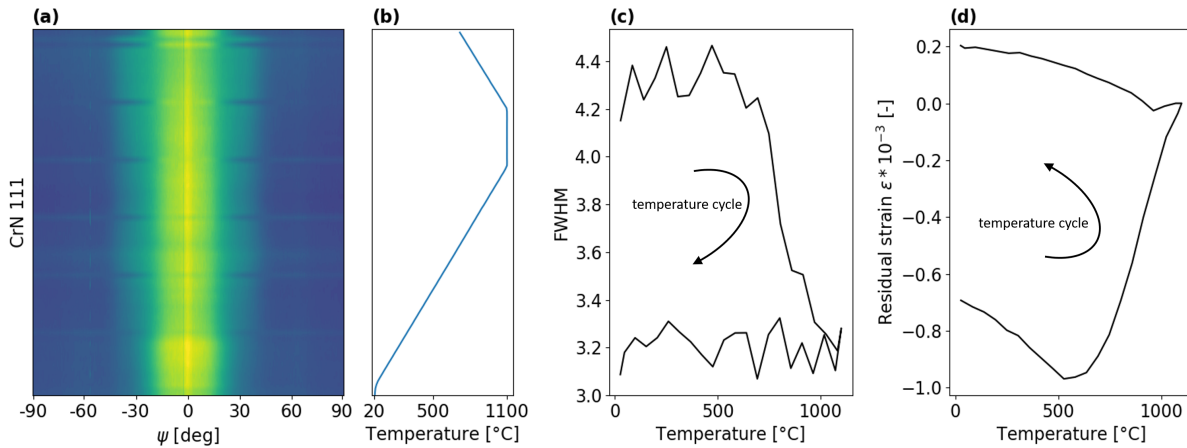
Figure 3.5: Examples for temperature-dependent properties of an AlCrN coating, which can be obtained simultaneously by the in-situ HT-HE-GIT-XRD method. Information about texture can be assessed by evaluating the (a) azimuthal intensity distribution of the c-CrN 111 peak, shown together with the (b) applied temperature. The (c) FWHM and the (d) residual strain as a function of temperature evaluated from the same CrN 111 peak indicates the grain size/defect density and the residual stress state of the coating, respectively [own work].

which can be obtained simultaneously by evaluating the 2D diffractograms. In addition to the phase evolution as a function of temperature, temperature-dependent information about texture, grain size, structural defects, residual stress state and coefficients of thermal expansion can be received, as exemplary shown in Fig. 3.5. By radial (θ) integration of the Debye-Scherrer rings, the azimuthal intensity distributions as a function of the ψ angle provide information of the texture development. An example of such a texture plot is given in Fig. 3.5(a), showing the azimuthal intensity distribution of the c-CrN 111 peak of an AlCrN coating as a function of temperature. The coating exhibits an 111 fibre texture, which does not change in the investigated temperature range. By evaluating the FWHM of the respective diffraction peaks (fitted using the Pseudo-Voigt function [52]), information about grain size and structural defects can be obtained Fig. 3.5(c), as the FWHM is generally sensitive to the presence of lattice defects, size of coherently diffracting domains and micro-strains of second and third order. The AlCrN coating in the as-deposited state has a high defect density and a relatively small grain size in the range of nanometers, which is typical for nitride coatings synthesized by PVD [54]. This yields in broad diffraction peaks with low intensity, hence large FWHM in Fig. 3.5(c). At temperatures above deposition temperature ($\sim 500\,°C$), lattice defects start to anneal out and the FWHM consequently decreases. No structural changes occur during cooling and the FWHM stays constant (Fig. 3.5(c)). The residual strain as a function of temperature can be obtained by evaluating the ellipticity of the Debye-Scherrer rings. The exemplary AlCrN coating exhibits an overall compressive residual strain of -0.7×10^{-3} in the as-deposited state (Fig. 3.5(d)), consisting of an intrinsic

(resulting from lattice defects) and a thermal (due to a mismatch between the TECs of coating and substrate) strain component. When the temperature increases to $500\,^{\circ}\mathrm{C}$, the (in this case tensile) thermal strain component decreases and the overall compressive residual strain increases. Above deposition temperature ($\sim500\,^{\circ}\mathrm{C}$), defect annihilation leads to a reduction of the compressive intrinsic strain component and the compressive residual strain deceases to zero. An overall tensile residual strain of -0.2×10^{-3} is attained after cooling down to RT, as the tensile thermal strain is built up again (Fig. 3.5(d)). With the knowledge of the X-ray elastic constants $(\frac{1}{2})S_2^{hkl}(z)$ and $S_1^{hkl}(z)$ of the material, it is possible to calculate the residual stress from the residual strain [52]. This is sometimes difficult in practical cases, as the X-ray elastic constants strongly depend on the elemental composition, which might be difficult to determine precisely, especially when it changes during an experiment (e.g. due to decomposition) or across the coating thickness (e.g. graded/multi-layered coatings).

The above given examples revealing the development of crystallographic phases, texture, structural defects and residual strain state of an AlCrN coating as a function of temperature demonstrate the potential of the in-situ HT-HE-GIT-XRD method to simultaneously assess various properties of coating and substrate material at the same time. However, one also has to consider the large experimental effort, starting with sample preparation, the experiment itself and finally, the data evaluation, that this method entails. Furthermore, an access to synchrotron facilities is expensive and not always available. In the following section, in-situ HT-HE-GIT-XRD is compared with DSC/TGA and the benefits and limitations of the respective methods will be discussed.

3.3 Comparison of DSC/TGA and in-situ HT-HE-GIT-XRD

In the previous sections, DSC/TGA and in-situ HT-HE-GIT-XRD have been shortly described as suitable methods to investigate the thermal stability of nanostructured nitride coatings. Both approaches have their strengths and limitations, which will be identified and discussed within this section. One major difference arises from the fact that a coated sample can be measured by in-situ HT-HE-GIT-XRD, while DSC/TGA requires a chemical removal of the substrate to obtain a sufficient signal from the coatings without an influence of the substrate material. The mass signal of an AlCrN coating during oxidation on an inert sapphire substrate and in its powdered state in Fig. 3.6 demonstrates the need for removing the substrate prior to DSC/TGA experiments. While a good signal is achieved for the powder, the mass change of the coated sample is hardly noticeable as the measured coating volume is simply too small.

Since the example above demonstrates that DSC/TGA experiments require a powdered coating, attention has to be paid to the process of preparing the powder and its resulting properties. First, the coating itself might be affected during removal of the substrate.
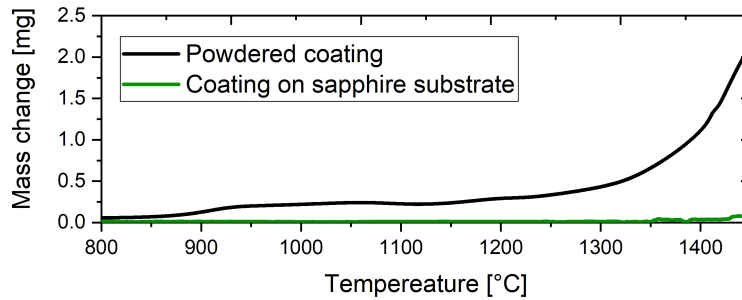
Figure 3.6: Mass signal of an AlCrN coating on a sapphire substrate and in its powdered state during annealing in synthetic air [own work].

Comparative XRD or EDX measurements of coating and powder before and after removing the substrate may indicate reactions of the coating material with the chemical solvent (e.g. nitric acid). Furthermore, the substrate may not be fully removed as strong chemical bonds and intermetallic phases between coating and substrate material may form at the coating-substrate interface (depending on the substrate material)[55, 56]. This effect is promoted by enhanced intermixing between coating and substrate as a result of extensive plasma pre-treatments prior to deposition applied to improve the coating adhesion [57]. In Fig. 3.7, iron-containing residuals stemming from the incompletely removed steel substrate can be clearly seen on several coating particles on the side originally facing the substrate (marked in red). The residuals are revealed by z-contrast (Fig. 3.7(a): iron with high atomic mass appears bright) and their different surface topography (Fig. 3.7(b): vermicular structure). The vermicular structure was formed during annealing at $1200\,^{\circ}\mathrm{C}$ and indicates intermetallic compounds consisting of Fe and Al with melting points below annealing temperature (e.g. $FeAl_2$, Fe_3Al_5, $FeAl_3$ [55]).
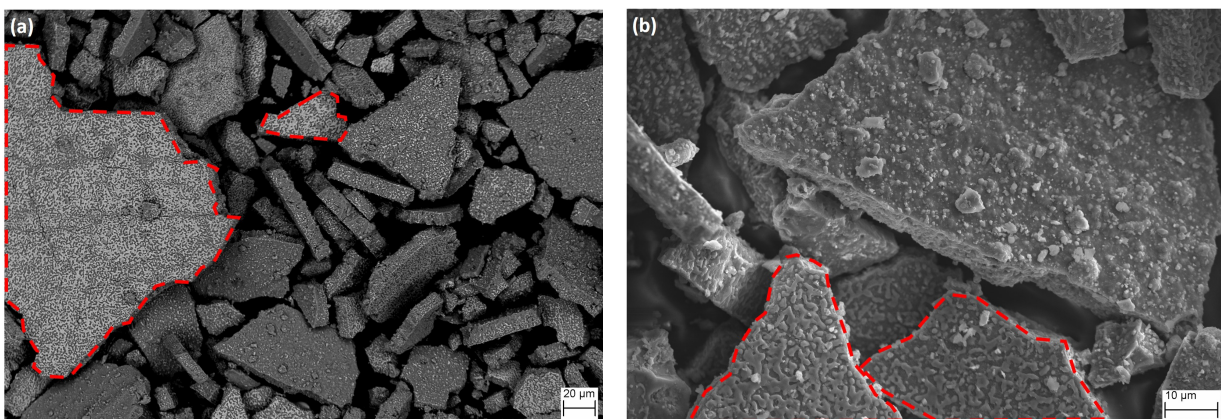
Figure 3.7: A powdered AlCrN coating after annealing in Ar atmosphere at $1200\,^{\circ}\mathrm{C}$ obtained by (a) back-scattered SEM and (b) secondary electron SEM. Particles with iron-containing residuals stemming from the incompletely removed steel substrate are marked in red [own work].
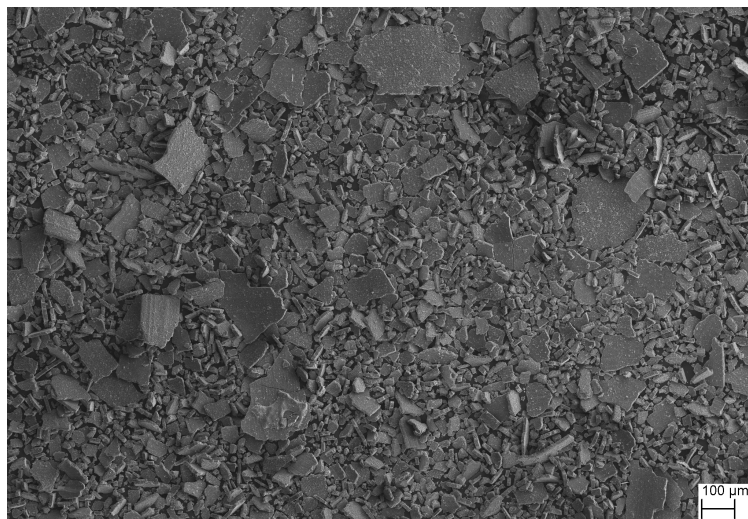
Figure 3.8: AlCrN coating prepared for DSC/TGA measurements by chemically removing the steel foil substrate and milling to a fine powder [own work].

In Fig. 3.8, a scanning electron microscopy (SEM) micrograph of an AlCrN powdered coating prepared for DSC/TGA is shown. Although the powder was milled in an agate mortar to obtain a fine, uniformly sized powder, particles with diameters ranging from 10 µm to >300 µm can be found. This large differences in particle size have an impact on the reaction kinetics during the measurement, especially in oxygen containing atmospheres, where the total surface area has a large impact on the oxidation kinetics [58]. In particular, multi-layered coatings with an optimized top layer against oxidation and monolithic coatings which tend to form a dense oxide scale acting as protecting layer against further oxidation have to be considered in this context. When the coating is applied on a substrate, only the coating surface is exposed to the oxidative atmosphere. In the case of a powdered coating, the total surface area is at least doubled and, even more important especially for multi-layered coatings, also the part of the coating originally facing the substrate is exposed to oxygen (which is most probably optimized for adhesion, but not for protection against oxidation). The formation of a protective oxide layer on the surface of two AlCr(Si)N coatings after annealing in synthetic air at 1260 °C can be clearly seen in Fig. 3.9. While the AlCrN coating oxidizes also below the porous oxide layer, evidenced by the rough surface morphology where the oxide layer is chipped off (Fig. 3.9(a)), a dense protective oxide layer is formed on AlCrSiN (Fig. 3.9(b)). The dense oxide layer acts as a diffusion barrier, suppresses the inward diffusion of oxygen and prevents the coating underneath from further oxidation, which can be recognized by the smooth appearance of the coating in areas with chipped oxide layer (Fig. 3.9(b)).

Another important factor to be considered is the relaxation of residual stress when the substrate is removed. The large impact of the residual stress state on the thermal stability of nitride coatings was shown by Meindlhumer et al. [26]. They observed that the decomposi-
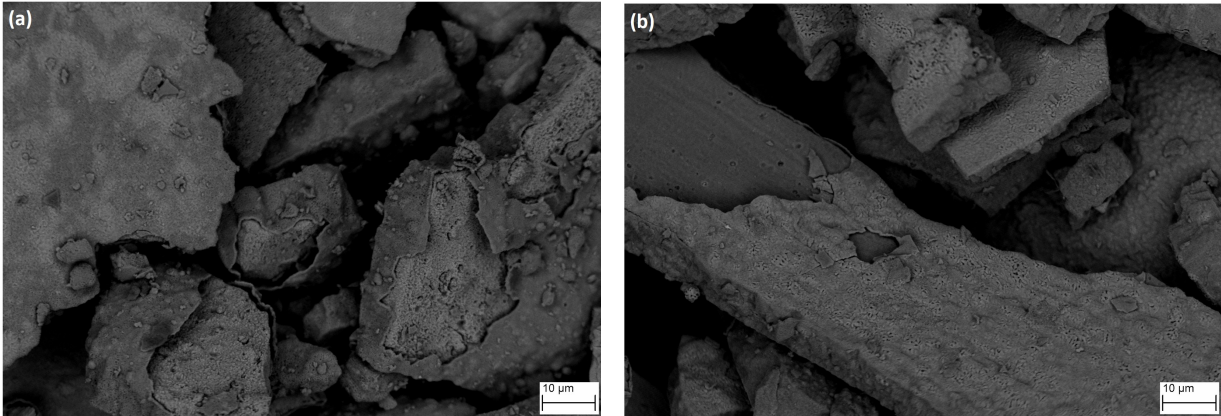
Figure 3.9: SEM micrographs of (a) AlCrN and (b) AlCrSiN powdered coatings after annealing in synthetic air at 1260 °C [own work].

tion onset temperature of AlCrN coatings is dependent on their compressive residual stress state. As the residual stress is almost entirely released by removal of the substrate, different onset temperatures of thermal stability related reactions are measured by DSC/TGA and in-situ HE-HT-GIT-XRD. This is discussed in more detail within the second publication of this thesis [45]. The relaxation of compressive residual stress of an AlCrN coating is demonstrated by a peak shift to lower 2θ angles in the X-ray diffractograms shown in Fig. 3.10.
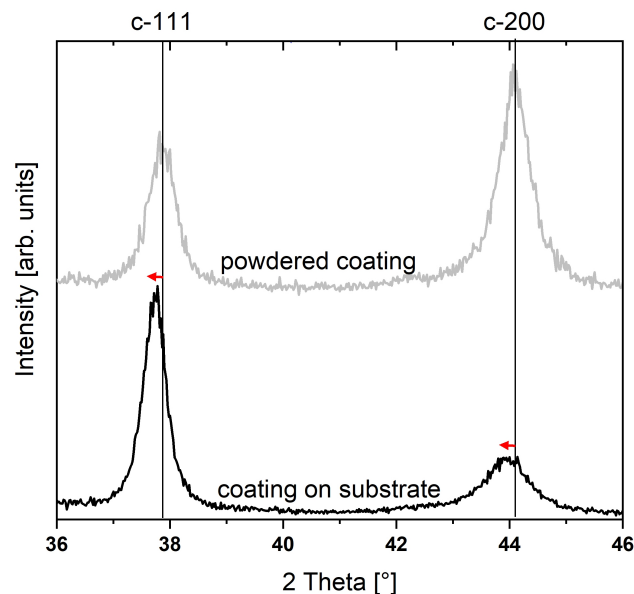
Figure 3.10: X-ray diffractograms of a cubic AlCrN coating on a substrate and in its powdered state. A shift of the 111 and 200 peak to lower 2θ angles due to compressive residual stress is marked by red arrows [own work].

Nanostructured nitride coatings often exhibit a pronounced texture resulting from the growth conditions during deposition [17, 59, 60]. While for the in-situ HE-HT-GIT-XRD method the

texture of the individual phases can be detected as a function of temperature, information about texture is completely lost when measuring a powder with randomly oriented particles. This is demonstrated by XRD measurements in Fig. 3.10. For the measurement of the AlCrN coating on the substrate, the 111 fibre texture is indicated by a much higher intensity of the 111 peak compared to the 200 peak. To get the full information about texture, additional investigations like pole figure measurements are required. In contrast, no information can be gained from the coating in its powdered state, as the particles of the powder are randomly distributed (note the change in intensity of the 111 and 200 peak in Fig. 3.10).
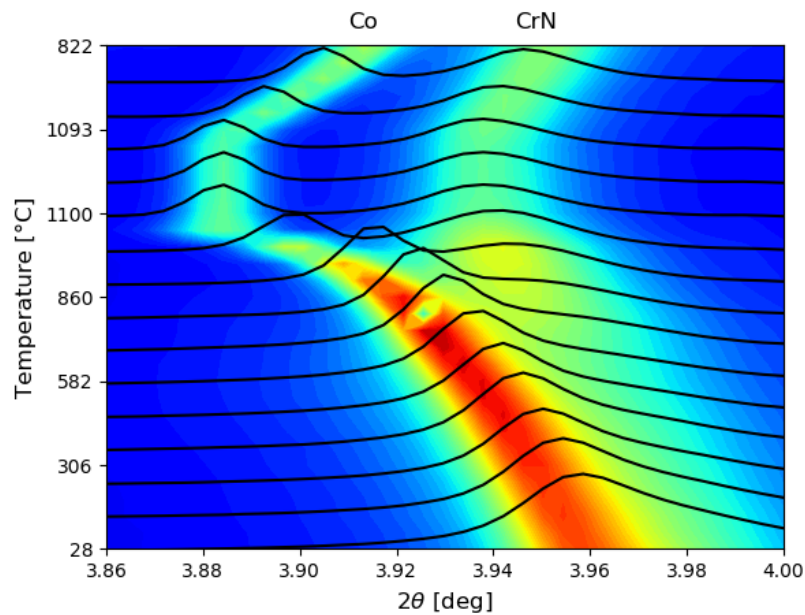
Figure 3.11: Diffraction intensities I(θ,T) as a function of temperature showing reflections stemming from the Co of the substrate and CrN of the coating. One-dimensional diffractograms at several temperatures are inserted to visualize the overlap of the Co and CrN reflections up to a temperature of ~900 °C [own work].

So far, mainly limitations arising from the use of powdered coatings when thermal stability is studied were discussed. It was shown that it is necessary to use powdered coatings to ensure sufficient signals from DSC/TGA. In the following, advantages of measuring a powdered coating and issues associated with the measurement of a coating on a substrate will be discussed. Firstly, the removal of the substrate avoids superimposed signals from coating and substrate material during the measurements, which makes interpretation of the results much easier. This issue has to be considered for the in-situ HE-HT-GIT-XRD method, where X-ray reflections stemming from coating and substrate may overlap if the phases have similar peak positions. An example of such an overlap is presented in Fig. 3.11, showing reflections of Co and CrN stemming from the substrate and the coating, respectively. Only a broad, asymmetric peak is visible at RT, which can be barely separated into its individual

constituents corresponding to Co and CrN. It makes further data evaluation (e.g. analysis of FWHM, strain, etc.) very difficult. As Co and CrN have largely different thermal expansion coefficients, a splitting into the individual peaks of the corresponding phase is observed with increasing temperature.
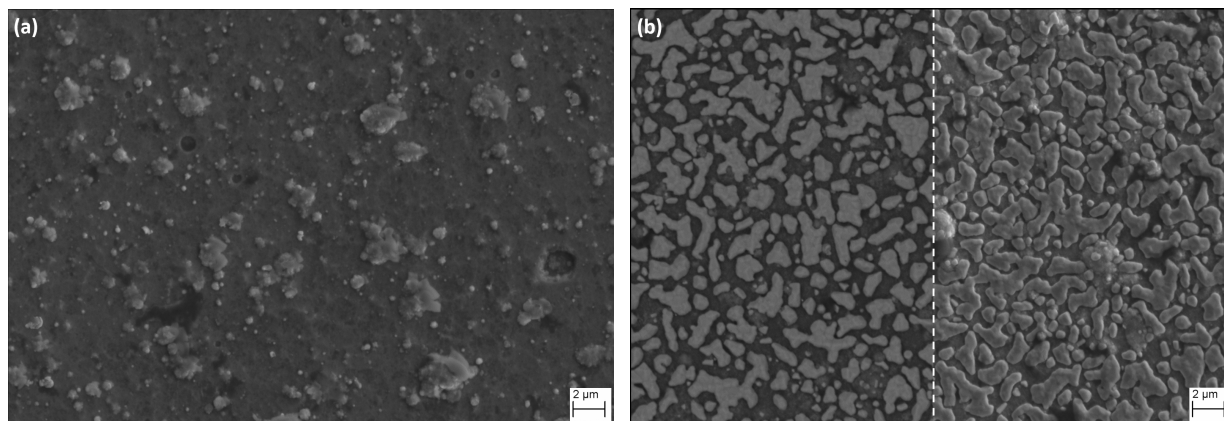
Figure 3.12: Surface of an AlCrN coating on a cemented carbide substrate in the (a) as-deposited state (secondary electron SEM) and (b) after vacuum annealing at 1000 °C for 30 min obtained by back scattered SEM (left) and secondary electron SEM (right) [own work].

Another topic to be considered, when the thermal stability of the whole coating-substrate system is studied, is the coating-substrate interface diffusion. If atoms from the substrate diffuse into the coating (and vice versa) at elevated temperatures, the properties of the coating material (including thermal stability) can significantly change. In Fig. 3.12, the surface of an AlCrN coating is shown in the as-deposited state and after vacuum annealing at 1000 °C for 30 min. After annealing, the surface is highly contaminated with Co stemming from the cobalt metal binder of the cemented carbide (WC-Co), which diffused through the whole coating during annealing (Fig. 3.12(b)). To overcome this issue, a diffusion barrier (e.g. TiN) between substrate and coating can be applied, or the measurement has to be done as fast as possible. While an additional diffusion barrier layer contributes to the X-ray diffractograms (making the evaluation more complicated), fast measurements with short measurement times at each temperature require highly sensitive X-ray detectors to obtain sufficient signal yields.

Within this section, DSC/TGA combined with ex-situ XRD and in-situ HT-HE-GIT-XRD were compared regarding their suitability to study the thermal stability of nanostructured nitride coatings. The most important characteristics including benefits and limitations of each method are summarized in Table 3.1. Each of these methods has its strengths and limitations and no general statement which method is preferable can be given. The newly developed in-situ HT-HE-GIT-XRD method provides information about various materials properties simultaneously, but requires access to a synchrotron facility. The ideal case is

Table 3.1: The most important characteristics of DSC/TGA combined with ex-situ XRD and in-situ HT-HE-GIT-XRD based on the author's experience obtained during the work for this thesis. The benefits and disadvantages of the respective method are highlighted in green and red, respectively.

DSC/TGA combined with ex-situ XRD	in-situ HT-HE-GIT-XRD
information about reaction enthalpies (DSC), sample mass change (TGA) and formed phases (ex-situ XRD)	simultaneous information about crystallographic phases, defect density, texture, residual stress, etc.
powdered coating	coating-substrate system
impact of sample preparation	unaffected coating-substrate system
no information about texture, stress relaxation	preserved texture and residual stress state
temperatures up to 2400 °C (in inert atmosphere)	limited temperature range (max. 1200 °C)
oxidative atmospheres (synthetic air/oxygen)	only inert atmosphere or vacuum
for amorphous phases also	only for crystalline samples
easy access, cheap	requires synchrotron facility, expensive
extensive sample preparation (chemically removal of substrate)	extensive data acquisition (limited software available)

of course the combination of both methods, which provides extensive information about numerous independent material properties and their variation as a function of temperature, and allows for a comprehensive understanding on the thermal stability of the whole coating-substrate system.

CHAPTER **4**

Summary and conclusions

Wear-resistant coatings on cutting tools, molds and in forming applications find widespread use in industry to protect surfaces from wear and corrosion. However, the increasing demand on the coatings in high-temperature applications like high-speed cutting or dry-cutting stimulate the development of materials with enhanced mechanical properties and thermal stability. In order to face the severe requirements in modern applications, next generation materials rely on advanced microstructural and compositional designs. The aim of the present thesis is the development of new coating materials with improved mechanical properties, high thermal stability and good resistance against high-temperature oxidation based on various novel approaches.

The first approach is based on the combination of materials differing in their mechanical properties in a multi-layered architecture with specific stress design. This approach allows for synthesis of coatings with high hardness and simultaneously high toughness, which are otherwise exclusive properties. The improved fracture toughness is associated with an increased energy dissipation as cracks are multiple deflected on interfaces implemented by structural and compositional heterogeneities. An example of this approach represents a multi-layered AlCrN coating consisting of hard, cubic and soft, hexagonal layers. In order to understand the influence of the complex architecture on the microstructure and the resulting coating properties, the newly developed cross-sectional X-ray nanodiffraction method was used to study phases, texture, crystallite size and residual strains position-resolved across the coating thickness. In addition to an as-deposited sample, a sample annealed at 1000 °C in vacuum was investigated to address the impact of the multi-layered architecture on the thermal stability of the system. By arranging the individual constituents in a dedicated architecture, it was possible to interrupt the columnar grain growth at interfaces between the layers with different phases, to control the development of the residual stress profile across the coating thickness and to govern the decomposition of the metastable cubic AlCrN phase.

The second approach is based on the microstructural design of coatings with nanocomposite

structure. The impact of the Si-content on the microstructure of AlCr(Si)N coatings and the associated coating properties was studied. While the second part of the thesis focused on the thermal stability of the coatings, their oxidation behavior was studied in more detail in the third part. Adding Si to the AlCrN system results into a nanocomposite microstructure with AlCrN crystallites embedded in an amorphous Si_xN_y tissue phase, as the solubiltiy limit of Si in AlCrN is very low and it tends to segregate along the grain boundaries. While in typical physical vapor deposited coatings with columnar microstructure a continuous diffusion path along grain boundaries exists, inter-granular diffusion is suppressed in AlCrSiN by the amorphous Si_xN_y phase encapsulating the individual AlCrN grains. In a first step, the thermal stability excluding oxidation of three AlCr(Si)N coatings with 0 at.%, 2.5 at.% and 5 at.% Si was investigated by differential scanning calorimetry, thermogravimetric analysis and ex-situ X-ray diffraction. Furthermore, the coatings were studied by the recently developed in-situ high-temperature high-energy grazing-incidence transmission X-ray diffraction. This method allowed to simultaneously access temperature-dependent variations of phases, defect densities, grain sizes, residual stress states and thermal expansion coefficients of coating and substrate material. The results revealed an increasing thermal stability with increasing Si-content of the AlCr(Si)N coatings and simultaneously improved mechanical properties at elevated temperatures.

In a second step, all three AlCr(Si)N coatings were investigated in terms of their oxidation behavior. The coatings were analyzed by differential scanning calorimetry, thermogravimetric analysis and ex-situ X-ray diffraction in ambient air. Additionally, a partially oxidized sample of the best performing AlCrSiN coating with 5 at.% Si was studied along the coating thickness by cross-sectional X-ray nanodiffraction and scanning transmission electron microscopy to gain deeper knowledge about elemental and microstructural changes during high-temperature oxidation. The results revealed the outwards diffusion of coating elements like Al, Cr and Si to the surface, where they oxidize, and the inward diffusion of oxygen as main mechanisms decisive for high-temperature oxidation. The results showed that the nanocomposite structure of the Si-containing coatings has a beneficial effect on the oxidation resistance of the AlCr(Si)N system resulting in an increase of the onset temperature of oxidation from 1100 °C to 1260 °C with Si-content from 0 at.% to 5 at.%. The study furthermore revealed that the oxidation behavior of the Si-containing coatings is positively affected by the formation of Cr_3Si instead of Cr after the decomposition of the AlCrN phase into AlN, Cr and N_2, since Cr outwards diffusion is suppressed as it is chemical bond.

This thesis presents several successful attempts to synthesize hard, wear-resistant coatings with excellent mechanical properties and simultaneously outstanding thermal stability and resistance against high-temperature oxidation. Furthermore, it underlines the importance of advanced, position resolved characterization techniques for the analysis of coatings with complex architecture and stress design in order to understand the relations between process,

coating microstructure and properties. The thesis also allows pointing out areas of possible future work. While within the present thesis AlCrSiN coatings with Si-contents up to $5\,\mathrm{at.\%}$ were investigated, it would be interesting to study the effect of even higher amounts of Si in the coatings.

Bibliography

[1] W.-D. Münz. "Titanium aluminum nitride films: A new alternative to TiN coatings". In: *Journal of Vacuum Science & Technology A: Vacuum, Surfaces, and Films* 4.6 (1986), pp. 2717–2725.

[2] J. Patscheider, T. Zehnder, and M. Diserens. "Structure–performance relations in nanocomposite coatings". In: *Surface and Coatings Technology* 146-147 (2001), pp. 201–208.

[3] J. P. R. Hauert. "From Alloying to Nanocomposites-Improved Performance of Hard Coatings". In: *Advanced Engeneering Materials* (2000), pp. 248–259.

[4] A. Anders. *Cathodic Arcs: From Fractal Spots to Energetic Condensation.* New York: Springer, 2008. ISBN: 978-0-387-79107-4.

[5] M. Kawate, A. Kimura, and T. Suzuki. "Microhardness and lattice parameter of $Cr_{1-x}Al_xN$ films". In: *Journal of Vacuum Science & Technology A: Vacuum, Surfaces, and Films* 20.2 (2002), pp. 569–571.

[6] S. PalDey and S. Deevi. "Single layer and multilayer wear resistant coatings of (Ti, Al) N: a review". In: *Materials Science and Engineering: A* 342.1-2 (2003), pp. 58–79.

[7] M. Kawate, A. K. Hashimoto, and T. Suzuki. "Oxidation resistance of $Cr_{1-x}Al_xN$ and $Ti_{1-x}Al_xN$ films". In: *Surface and Coatings Technology* 165.2 (2003), pp. 163–167.

[8] H. Willmann, P. H. Mayrhofer, P. Persson, A. E. Reiter, L. Hultman, and C. Mitterer. "Thermal stability of Al–Cr–N hard coatings". In: *Scripta Materialia* 54.11 (2006), pp. 1847–1851.

[9] H. Willmann, P. H. Mayrhofer, L. Hultman, and C. Mitterer. "Hardness evolution of Al–Cr–N coatings under thermal load". In: *Journal of Materials Research* 23.11 (2008), pp. 2880–2885.

[10] P. Fratzl and R. Weinkamer. "Nature's hierarchical materials". In: *Progress in Materials Science* 52.8 (2007), pp. 1263–1334.

[11] O. Paris, I. Burgert, and P. Fratzl. "Biomimetics and biotemplating of natural materials". In: *Mrs Bulletin* 35.3 (2010), pp. 219–225.

[12]   R. Lakes. "Materials with structural hierarchy". In: *Nature* 361.6412 (1993), pp. 511–515.

[13]   S. Weiner and W. Traub. "Bone structure: from angstroms to microns." In: *The FASEB journal* 6.3 (1992), pp. 879–885.

[14]   A. Jackson, J. F. Vincent, and R. Turner. "The mechanical design of nacre". In: *Proceedings of the Royal society of London. Series B. Biological sciences* 234.1277 (1988), pp. 415–440.

[15]   R. Daniel, M. Meindlhumer, J. Zalesak, B. Sartory, A. Zeilinger, C. Mitterer, and J. Keckes. "Fracture toughness enhancement of brittle nanostructured materials by spatial heterogeneity: A micromechanical proof for CrN/Cr and TiN/SiO$_x$ multilayers". In: *Materials & Design* 104 (2016), pp. 227–234.

[16]   J. Keckes, M. Bartosik, R. Daniel, C. Mitterer, G. Maier, W. Ecker, J. Vila-Comamala, C. David, S. Schoeder, and M. Burghammer. "X-ray nanodiffraction reveals strain and microstructure evolution in nanocrystalline thin films". In: *Scripta Materialia* 67.9 (2012), pp. 748–751.

[17]   J. Keckes, R. Daniel, J. Todt, J. Zalesak, B. Sartory, S. Braun, J. Gluch, M. Rosenthal, M. Burghammer, C. Mitterer, S. Niese, and A. Kubec. "30 nm X-ray focusing correlates oscillatory stress, texture and structural defect gradients across multilayered TiN-SiO$_x$ thin film". In: *Acta Materialia* 144 (2018), pp. 862–873.

[18]   F. Klocke, A. Krämer, H. Sangermann, and D. Lung. "Thermo-mechanical tool load during high performance cutting of hard-to-cut materials". In: *Procedia CIRP* 1 (2012), pp. 295–300.

[19]   E. Pflüger, A. Schröer, P. Voumard, L. Donohue, and W.-D. Münz. "Influence of incorporation of Cr and Y on the wear performance of TiAlN coatings at elevated temperatures". In: *Surface and Coatings Technology* 115.1 (1999), pp. 17–23.

[20]   J. L. Endrino and V. Derflinger. "The influence of alloying elements on the phase stability and mechanical properties of AlCrN coatings". In: *Surface and Coatings Technology* 200.1-4 (2005), pp. 988–992.

[21]   S. Vepřek. "The search for novel, superhard materials". In: *Journal of Vacuum Science & Technology A: Vacuum, Surfaces, and Films* 17.5 (1999), pp. 2401–2420.

[22]   S. Veprek and M. Jilek. "Super- and ultrahard nanacomposite coatings: generic concept for their preparation,properties and industrial applications". In: *Vacuum* 67 (2002), pp. 443–449.

[23]   J. Musil and P. Zeman. "Hard a-Si$_3$N$_4$/MeN$_x$ Nanocomposite Coatings with High Thermal Stability and High Oxidation Resistance". In: *Solid State Phenomena* 127 (2007), pp. 31–36.

[24] S. Q. Wang, L. Chen, B. Yang, K. K. Chang, Y. Du, J. Li, and T. Gang. "Effect of Si addition on microstructure and mechanical properties of Ti–Al–N coating". In: *International Journal of Refractory Metals and Hard Materials* 28.5 (2010), pp. 593–596.

[25] M. Meindlhumer, J. Zalesak, R. Pitonak, J. Todt, B. Sartory, M. Burghammer, A. Stark, N. Schell, R. Daniel, J. F. Keckes, et al. "Biomimetic hard and tough nanoceramic Ti–Al–N film with self-assembled six-level hierarchy". In: *Nanoscale* (2019).

[26] M. Meindlhumer, S. Klima, N. Jäger, A. Stark, H. Hruby, C. Mitterer, J. Keckes, and R. Daniel. "Stress-controlled decomposition routes in cubic AlCrN films assessed by in-situ high-temperature high-energy grazing incidence transmission X-ray diffraction". In: *Scientific Reports* 9.1 (Dec. 2019), p. 18027.

[27] O. Knotek, F. Lo, H.-J. Scholl, et al. "Properties of arc-evaporated CrN and (Cr, Al) N coatings". In: *Surface and Coatings Technology* 45.1-3 (1991), pp. 53–58.

[28] J. Vetter, E. Lugscheider, and S. Guerreiro. "(Cr: Al) N coatings deposited by the cathodic vacuum are evaporation". In: *Surface and Coatings Technology* 98.1-3 (1998), pp. 1233–1239.

[29] W. Kalss, A. Reiter, V. Derflinger, C. Gey, and J. Endrino. "Modern coatings in high performance cutting applications". In: *International Journal of Refractory Metals and Hard Materials* 24.5 (2006), pp. 399–404.

[30] L. Zhou, D. Holec, and P. H. Mayrhofer. "First-principles study of elastic properties of cubic $Cr_{1-x}Al_xN$ alloys". In: *Journal of applied physics* 113.4 (2013), p. 043511.

[31] R. Daniel, K. J. Martinschitz, J. Keckes, and C. Mitterer. "Texture development in polycrystalline CrN coatings: The role of growth conditions and a Cr interlayer". In: *Journal of Physics D: Applied Physics* 42.7 (2009), p. 075401.

[32] P. H. Mayrhofer, F. Rovere, M. Moser, C. Strondl, and R. Tietema. "Thermally induced transitions of CrN thin films". In: *Scripta Materialia* 57.3 (2007), pp. 249–252.

[33] P. Mayrhofer, D. Music, and J. Schneider. "Ab initio calculated binodal and spinodal of cubic $Ti_{1-x}Al_xN$". In: *Applied Physics Letters* 88.7 (2006), p. 071922.

[34] S. Zhang, D. Sun, Y. Fu, and H. Du. "Toughening of hard nanostructural thin films: a critical review". In: *Surface and Coatings Technology* 198.1-3 (2005), pp. 2–8.

[35] P. Fratzl, H. S. Gupta, F. D. Fischer, and O. Kolednik. "Hindered crack propagation in materials with periodically varying Young's modulus—lessons from biological materials". In: *Advanced Materials* 19.18 (2007), pp. 2657–2661.

[36] O. Kolednik, J. Predan, F. D. Fischer, and P. Fratzl. "Bioinspired design criteria for damage-resistant materials with periodically varying microstructure". In: *Advanced Functional Materials* 21.19 (2011), pp. 3634–3641.

[37] N. Jäger, S. Klima, H. Hruby, J. Julin, M. Burghammer, J. Keckes, C. Mitterer, and R. Daniel. "Evolution of structure and residual stress of a fcc/hex-AlCrN multi-layered system upon thermal loading revealed by cross-sectional X-ray nano-diffraction". In: *Acta Materialia* 162 (2019), pp. 55–66.

[38] S. Vepřek and S. Reiprich. "A concept for the design of novel superhard coatings". In: *Thin solid films* 268.1-2 (1995), pp. 64–71.

[39] C. Mitterer, M. Rauter, and P. Rödhammer. "Sputter deposition of ultrahard coatings within the system Ti-BCN". In: *Surface and Coatings technology* 41.3 (1990), pp. 351–363.

[40] J. Schiøtz, F. D. Di Tolla, and K. W. Jacobsen. "Softening of nanocrystalline metals at very small grain sizes". In: *Nature* 391.6667 (1998), pp. 561–563.

[41] J. Patscheider. "Nanocomposite hard coatings for wear protection". In: *MRS bulletin* 28.3 (2003), pp. 180–183.

[42] J. Musil. "Hard nanocomposite coatings: Thermal stability, oxidation resistance and toughness". In: *Surface and Coatings Technology* 207 (2012), pp. 50–65.

[43] C. Mitterer, P. Mayrhofer, M. Beschliesser, P. Losbichler, P. Warbichler, F. Hofer, P. Gibson, W. Gissler, H. Hruby, J. Musil, et al. "Microstructure and properties of nanocomposite Ti–B–N and Ti–B–C coatings". In: *Surface and Coatings Technology* 120 (1999), pp. 405–411.

[44] H. Willmann, P. H. Mayrhofer, L. Hultman, and C. Mitterer. "Thermal stability and age hardening of supersaturated AlCrN hard coatings". In: *International Heat Treatment and Surface Engineering* 1.2 (2013), pp. 75–79.

[45] N. Jäger, M. Meindlhumer, S. Spor, H. Hruby, J. Julin, A. Stark, F. Nahif, J. Keckes, C. Mitterer, and R. Daniel. "Microstructural evolution and thermal stability of AlCr(Si)N hard coatings revealed by in-situ high-temperature high-energy grazing incidence transmission X-ray diffraction". In: *Acta Materialia* 186 (2020), pp. 545–554.

[46] V. Gutakovskis, G. Bunga, E. Niemi, and S. Laakso. "Finite element method modeling of the stainless steel cutting process using different machining parameters". In: *Transport and Engineering* 31.1 (2009), pp. 51–55.

[47] M. Meindlhumer, S. Klima, N. Jäger, A. Stark, H. Hruby, C. Mitterer, J. Keckes, and R. Daniel. "Stress-controlled decomposition routes in cubic AlCrN films assessed by in-situ high-temperature high-energy grazing incidence transmission X-ray diffraction". In: *Scientific reports* 9.1 (2019), pp. 1–14.

[48] P. K. Gallagher, M. E. Brown, and R. B. Kemp. *Handbook of thermal analysis and calorimetry*. Elsevier New York, 1998.

[49]   A. Abdulkadhim, M. to Baben, T. Takahashi, V. Schnabel, M. Hans, C. Polzer, P. Pol-
       cik, and J. M. Schneider. "Crystallization kinetics of amorphous Cr_2AlC thin films". In:
       Surface and Coatings Technology 206.4 (2011). Carbon-Based Nanostructured Coat-
       ings and Composite Films, pp. 599–603.

[50]   D. Zhong, J. Moore, B. Mishra, T. Ohno, E. Levashov, and J. Disam. "Composition
       and oxidation resistance of Ti–B–C and Ti–B–C–N coatings deposited by magnetron
       sputtering". In: *Surface and Coatings Technology* 163 (2003), pp. 50–56.

[51]   P. H. Mayrhofer, H. Willmann, L. Hultman, and C. Mitterer. "Influence of different
       atmospheres on the thermal decomposition of Al-Cr-N coatings". In: *Journal of Physics
       D: Applied Physics* 41.15 (2008), p. 155316.

[52]   M. Meindlhumer, N. äger, S. Spor, M. Rosenthal, J. Keckes, H. Hruby, C. Mitterer, R.
       Daniel, J. Keckes, and J. Todt. "Nanoscale residual stress and microstructure gradients
       across the cutting edge area of a TiN coating on WCCo". In: *Scripta Materialia* 182
       (2020), pp. 11–15.

[53]   J. Kieffer and D. Karkoulis. "PyFAI, a versatile library for azimuthal regrouping". In:
       Journal of Physics: Conference Series 425.20 (2013), p. 202012.

[54]   C. Mitterer. "PVD and CVD Hard Coatings". In: *Comprehensive Hard Materials*.
       Elsevier, 2014, pp. 449–467. ISBN: 9780080965284.

[55]   A. Griger and V. Stefaniay. "Equilibrium and non-equilibrium intermetallic phases in
       Al-Fe and Al-Fe-Si alloys". In: *Journal of materials science* 31.24 (1996), pp. 6645–
       6652.

[56]   H. Okamoto, T. Massalski, et al. "Binary alloy phase diagrams". In: *ASM Interna-
       tional, Materials Park, OH, USA* (1990).

[57]   C. Schönjahn, M. Bamford, L. Donohue, D. Lewis, S. Forder, and W.-D. Münz. "The
       interface between TiAlN hard coatings and steel substrates generated by high energetic
       Cr^x bombardment". In: *Surface and Coatings Technology* 125.1-3 (2000), pp. 66–70.

[58]   Y. Li and T. Qiu. "Oxidation behaviour of boron carbide powder". In: *Materials Sci-
       ence and Engineering: A* 444.1 (2007), pp. 184–191.

[59]   D. R. McKenzie and M. Bilek. "Thermodynamic theory for preferred orientation in
       materials prepared by energetic condensation". In: *Thin Solid Films* 382.1-2 (2001),
       pp. 280–287.

[60]   J. Almer, U. Lienert, R. L. Peng, C. Schlauer, and M. Odén. "Strain and texture
       analysis of coatings using high-energy X-rays". In: *Journal of applied physics* 94.1
       (2003), pp. 697–702.

Publications

5.1   List of included publications

1. Evolution of structure and residual stress of a fcc/hex-AlCrN multi-layered system upon thermal loading revealed by cross-sectional X-ray nano-diffraction

   N. Jäger, S. Klima, H. Hruby, J. Julin, M. Burghammer, J.F. Keckes, C. Mitterer, R. Daniel

   Acta Materialia 162 (2019) 55-66.

2. Microstructural evolution and thermal stability of AlCr(Si)N hard coatings revealed by in-situ high-temperature high-energy grazing incidence transmission X-ray diffraction

   N. Jäger, M. Meindlhumer, S. Spor, H. Hruby, J. Julin, A. Stark, F. Nahif, J. Keckes, C. Mitterer, R. Daniel

   Acta Materialia 186 (2020) 545-554.

3. Impact of Si on the high-temperature oxidation of AlCr(Si)N coatings

   N. Jäger, M. Meindlhumer, M. Zítek, S. Spor, H. Hruby, F. Nahif, J. Julin, M. Rosenthal, J. Keckes, C. Mitterer, R. Daniel

   Submitted to Journal of Materials Science & Technology.

5.2   Publications related to this work

4. Structure-stress relationships in nanocrystalline multilayered $Al_{0.7}Cr_{0.3}N/Al_{0.9}Cr_{0.1}N$ coatings studied by cross-sectional Xray nanodiffraction

   S. Klima, N. Jäger, H. Hruby, C. Mitterer, J.F. Keckes, M. Burghammer, R. Daniel

Materials and Design 170 (2019) 107702.

5. Stress-controlled decomposition routes in cubic AlCrN films assessed by in-situ high-temperature high-energy grazing incidence transmission X-ray diffraction

M. Meindlhumer, S. Klima, N. Jäger, A. Stark, H. Hruby, C. Mitterer, J. Keckes, R. Daniel

Scientific Reports 9 (2019) 18027.

6. Nanoscale residual stress and microstructure gradients across the cutting edge area of a TiN coating on WCCo

M. Meindlhumer, N. Jäger, S. Spor, M. Rosenthal, J.F. Keckes, H. Hruby, C. Mitterer, R. Daniel, J. Keckes, J. Todt

Scripta Materialia 182 (2020) 11-15

Publication I

Microstructural evolution and thermal stability of AlCr(Si)N hard coatings revealed by in-situ high-temperature high-energy grazing incidence transmission X-ray diffraction
N. Jäger, S. Klima, H. Hruby, J. Julin, M. Burghammer, J.F. Keckes, C. Mitterer, R. Daniel

Evolution of structure and residual stress of a fcc/hex-AlCrN multi-layered system upon thermal loading revealed by cross-sectional X-ray nano-diffraction

Jäger N.[a], Klima S.[a], Hruby H.[b], Julin J.[c], Burghammer M.[d], Keckes J.F.[e], Mitterer C.[f], Daniel R.[a]

[a]Christian Doppler Laboratory for Advanced Synthesis of Novel Multifunctional Coatings at the Department of Physical Metallurgy and Materials Testing,
Montanuniversität Leoben, Austria
[b]voestalpine eifeler Vacotec GmbH, Düsseldorf, Germany
[c]Institute of Ion Beam Physics and Materials Research at the Helmholtz-Zentrum Dresden-Rossendorf, Dresden, Germany
[d]ESRF, Grenoble Cedex, France
[e]Department of Materials Physics, Montanuniversität Leoben and Erich Schmid Institute for Materials Science, Austrian Academy of Sciences, Austria
[f]Department of Physical Metallurgy and Materials Testing, Montanuniversität Leoben, Austria

Abstract

Understanding the influence of process conditions and coating architecture on the microstructure and residual stress state of multi-layered coatings is essential for the development of novel thermally and mechanically stable coatings and requires advanced depth resolving characterization techniques. In this work, an arc-evaporated multi-layered coating, consisting of alternating $Al_{70}Cr_{30}N$ and $Al_{90}Cr_{10}N$ sublayers with an individual layer thickness between 120 nm and 380 nm, was investigated. The as-deposited state of the multi-layered coating and the state after vacuum annealing at 1000 °C for 30 min was studied along its cross-section by synchrotron X-ray nano-diffraction using a beam with a diameter of 50 nm. The results revealed sublayers with alternating cubic and hexagonal phase, causing repeated interruption of the grain growth at the interfaces. The in-plane residual stress depth distribution across the coating thickness could be tuned in a wide range between pronounced compressive and slight tensile stress by combining the effects of the coating architecture and the modulated incident particle energy controlled by the substrate bias voltage ranging from −30 V to −250 V. This resulted in an oscillatory stress profile fluctuating between −2 GPa and −4.5 GPa or pronounced stress gradients with values between −4 GPa and 0.5 GPa. Finally, the decomposition routes of the metastable cubic $Al_{70}Cr_{30}N$ phase could be controlled by the $Al_{90}Cr_{10}N$ sublayers which acted as nucleation sites and governed the texture of the decomposition products as Cr_2N. The results demonstrate that the cross sectional combinatorial approach, relying on a sophisticated multi-layer architecture combining various materials synthesized under tailored conditions, allowed for resolving structural variations and stress profiles in the individual layers within the complex architecture and pioneers the path for knowledge-based development of multi-layered coatings with predefined microstructure and a dedicated stress design.

Keywords: Coating, Multilayers, Microstructure design, Residual stress, X-ray nano-diffraction

1. Introduction

The development of ceramic hard coatings for severe applications has been considered as an important topic in materials research in the last decades, because of their outstanding properties such as high hardness, thermal stability and abrasion resistance. In particular, ternary and multinary coatings like AlCrN, AlTiN and CrAlSiN have been widely investigated with respect to their microstructure as well as thermal and mechanical properties [1–5]. AlCrN and AlTiN systems represent metastable solid solutions with a face centered cubic (NaCl-type) structure up to an Al content of around 70 at.% [6, 7] and 60 % [8] on the metal sublattice, respectively, depending on the process conditions. Exceeding the critical Al content results in the formation of a second, hexagonal dense packed (ZnS wurtzite-type) phase, or even in a single-phase wurtzite structure for very high Al contents. While the cubic structure exhibits a high hardness, the wurtzite structure is softer and more elastic [6]. The capability to synthesize hard, cubic and soft, hexagonal structures, depending on the amount of the al-

loying elements, makes the AlCrN system very interesting for the development of sophisticated, multi-layered materials with a high damage-tolerance. Ceramic hard coatings, as AlCrN, often exhibit high hardness and strength, but suffer from their low fracture toughness. This can lead to catastrophic failure when a crack is initiated and subsequently propagates through the whole sample already at small strains. Although strength and toughness are commonly exclusive properties, it is possible to develop damage-tolerant materials with high strength and high toughness by implementing structural and compositional heterogeneities in the material, as observed in biological [9, 10] and synthetic materials [11]. An established strategy for toughening is based on the combination of materials with structural and compositional heterogeneity, e.g. lamellar [11] or layered structures [9, 12]. The enhancement in fracture toughness in these materials is caused by an effective increase of energy dissipation through multiple crack deflection at the interfaces. Daniel et al. demonstrated the suitability of these concepts also for ceramic hard coatings by achieving an increase in the fracture toughness for multi-layered TiN/SiO_x and CrN/Cr coatings

[13].

For the development of such multi-layered coating systems, it is of vital importance to know not only the mechanical properties of the monolithic coatings, but also to investigate residual stress, texture and crystal structure in the individual components of the complex coating architecture. While the microstructure and properties of monolithic coatings are predominantly determined by the elemental composition and the process parameters during deposition [14, 15], they may be effectively controlled to a much wider extent by a sophisticated coating architecture [4, 16, 17]. Successful attempts to stabilize the metastable cubic NaCl high pressure polymorph of AlN by coherency strains within a CrN/AlN superlattice structure have been reported in [18], and there are other examples for such a structural effect demonstrated by Schlögl et al. [19, 20]. Besides the structure stabilization effect and the effect of interfaces in superlattice structures, a combination of materials differing in their microstructure and properties is also a promising approach to enhance the damage tolerance of materials [13, 17]. However, there are still many open questions, which role the microstructure and properties of individual substituents have on the microscopic and macroscopic properties of such complex systems. Therefore, local characterization of microstructure and properties is of vital importance in order to understand structure-property relationships of layered materials.

In this work, a recently developed X-ray nano-diffraction approach with a beam size of ~50 nm in diameter was used to position-resolve crystallographic texture, crystallite size and strains across the coating thickness [21]. By using this method, it was possible to reveal the influence of a layered structure on the crystallographic properties of a coating across the coating thickness. Here, $Al_{90}Cr_{10}N$ with hexagonal, and $Al_{70}Cr_{30}N$ with cubic crystallographic structure were combined in a multi-layered fashion with various thicknesses of the individual constituents and the results of the microstructure characterization across the coating thickness were compared with those of reference monolithic $Al_{90}Cr_{10}N$ and $Al_{70}Cr_{30}N$ coatings deposited under the same process conditions. The study revealed the impact of process conditions on the microstructure and texture of the monolithic reference coatings in comparison to the multi-layered coating, showing the influence of the complex architecture on microstructure and coating morphology, and demonstrates the capability of controlling the thermally induced decomposition of the thermodynamically metastable cubic AlCrN phase via systematic coating design.

2. Experimental methods

2.1. Coating deposition

In order to understand the complex relationships between microstructure, thickness and properties of individual constituents with respect to a macroscopic behaviour of the multi-layered coating, a cross-sectional combinatorial approach was applied. This allowed to study these relationships within one single sample. For this purpose, a multi-layered AlCrN coating, containing three parts with dedicated composition and architecture, was synthesized by cathodic arc evaporation using an

industrial-sized coating system (alpha400P, voestalpine eifeler Vacotec) and one-fold rotation. Mirror-polished cemented carbide was used as substrates. Prior to the deposition, the substrates were heated to 480 °C and plasma-etched, to remove all contaminants and to activate the substrate surface for better adhesion. Alternating sublayers with predicted cubic and hexagonal structure were deposited by using two sets of cathodes with elemental compositions of $Al_{70}Cr_{30}$ and $Al_{90}Cr_{10}$, respectively. The sublayers were deposited with thicknesses between 120 nm and 380 nm and under various incident particle energies controlled by the substrate bias voltage from −30 V to −250 V. Additionally, reference monolithic AlCrN coatings were deposited for comparison from the same cathodes and under the same conditions to investigate their intrinsic properties without the influence of the multi-layered structure. All coatings were grown in pure N_2 atmosphere at a total pressure of 4 Pa using a cathode current of 100 A for each cathode and a substrate temperature of about 480 °C.

2.2. Coating characterisation

The elemental composition of the reference monolithic coatings was determined by energy dispersive X-ray spectroscopy (EDX) under an acceleration voltage of 20 keV, using a scanning electron microscope (SEM) (ZEISS EVO50). Because of the limited detection accuracy of EDX for light elements, Elastic Recoil Detection Analysis (ERDA) was performed for the $Al_{90}Cr_{10}N$ and the $Al_{70}Cr_{30}N$ monolithic reference samples deposited at −100 V, to obtain precise information about the nitrogen and oxygen content in the coatings. An area of approximately 1.5 mm × 1.5 mm per sample was analysed using a 43 MeV $^{35}Cl^{7+}$ ion beam. The angle between the sample normal and the incoming beam was 75°, the scattering angle was 31°. The recoiling sample ions were detected using a Bragg Ionization Chamber (BIC), which enables energy measurement and atomic number identification of the recoils. To reveal the elemental composition of the individual layers within the multi-layered coating, an EDX mapping on the cross-sections of the coating was performed using a SEM (ZEISS Auriga) under a reduced acceleration voltage of 5 keV. It allowed to obtain a sufficient lateral resolution due to a smaller activation volume interacting with the electron beam. Cross-sections of the coatings for SEM imaging and EDX mapping were polished using a precision ion polishing system and Ar ions. The SEM micrographs of the coating cross-sections were recorded with an acceleration voltage of 2 keV using an InLens detector.

The crystallographic structure of the reference monolithic coatings was analysed using a Bruker D8 Advance diffractometer equipped with an energy-dispersive Sol-X detector and applying Cu-Kα radiation ($E = 8$ keV). While the $Al_{70}Cr_{30}N$ coatings were analysed using the Bragg-Brentano geometry, a grazing incidence configuration with a fixed incident angle of 2° was used to reduce the signal from the WC peaks from the substrate overlapping with the hexagonal AlN reflections.

The cross-sectional synchrotron X-ray nano-diffraction experiments were performed at the nanofocus extension of the ID13 beamline at the European Synchrotron Radiation Facility (ESRF) in Grenoble, France [22]. A slice of the sample

2

was cut using a high speed precision diamond saw and then mechanically polished in three steps using a decreasing size of the diamond suspension particles from 9 μm to 3 μm and finally 1 μm. The final thickness of the slice in beam direction was 30 μm. The sample was scanned in transmission geometry using a monochromatic X-ray beam ($E = 12.7$ keV) parallel to the coating-substrate interface (Figure 1). In order to scan the coating cross-section and measure the depth distribution of the crystallographic properties across the coating thickness, the sample was moved along the y axis in steps of 50 nm, matching the applied beam size adjusted using Kirkpatrick-Baez mirrors. The diffraction data were collected for each position, using a two-dimensional charge-coupled device detector, positioned at a distance of 100 mm behind the sample. Information about texture were obtained by analysing the intensity of the Debye-Scherrer rings along the azimuthal angle δ. The diffraction data were executed using the program package Fit2D [23]. While the in-plane elastic strain depth distribution was determined with an error smaller than 15 %, by analysing the elliptical shape of the Debye-Scherrer rings, the calculation of the residual stress profiles across the coating thickness strongly depends on the quality of the X-ray elastic constant $\frac{1}{2}s_2^{hkl}$ [21]. In the present case, $\frac{1}{2}s_2^{hkl} = 2.68 \times 10^{-6}$ MPa^{-1} was used for c-Al$_{70}$Cr$_{30}$N as calculated from cubic (c-) CrN [24] and c-AlN [25] assuming a Vegard's-like behaviour [26], and $\frac{1}{2}s_2^{hkl} = 3.67 \times 10^{-6}$ MPa [25] was used for hexagonal (h-) Al$_{90}$Cr$_{10}$N.

Characterisation of the multi-layered and monolithic coatings was furthermore performed after vacuum annealing at 1000 °C for 30 min, to investigate the influence of the coating architecture on the thermal stability, diffusion related phase transformations, changes in elemental composition and mechanical properties.
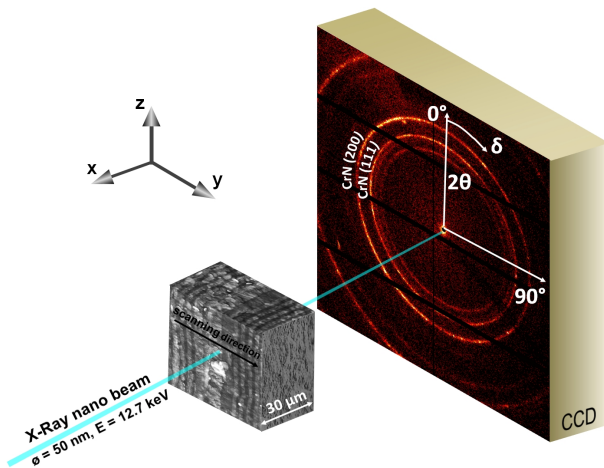

Figure 1: Schematic view of the synchrotron X-ray nano-diffraction experiment: A 30 μm thick lamella was scanned in transmission geometry using a monochromatic X-ray beam oriented parallel to the coating-substrate interface. The sample was moved along the y axis and diffraction data were collected for each position, using a two-dimensional charge-coupled device detector, positioned at a distance of 100 mm behind the sample.

3. Results

3.1. Coating architecture

The architecture of the multi-layered coating used for the cross-sectional combinatorial approach is schematically shown in Figure 2. The coating architecture consisted of three parts, which allowed to correlate process parameters, coating architecture and coating properties. The cathode composition and main variable deposition parameters, under which individual sublayers were deposited either from the Al$_{70}$Cr$_{30}$ or Al$_{90}$Cr$_{10}$ cathodes, are also given in Figure 2. While in part I, the parameters held constant during deposition were the layer thickness of ~120 nm and the substrate bias voltage of −100 V, in part II the thickness of the sublayers increased up to ~380 nm, to study the influence of layer thickness and number of interfaces on coating structure and stress state. In part III, substrate bias voltage variations were intended to reveal the role of the incident particle energy. While the substrate bias voltage was increased from −100 V to −250 V for the sublayers deposited with Al$_{70}$Cr$_{30}$ cathodes, with the intention to stabilize the cubic phase and simultaneously increase the hardness [4, 27], the substrate bias voltage was decreased from −100 V to −30 V for the sublayers with hexagonal structure deposited from Al$_{90}$Cr$_{10}$ cathodes, with the aim to reduce the overall residual stress in part III [28]. The SEM micrographs in Figure 2 show cross-sections of the sample in its as-deposited (a) and annealed (b) state. The individual sublayers deposited from the Al$_{70}$Cr$_{30}$ and Al$_{90}$Cr$_{10}$ cathodes can be distinguished as darker and brighter layers, which refers to the differences in their elemental composition.

3.2. Elemental composition

Table 1 summarizes the elemental composition of the monolithic reference coatings deposited at −100 V substrate bias voltage, obtained by ERDA. The measurements revealed nearly stoichiometric nitrides and indicated a slight loss of Al during deposition due to preferred resputtering, also confirmed by EDX measurements (not shown here).

In Figure 3, EDX maps of the cross-sections of the multi-layered coating in its as-deposited state (a-c) and after vacuum annealing (d-f) are shown. The elemental distribution of Al and Cr across the coating thickness revealed a change in the aluminium content between ∼ 45 at.% and ∼ 35 at.% in the alternating layers, corresponding to the Al/Cr ratio of the particular cathodes. The nitrogen content was found to be constant at ~50 at.% and uniformly distributed over the whole coating thickness.

Small areas with a deviating elemental composition observed at the coating cross-sections (denoted by arrows and circles in Figure 3) refer to macroparticles generated during deposition. Macroparticles typically eject out of the cathode surface from locally molten cathode material [29]. The composition of the macroparticles predominantly depends on the composition of the molten region of the cathode and may thus exhibit a high Al content while originating from the high Al-containing Al$_{90}$Cr$_{10}$ cathode (see Figure 3a-c, marked with arrows), or a higher Cr
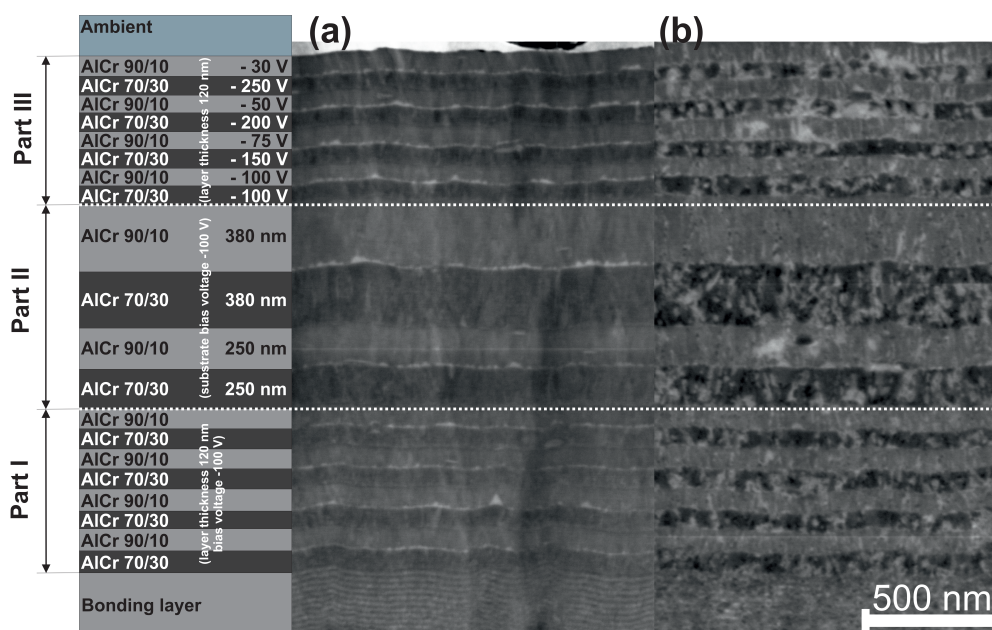
3

Figure 2: SEM micrographs of cross-sections of the multi-layered coating in the (a) as-deposited and (b) thermally annealed states. The schematic illustration of the coating architecture summarizes the main deposition parameters and composition of the cathodes used to deposit the individual sublayers.

Table 1: Elemental composition of the monolithic reference coatings deposited at -100 V substrate bias voltage, obtained by ERDA.

Coating	Composition [at. %]				Al/Cr coating	Al/Cr cathode
	Al	Cr	N	O		
$Al_{70}Cr_{30}N$	32.6	16.0	51.0	0.4	2.0	2.3
$Al_{90}Cr_{10}N$	41.9	4.8	53.0	0.2	8.7	9

content while originating from the $Al_{70}Cr_{30}$ cathode (Figure 3d-f, marked with circles). Since the reaction of the macroparticles with nitrogen is limited only to their surface and subsurface regions (as it may occur only during their exposure to nitrogen, i.e. during their flight from cathode to substrate or at the surface of the growing film), the macroparticles typically consist of a relatively nitrogen-rich rim and a pure metallic core [30]. The nitrogen deficiency within the core of the macroparticle with respect to the surrounding matrix is evidenced by Figure 3 (see the macroparticles marked with arrows and circles), confirming their metallic character which is also preserved after annealing [31].

3.3. Crystallographic structure

3.3.1. Crystallographic structure of reference monolithic coatings

The X-ray diffractograms in Figure 4 summarize the evolution of the crystallographic structure of the reference monolithic coatings in the as-deposited state (a, b) and after vacuum annealing at 1000 °C for 30 min (c, d). The monolithic $Al_{70}Cr_{30}N$ coatings exhibited a single-phase cubic structure in their as-deposited state, irrespective of the incident particle energy controlled by the substrate bias voltage (Figure 4a). The lattice parameter of all c-AlCrN coatings is 4.11± 0.01 Å, which is

slightly higher than that predicted by ab initio calculations [32], most likely due to compressive residual stress of the coatings. The magnitude of the residual stress seems to be rather independent of the substrate bias voltage (in the applied range from -100 V to -250 V), as indicated by almost identical peak positions for all monolithic $Al_{70}Cr_{30}N$ coatings (potentially superimposed peak shift resulting from differences in the elemental composition can be excluded due to the EDX measurements (not shown here)). A change in the orientation of the AlCrN crystallites from a preferred (111)-direction at -100 V substrate bias voltage to a preferred (100)-direction above -150 V shows the capability of the deposition conditions to control the growth conditions and subsequently the coating microstructure.

Since the nominal Al content of 45 at.% in the coating already exceeds the solubility limit of AlN in the cubic AlCrN phase, all $Al_{90}Cr_{10}N$ coatings show a single hexagonal structure, irrespective of the applied substrate bias voltage and corresponding incident particle energy (Figure 4b). On the other hand, the effect of the incident particle energy on the orientation and strain of the grains of the $Al_{90}Cr_{10}N$ coatings is evidently stronger than observed for the cubic $Al_{70}Cr_{30}N$ coatings. While the grains of the $Al_{90}Cr_{10}N$ coatings grown at the bias voltage of -30 V are highly (001) oriented, rather randomly oriented grains developed at substrate bias voltages above -75 V. An
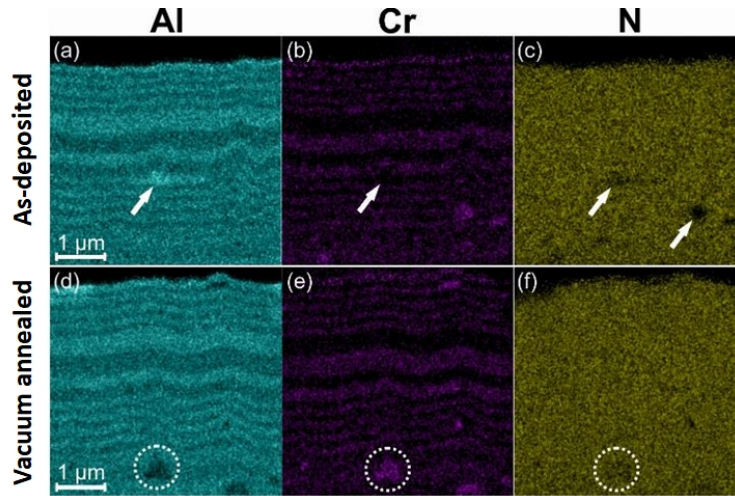
Figure 3: EDX mapping comprising Al, Cr and N across the coating thickness of (a-c) the as-deposited state and (d-f) the vacuum annealed state of the sample. Al-rich and Cr-rich macroparticles are marked with arrows and circles, respectively.

increase in the incident particle energy is furthermore reflected by a pronounced peak shift to lower 2θ angles, corresponding to the increase of the lattice parameter associated with higher in-plane compressive residual stress in the coating (see the (002) peak in Figure 4b). A further evidence of a strong effect of the incident particle energy on coating growth is the observed significant peak broadening with increasing substrate bias voltage, reflecting a reduction of the grain size and an increase of the defect density due to enhanced collisions of incident particles with the coating surface.

The structure development of monolithic reference coatings after annealing at 1000 °C in vacuum for 30 min is shown in Figure 4c-d. While the applied heat treatment of the thermo-dynamically metastable $Al_{70}Cr_{30}N$ coatings led to a partial de-composition of c-AlCrN into c-CrN and h-AlN (Figure 4c), the $Al_{90}Cr_{10}N$ coatings preserved their thermodynamically stable hexagonal structure after annealing (Figure 4d). The decomposition of c-AlCrN, controlled by diffusion driven Al segregation and subsequent formation of h-AlN is, in addition, accompanied by the formation of Cr-enriched c-Cr(Al)N regions. For these Cr-enriched regions, a sufficient driving force for a further decomposition into h-Cr_2N is obtained, accompanied by the release of nitrogen [2]. The formation of h-Cr_2N is indicated by the peak at ~43° in Figure 4c. The thermal treatment also resulted in recovery of deposition-induced lattice defects and grain growth, which is reflected by a reduced full width at half maximum (FWHM) of the diffraction peaks (Figure 4c, d). The defect annihilation was also accompanied by a relaxation of the compressive residual stress, indicated by a peak shift to higher 2θ angles.

3.3.2. Crystallographic structure of the multi-layered coating

To investigate the effect of the multi-layered architecture on the crystallographic structure and stress state of the individual $Al_{70}Cr_{30}N$ and $Al_{90}Cr_{10}N$ layers, position resolved character-ization of the multi-layered coating was performed by cross-sectional X-ray nano-diffraction. The use of a 2D detector allowed recording full Debye-Scherrer rings in 50 nm steps across the coating thickness, which reflects, contrary to labo-ratory conditions, the full orientation distribution of the grains in space. Figure 5 illustrates the normalized X-ray diffraction intensity distribution depth plots of the h-(100) and the c-(200) peaks of the multi-layered coating in the as-deposited state (Figure 5a) and after vacuum annealing at 1000 °C (Figure 5b) as a function of the diffraction angle 2θ. The data for Figure 5 were obtained by 2θ integration of the entire Debye-Scherrer rings, thus including information of the whole grain orienta-tion distribution. The spatial resolution of the method using a 50 nm X-ray beam allowed for resolving the sublayers within the multi-layered architecture of the coating (Figure 5). The sublayers in Figure 5 exhibit an alternating cubic and hexag-onal crystal structure for the $Al_{70}Cr_{30}N$ and $Al_{90}Cr_{10}N$ layers, respectively. While Figure 5 shows the integrated signal over the entire Debye-Scherer rings (δ from 0° to 360°) and therefore provides an averaged imprint of the full orientation distribution of the grains in space, diffraction plots of selected segments of the Debye Scherrer rings given in Figure 6 allow deeper insights into the microstructure of the multi-layered coating, i.e. crystal-lographic structure and texture. In Figure 6, data corresponding to the crystallographic planes oriented parallel to the coating-substrate interface ($\delta = 0 \pm 10°$) and those tilted of $54 \pm 10°$ were evaluated, allowing for analysis of crystallographic tex-ture. Crystallites oriented parallel to the coating-substrate in-terface represent the typical preferred orientation of coatings prepared by physical vapour deposition (PVD) processes [37]. The data in Figure 6a reveals a preferred (111) orientation of the cubic crystallites with planes parallel to the coating-substrate interface within parts I and II of the multi-layered coating, de-posited at −100 V substrate bias voltage. With increasing sub-strate bias voltage from −100 V to −250 V within part III, a
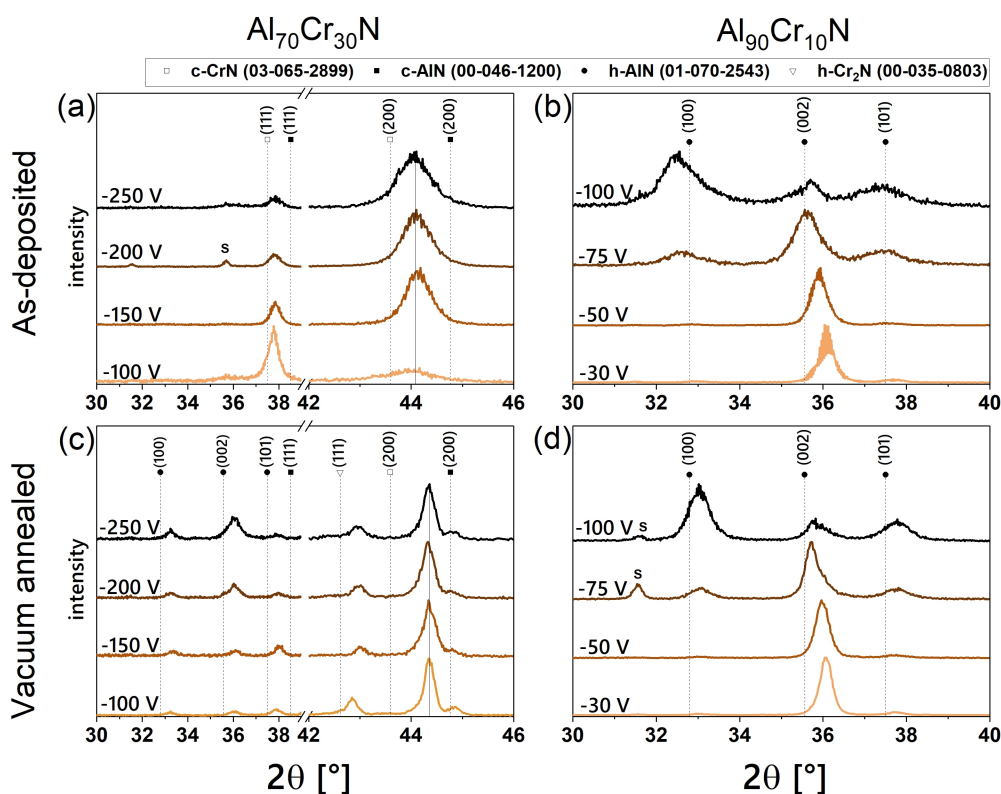
Figure 4: X-ray diffractograms of the reference $Al_{70}Cr_{30}N$ and $Al_{90}Cr_{10}N$ monolithic coatings deposited at various substrate bias voltages in the (a), (b) as-deposited and (c), (d) vacuum annealed states, respectively. ("S" indexes diffraction peaks emanating from the substrate) [33–36]

change in preferred orientation from c-(111) to c-(100) was observed, which corresponds to a gradual development of the (100)-oriented crystallites at the extent of those with the (111) orientation (Figure 6a) at higher incident ion energies [38]. This effect is visible also in Figure 6b. The microstructure of the layers with hexagonal crystallite structure showed a texture development from randomly oriented grains at −100 V bias voltage (part I and II), to preferentially oriented (001) grains with decreasing bias voltage, as seen in part III of the coating (Figure 6a). The (002)-peak is not visible in Figure 6b, indicating the small number of crystallites oriented at an angle of $\delta = 54°$ to the coating-substrate interface, which confirms the strongly pronounced texture of the hexagonal phase.

The study of the microstructure of the same coating after annealing allowed to reveal the influence of the multi-layer arrangement on the thermal stability of the individual layers. Recovery processes acting at temperatures slightly above the deposition temperature lead to annihilation of deposition-induced lattice defects, responsible for a compressive residual stress state [2]. The reduced defect density is reflected by an increased intensity of the h-(111) and the c-(200) peaks, simultaneously accompanied by a reduced peak width (Figure 5c). Furthermore, the thermodynamically metastable cubic AlCrN phase decomposed into c-CrN and h-AlN, indicated by the formation of a h-AlN phase in Figure 5c, which evidently oc-

curred in the individual parts of the coating to a different extent. A pronounced increase in the intensity of the h-(111) peak together with a decrease of the c-(200) peak intensity along part III, with a maximum intensity of the h-(111) peak close to the coating surface, is visible in Figure 5c. In Figure 6c and d, a peak at $2\theta \approx 21.6°$ appeared, corresponding to the Cr_2N phase, which formed after nitrogen release from the c-CrN phase during the decomposition process at temperatures of $\sim 1000 °C$ [2, 39]. While almost no Cr_2N crystallites oriented parallel to the coating-substrate interface can be found in the layers deposited at −100 V substrate bias voltage, they are more obvious in the layers deposited at higher incident particle energies (part III in Figure 6c). The highest intensities of the h-Cr_2N peak in Figure 6c, d can be found near to the coating surface.

3.4. Crystallite size and morphology

Fracture cross-sections of the multi-layered coating in its as-deposited and annealed state show a columnar microstructure of the individual layers characterized by needle-like grains oriented perpendicular to the individual layer interfaces (Figure 7). The size of the columnar grains was limited by the thickness of the sublayers and the grain growth is interrupted at the interfaces of the individual layers. The h-$Al_{90}Cr_{10}N$ layers (dark) are composed of finer grains compared to the c-$Al_{70}Cr_{30}N$ lay-
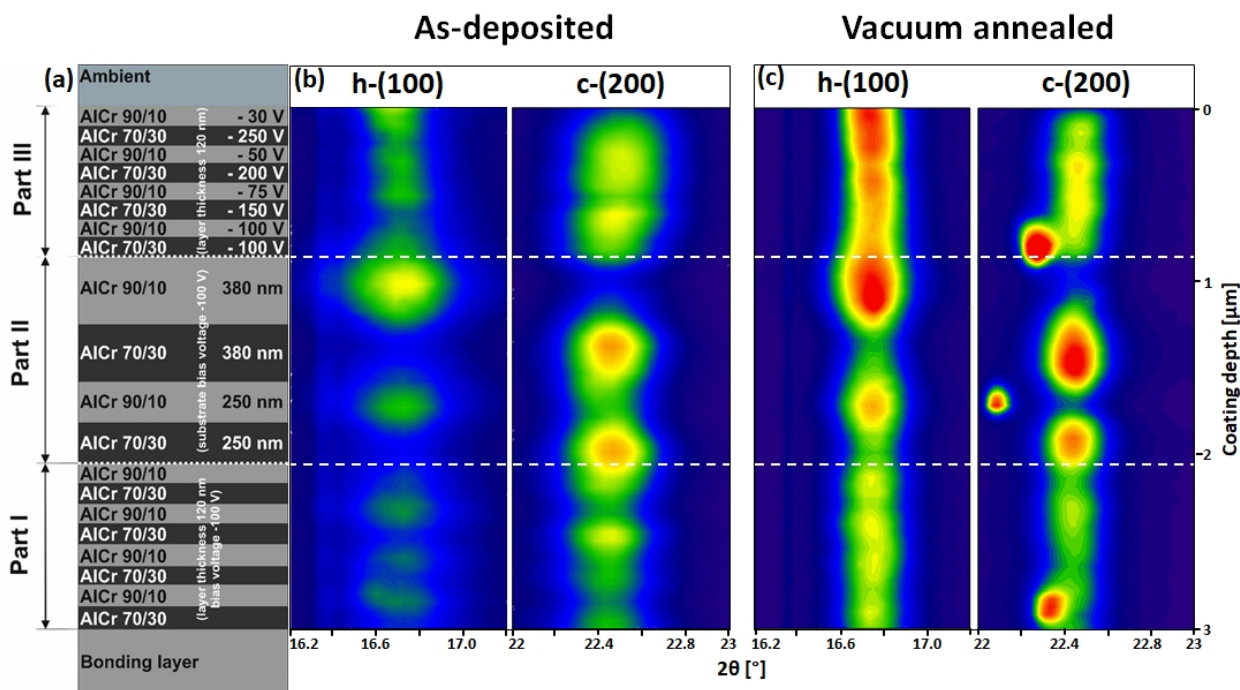
6

Figure 5: (a) Schematic of the coating architecture, (b) the intensity of the h-(100) and the c-(200) peaks across the coating thickness of the as-deposited and (c) at 1000 °C vacuum annealed sample. The three spikes with lower 2θ angles at the c-(200) peak in (b) refer to macroparticles with reduced Al content.

ers (bright). The fracture surfaces revealed also local differences in the fracture behaviour across the coating thickness associated with the variation of the incident particle energy during coating growth. While for the parts deposited at a bias voltage of −100 V (parts I and II) an increase in roughness of the fractured surface was observed, the fracture surface of part III (substrate bias variation) remains smoother. Additionally, parts I and II differ in the appearance of single grains within the sublayers, indicating a more pronounced intergranular fracture behaviour compared to part III. These effects are more significant after the annealing (Figure 7b), which is governed by the structural changes associated with the defect recovery and phase decomposition discussed above. Additionally, the coating exhibited a slightly coarser grained microstructure with even more pronounced interfaces between the individual layers.

Spatial-resolved X-ray nano-diffraction characterization allows, besides the phase analysis, also a detailed study of the grain size and defect density across the coating thickness. The analysis is based on the evaluation of the FWHM of the diffraction peaks corresponding to the size of coherently diffracting domains and the strains of the second and third order. In Figure 7, the FWHM values of the h-(100) and c-(200) peaks, corresponding to the grains of the h-$Al_{90}Cr_{10}$N and the c-$Al_{70}Cr_{30}$N layers, respectively, are plotted across the coating thickness. The parts I and II of the coating are characterized by nearly constant FWHM values indicating an invariable grain size and defect density within these parts. In part III, the effect of the incident particle energy on the coating microstructure is

demonstrated. While the FWHM of cubic grains within sub-layers deposited from $Al_{70}Cr_{30}$ cathodes is not much affected by enhanced particle bombardment at the bias voltage ranging from −100 V to −250 V, FWHM of the h-(100) peak gradually increases with increasing incident particle energies corresponding to the bias voltage variation from −30 V to −100 V. Analysis of the FWHM values corresponding to the in-plane ($\delta = 0°$) and out-of-plane ($\delta = 90°$) diffraction allowed for the reconstruction of the shape of the grains. Higher FWHM values for the out-of-plane than for the in-plane direction, irrespective of the phase composition and as-deposited or annealed state, are associated with a needle-like shape of the grains. This is in a good agreement with the results of the SEM analysis. A decrease of FWHM after vacuum annealing at 1000 °C (Figure 5c) reflects recovery of growth defects and possible growth of the grains.

3.5. Stress evolution

Besides the possibility to characterize phases and microstructure across the coating thickness, cross-sectional X-ray nano-diffraction allows also for depth-resolved determination of elastic strains and subsequent calculation of the residual stress state. Since the sample thickness of 30 μm (in beam direction) is a few times the coating thickness of 4 μm, a stress relaxation due to sample cutting can be neglected and the measured stresses represent the original stress state of the coating before cutting [40].

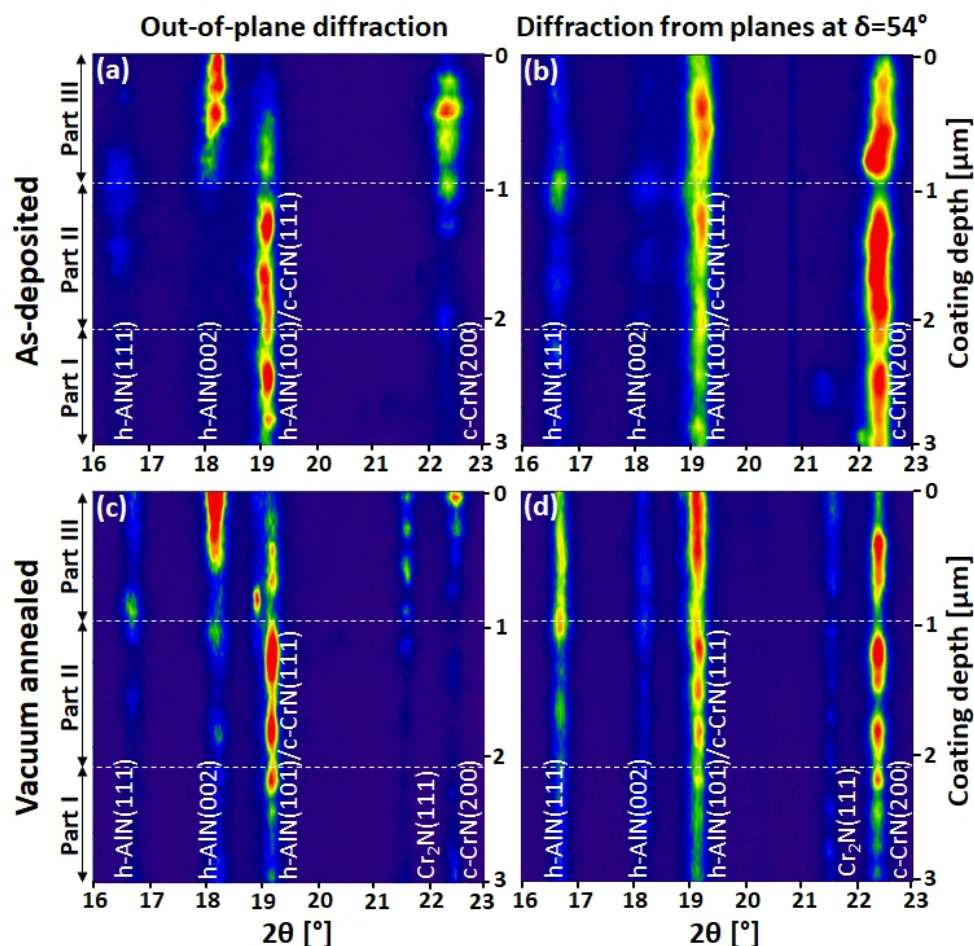High-energy incident particles arriving at the coating surface

7

Figure 6: Phase plots of (a,b) out-of-plane diffracting crystallites, and (a,c) for planes at $\delta = 54°$ of the (b,d) as-deposited state and (c,d) the at 1000 °C vacuum annealed state of the multi-layered coating.

during PVD processes typically generate lattice defects and subsequently compressive stress. Besides deposition induced lattice defects, the development of residual stress throughout the coating is also affected by the presence of adjacent sublayers, when coherency strains develop due to a lattice mismatch between different phases of the sublayers. Additionally, the thermal expansion mismatch of coating and substrate contributes to the residual stress state of the coating. The development of biaxial in-plane residual stress in the individual cubic and hexagonal phases as a function of the coating thickness is shown in Figure 8. In the as-deposited state, all individual sublayers are compressively stressed, although the stress magnitude is not constant and varies across the coating thickness. In part I of the coating, where an uniform substrate bias voltage of −100 V was applied for all sublayers, the residual stress in both phases remains nearly constant at −3 GPa. With an increase of the sublayer thickness from 120 nm to 380 nm, multiple measurements with the focused X-ray beam (50 nm of diameter) were done revealing stress variations even within the

individual sublayers, as shown for Part II of the coating in Figure 8. Since the sublayers in part II were all deposited at constant process conditions (temperature, pressure and a substrate bias voltage of −100 V), the development of the residual stress is rather dominated by the individual layer composition and the coating architecture. The compressive stress increases within the layers with a dominating hexagonal $Al_{90}Cr_{10}N$ phase and it decreases within the layers dominated by the cubic $Al_{70}Cr_{30}N$ phase, which resulted in a zigzag like stress variation between −2.5 GPa and −4.5 GPa. In part III, the stress variation across the coating thickness is mainly governed by the incident particle energy, controlled by the substrate bias voltage, and the alternating layer composition. While the compressive residual stress in the $c\text{-}Al_{70}Cr_{30}N$ layers, deposited at increasing substrate bias voltages from −100 V to −250 V, was only slightly reduced from −2.5 GPa to −1.5 GPa, a more pronounced decrease can be observed for the $h\text{-}Al_{90}Cr_{10}N$ layers, were the compressive stress of −3.5 GPa decreases and reaches, even slight tensile stress (0.5 GPa) within the top layer, deposited at the lowest
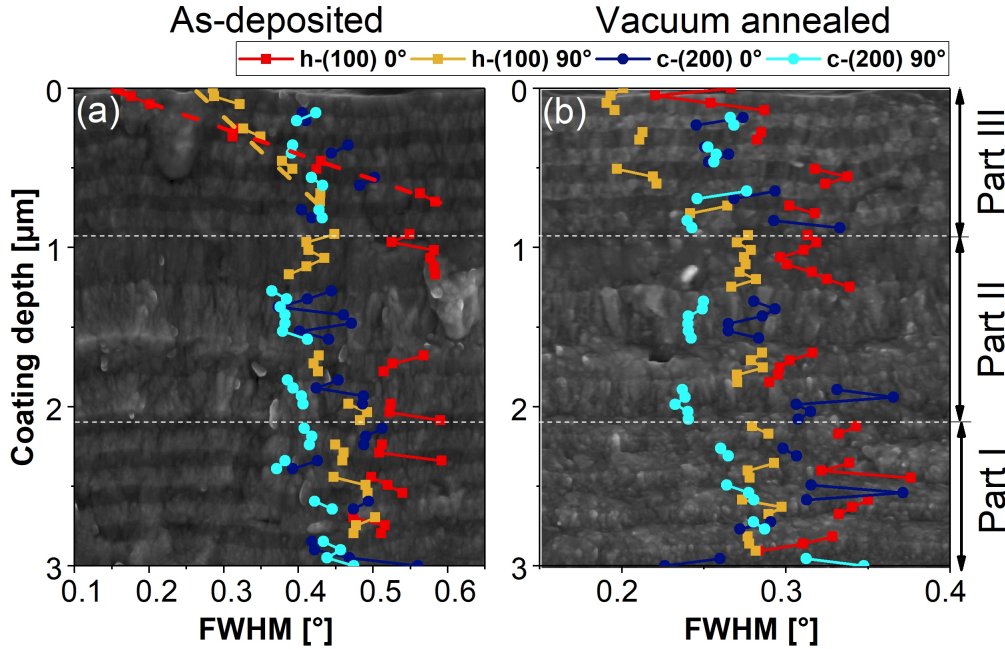
Figure 7: SEM fracture cross-sections of the multi-layered AlCrN coating and FWHM data obtained by X-ray nano-diffraction across the coating thickness in the (a) as-deposited state and (b) after vacuum annealing. The FWHM values are given for the h-(100) (red squares) and the c-(200) (blue dots) peak for the in-plane (δ = 0°, bright symbols) and out-of-plane (90°, dark symbols) orientation.

substrate bias voltage of −30 V.

After vacuum annealing, annihilation of lattice defects led to an overall reduction of the compressive residual stress, becoming even tensile in the upper part of the coating. In part I, a relaxation of ~2 GPa led to reduced compressive stress slightly below −1 GPa in both phases. In part II, the zigzag stress profile was preserved, only the values of residual stress state decreased, reaching even tensile stress of 1 GPa at the coating depth of 1.5 μm. Within part III, an almost complete relaxation of the stress in the c-$Al_{70}Cr_{30}$N layers caused a shift from pronounced compressive (−2 GPa) to slight tensile stress below 0.5 GPa for the cubic phase. The distinctive stress gradient of the h-$Al_{90}Cr_{10}$N layers was diminished, with stresses ranging from −1.5 GPa to 0 GPa after annealing.

4. Discussion

4.1. Development of the coating microstructure and phase stability upon thermal loading

The crystallite growth of thin coatings deposited using PVD techniques strongly depends on the process conditions (such as substrate bias voltage, temperature and pressure) and on the surface where the coating nucleates and grows. The latter effect can be effectively controlled by selection of a specific crystallographic template (substrate material [41] or sublayer [42]) or by a combination of materials which significantly differ in their microstructure. One example is the stabilisation of AlN in its metastable cubic NaCl high pressure polymorph by coherency strains in a CrN/AlN multi-layered arrangement reported by

Lin et al. [43]. Despite of the relatively small difference in the elemental composition of individual layers in the multi-layered architecture studied in this work, the layers deposited from the $Al_{70}Cr_{30}$ cathodes exhibited cubic structure, while the $Al_{90}Cr_{10}$N layers form a hexagonal structure, irrespective of the multi-layered architecture (Figure 5). The reason for that is, that once the solubility limit of AlN in CrN is exceeded in the h-$Al_{90}Cr_{10}$N layers, the cubic structure may hardly be stabilized at thicknesses above a few nanometres [43]. The phase composition of individual layers of the multi-layered coating thus corresponds to that of the reference monolithic coatings (see Figure 5 and 6). The data presented in Figure 6 confirm that the individual layers within the complex multi-layered coating exhibit comparable microstructure in terms of size and orientation of the crystallites to the reference monolithic coatings. The dependence of the microstructure of the individual layers on the incident particle energy controlled by the substrate bias voltage is similar to that of the monolithic reference counterparts. The c-$Al_{70}Cr_{30}$N sublayers grow fiber textured with (111) planes oriented parallel to the coating-substrate interface for an applied bias voltage of −100 V (parts I and II). When increasing the bias voltage up to −250 V in part III, the (111) texture smoothly transforms into the (100) fiber texture. This texture evaluation is in good agreement with the effects seen for the reference monolithic coatings in Figure 4a. The texture development is likely associated with the formation of admolecules with limited mobility on the growing surface [42]. In contrast, randomly oriented grains of the hexagonal phase developed in parts I and II of the h-$Al_{90}Cr_{10}$N layers at −100 V,
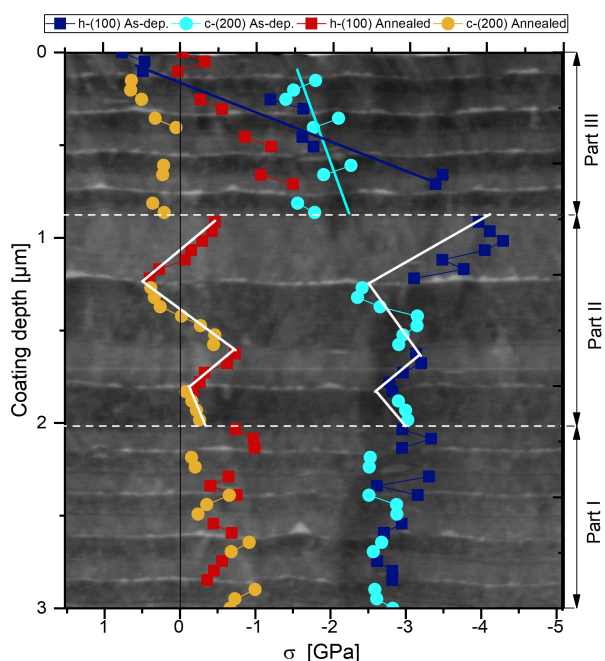
Figure 8: Development of the in-plane residual stress across the coating thickness, determined for the hexagonal (squares) and the cubic phase (circles) in the as-deposited (blue symbols) and vacuum annealed (red symbols) state of the sample. The stress depth distribution documents (i) constant stress for part I, (ii) an oscillatory stress profile in part II (accented by white lines) and (iii) distinct stress gradients in part III (marked by blue lines)

which changed the orientation towards (001) with a decreased bias voltage to −30 V within part III of the multi-layered coating. This texture development can be correlated with the evolution of the residual stress state. While randomly oriented grains formed in regions with high compressive stress around −3 GPa in part I and II, predominantly (001) oriented grains evolved in part III as a result of the decreasing compressive stresses. As stated by McKenziel and Bilek [44], preferred orientations may arise from the thermodynamic principle of energy minimisation including the strain energy associated with intrinsic residual stress. Similar dependencies between texture and residual stress state were also found for pure AlN [45, 46]. The development of the microstructure of the multi-layered coating again correlates with the reference monolithic coatings and demonstrate the strong effect of the incident particle energy on the development of the coating microstructure. These findings indicate that the impact of the process parameters on the microstructure, i.e. crystallographic structure and texture, of the multi-layered coating with individual layer thickness greater than 120 nm, is much stronger than that of the crystallographic template given by the multi-layered architecture of the coating.

The decomposition of c-AlCrN as a function of the coating composition, microstructure and stress state is well documented in literature [2, 3, 5, 8, 39]; however, relatively little is known about the effect of the combination of thermally stable h-AlCrN and metastable c-AlCrN constituents in a multi-

layered architecture on their thermal stability. A combination of conventional X-ray diffraction and X-ray nano-diffraction experiments applied for the vacuum annealed monolithic reference and multi-layered AlCrN coatings allowed to identify differences in the thermal stability of the metastable c-AlCrN as a monophase structure and as structure confined within the multi-layered coating. Furthermore, the effect of the incident particle energy associated with corresponding stress build-up in the c-AlCrN system on its thermal stability was revealed. At elevated temperatures, decomposition of c-AlCrN generally leads to the formation of a hexagonal AlN phase [2]. An increasing intensity of the ion bombardment destabilized the cubic phase and promoted decomposition, observable for the monolithic cubic $Al_{70}Cr_{30}N$ reference coatings in Figure 4c and for the multi-layered coating within part III in Figure 5. The vacuum annealed multi-layered coating exhibited an increasing amount of formed hexagonal phase with increasing substrate bias voltage applied for the c-$Al_{70}Cr_{30}N$ layers within part III, reflected by an increased intensity of the h-(111) peak and simultaneously decreased c-(200) peak visible in Figure 5. The impact of incident particle energy on the destabilisation of the c-$Al_{70}Cr_{30}N$ phase can be explained by the formation of compressive residual stress. As shown by Schalk et al. for the similar TiAlN system [47], compressive residual stress stabilizes the cubic phase against decomposition into the more volume consuming hexagonal phase. Regarding to part III in Figure 8, the residual stress decreased with increasing substrate bias voltage within the individual cubic layers (discussed more detailed in subsection 4.3), which promoted its decomposition. Decomposition of c-AlCrN into h-AlN and c-CrN at high temperatures led to the formation of Cr enriched regions within the coating, where furthermore a sufficient driving force for a continued decomposition of c-CrN into h-Cr_2N was obtained. The formation of Cr_2N obviously depends on the amount of formed c-CrN during decomposition, which especially becomes evident from the intensity development of the (111) Cr_2N peak across the coating thickness in part III of the coating, corresponding to the increase of substrate bias voltage (Figure 6c). The highest intensities of the h-Cr_2N peaks in Figure 6c, d were found for the $Al_{70}Cr_{30}N$ deposited at −250 V, located at the very top of the coating.

Besides the process conditions during deposition, also the multi-layered architecture of the coating had an influence on the microstructure development during annealing. The h-AlN and h-Cr_2N phase, which formed during annealing in the monolithic c-$Al_{70}Cr_{30}N$ reference coatings, exhibited no specific texture (Figure 4c). Unlike the monolithic reference coatings, an influence of the coating architecture on the texture of the phases formed during decomposition becomes evident by comparing the peaks of the hexagonal phase ((111), (002) and (101)) before (Figure 6a) and after vacuum annealing (Figure 6c). A similar shape of the peaks with identical intensity development across the coating thickness is visible. Furthermore, out-of-plane oriented crystallites of the h-Cr_2N phase are merely observed in part III of the coating, indicating a change of texture along the coating thickness. Because the texture development of h-Cr_2N of the annealed reference monolithic coatings is independent of the originating coating texture, an influence

of the coating architecture has to be assumed for the multi-layered coating. Decomposition of c-AlCrN starts with the nucleation of h-AlN participates preferably at grain boundaries [48]. For the multi-layered coating, energy of formation for the nucleation of the h-AlN domains within the cubic layers can be reduced, if the growth starts at the layer interfaces between the individual c-Al$_{70}$Cr$_{30}$N and h-Al$_{90}$Cr$_{10}$N layers, where the hexagonal phase is already present when decomposition begins. This growth behaviour is confirmed by the shape of the formed h-AlN participates (bright spots) within the c-Al$_{70}$Cr$_{30}$N layers (dark) for the vacuum annealed state of the sample in Figure 2b. Here, most of the h-AlN domains are connected with the layer interfaces, especially for the thinner layers with ~120 nm thickness. These findings demonstrate that the decomposition route of c-Al$_{70}$Cr$_{30}$N can be controlled by the combination of selected materials in a dedicated coating architecture.

4.2. Development of the coating morphology

Nanocrystalline coatings prepared by PVD typically grow under highly non-equilibrium conditions, where atomistic processes acting on the surface of the growing deposits are controlled by kinetic restrictions predominate thermodynamics [42]. This frequently results in a microstructure with V shaped grains [49] and often unfavourable coating properties. The specific shape of the columnar grains is given by competitive growth of adjacent grains differing in their orientations. Unlike monolithic coatings, where the columnar microstructure proceeds across the entire coating thickness, growth of the columnar grains in the multi-layered coating is limited by the thickness of individual layers (Figure 7). The resulting sharp interfaces evident in Figure 7 demonstrates the interruption of the columnar growth at the interfaces between the layers exhibiting cubic and hexagonal structure. The repeated interruption of the competitive grain growth at the layer interfaces leads to constant FWHM in part I and II for both phases, indicating a constant grain size (and defect density) across the coating thickness (Figure 7). Within part III, the FWHM of the h-(100) peak strongly decreases due to a reduction of irradiation-induced defects resulting from a reduced energy of the incident particles caused by the substrate bias voltage decreasing from −100 V to −30 V. The increase in substrate bias voltage from −100 V to −250 V does not affect the defect density in the individual cubic layers. This indicates that at such high incident particle energies, defect generation is in balance with recovery effects caused by the high adatom mobility accompanied by enhanced surface diffusion.

4.3. Development of residual stress

The total residual stress σ_{tot} in nanocrystalline coatings is given by

$$\sigma_{tot} = \sigma_i + \sigma_{th} + \sigma_e. \tag{1}$$

While the effect of the extrinsic stress component σ_e stems from structural misfits, phase transformations, precipitation and chemical reactions, the intrinsic stress σ_i are related to the deposition conditions controlling atomistic processes during film growth. Additionally, differences in the thermal expansion coefficient (TEC) between coating and substrate or individual phases lead to thermal residual stress σ_{th} during cooling down from deposition to room temperature. Since the TEC of the cemented carbide substrates used in this work was smaller than the TEC of the AlCrN-based coating, tensile thermal residual stress developed. The intrinsic stress comprises of many components [50], whereof the generation of point defects due to ion bombardment during film growth, resulting in a volume increase and thus the development of compressive stress, represents typically the dominant contribution. Within part I of the coating, deposited at a constant substrate bias voltage of −100 V, the total residual stress is constant for the hexagonal and the cubic phased AlCrN layers (Figure 8). In part II, stress gradients within the individual sublayers were observed, revealing a zigzag like stress variation. Since all layers were deposited at a constant substrate bias voltage of −100 V, the combination of layers with different elemental composition and hence different phases is the reason for this oscillatory stress profile. When deposited as a monolithic reference at −100 V, the hexagonal phased Al$_{90}$Cr$_{10}$N coating exhibits −4.9 GPa compressive stress, while for the cubic phased Al$_{70}$Cr$_{30}$N coating −3.5 GPa were observed. Combined in the multi-layered architecture, a repeated residual stress field along part II was formed with increasing compressive stress within the layers with a dominating hexagonal phase and decreasing stress within the cubic phased layers. The largest stress gradients within the multi-layered coating were found in part III, demonstrating the strong impact of the deposition conditions on the formation of residual stress also in multi-layered coatings with complex architecture. Simultaneously with the decreasing substrate bias voltage applied for the h-Al$_{90}$Cr$_{10}$N layers, the compressive residual stress strongly decreased becoming even tensile for the top layer deposited at −30 V. This can be related to the less defective crystalline structure as a result of the reduced energy of impacting particles at lower substrate bias voltages. In the top layer, the tensile component of the thermal stress exceeds the low compressive intrinsic stress component, leading to an overall tensile stress state. Contrary to the h-Al$_{90}$Cr$_{10}$N layers, the c-Al$_{70}$Cr$_{30}$N layers were deposited at substrate bias voltages increasing from −100 V to −250 V within part III, which also results in decreasing compressive stress, although much less pronounced compared to the hexagonal phased layers. An increase of the substrate bias voltage typically leads to a rising number of lattice defects, resulting in increased compressive residual stress, as seen for the h-Al$_{90}$Cr$_{10}$N layers within part III. The substrate bias voltages up to −250 V applied for the cubic layers in part III of the coating were remarkably high, causing an exceptional increase of adatom mobility accompanied by enhanced surface diffusion. Therefore, a saturation of the defect density resulting in a slight decrease of compressive residual stress was observed. These findings are supported by constant FWHM values of the cubic phase across the whole coating thickness in Figure 7.

At temperatures above decomposition temperature, recovery processes lead to decreasing number of the deposition-induced lattice defects and thus to a reduction of the intrinsic compres-

11

sive stress component [2]. Since the thermal tensile stress remained unchanged after annealing, an overall shift towards the tensile regime of the total residual stress is observed in Figure 8. The magnitude of the stress relaxation is mainly controlled by the defect density in the as-deposited state, as demonstrated for the h-$Al_{90}Cr_{10}N$ layers in part III. Here, the reduced energy of incident ions (controlled by substrate bias voltage) led to a reduction of lattice defects accompanied by decreasing compressive stress in the as-deposited state. This stress gradient is much less pronounced after vacuum annealing, since recovery effects annihilated most of the deposition induced lattice defects. Nevertheless, the oscillatory stress profile of part II and the distinct stress gradients within part III were preserved even after annealing, demonstrating that the dedicated stress profile generated by the systematic coating design can be preserved to temperatures up to 1000 °C.

5. Summary and conclusion

The relation between microstructure and process conditions in cathodic arc deposited monolithic and multi-layered AlCrN coatings was studied. As-deposited and at 1000 °C vacuum annealed samples were investigated concerning crystal structure, texture development, coating morphology and residual stress state. The process parameters, especially substrate bias voltage, affect the microstructure of monolithic and multi-layered coatings in a similar way. For a minimum single layer thickness of ~120 nm, the microstructure of the individual layers within the multi-layered coating develops equivalently to the monolithic coatings with corresponding elemental composition. The multi-layered architecture (i) affects the coating due to interruption of the columnar grain growth at interfaces of layers exhibiting different phases (ii) governs the decomposition of the metastable c-AlCrN and influences the microstructure of the phases formed during annealing and (iii) shapes the development of the stress profile across the coating depth resulting in zig-zag like stress profiles and distinct stress gradients. By arranging the individual constituents with specific elemental composition in a dedicated coating architecture and simultaneously adapting the process parameters during composition, it is possible to deposit multi-layered coatings with a defined microstructure and a modulated stress design. Multi-layered architectures can thus be used to generate advanced coatings by regulating grain size, morphology and stress design and controlling the microstructure of decomposition products formed at elevated temperatures.

6. Acknowledgements

7. References

References

[1] C. Tritremmel, R. Daniel, M. Lechthaler, P. Polcik, and C. Mitterer. Influence of Al and Si content on structure and mechanical properties of arc evaporated Al–Cr–Si–N thin films. *Thin Solid Films*, 534:403–409, 2013.

[2] H. Willmann, P. H. Mayrhofer, P.O.Å. Persson, A. E. Reiter, L. Hultman, and C. Mitterer. Thermal stability of Al–Cr–N hard coatings. *Scripta Materialia*, 54(11):1847–1851, 2006.

[3] H. Willmann, P. H. Mayrhofer, L. Hultman, and C. Mitterer. Thermal stability and age hardening of supersaturated AlCrN hard coatings. *International Heat Treatment and Surface Engineering*, 1(2):75–79, 2013.

[4] C. Sabitzer, J. Paulitsch, S. Kolozsvári, R. Rachbauer, and P. H. Mayrhofer. Impact of bias potential and layer arrangement on thermal stability of arc evaporated Al-Cr-N coatings. *Thin Solid Films*, 610:26–34, 2016.

[5] M. Bartosik, R. Daniel, C. Mitterer, and J. Keckes. Thermally-induced formation of hexagonal AlN in AlCrN hard coatings on sapphire: Orientation relationships and residual stresses. *Surface and Coatings Technology*, 205(5):1320–1323, 2010.

[6] M. Kawate, A. Kimura, and T. Suzuki. Microhardness and lattice parameter of $Cr_{1-x}Al_xN$ films. *Journal of Vacuum Science & Technology A: Vacuum, Surfaces, and Films*, 20(2):569–571, 2002.

[7] A. E. Reiter, V. H. Derflinger, B. Hanselmann, T. Bachmann, and B. Sartory. Investigation of the properties of $Al_{1-x}Cr_xN$ coatings prepared by cathodic arc evaporation. *Surface and Coatings Technology*, 200(7):2114–2122, 2005.

[8] A. Kimura, H. Hasegawa, K. Yamada, and T. Suzuki. Effects of Al content on hardness, lattice parameter and microstructure of $Ti_{1-x}Al_xN$ films. *Surface and Coatings Technology*, 120-121:438–441, 1999.

[9] K. S. Chan, M. Y. He, and J. W. Hutchinson. Cracking and stress redistribution in ceramic layered composites. *Materials Science and Engineering: A*, 167(1-2):57–64, 1993.

[10] P. Fratzl and R. Weinkamer. Nature's hierarchical materials. *Progress in Materials Science*, 52(8):1263–1334, 2007.

[11] M. P. Rao. Laminar Ceramics That Exhibit a Threshold Strength. *Science*, 286(5437):102–105, 1999.

[12] S. Zhang, D. Sun, Y. Fu, and H. Du. Toughening of hard nanostructural thin films: A critical review. *Surface and Coatings Technology*, 198(1-3):2–8, 2005.

[13] R. Daniel, M. Meindlhumer, J. Zalesak, B. Sartory, A. Zeilinger, C. Mitterer, and J. Keckes. Fracture toughness enhancement of brittle nanostructured materials by spatial heterogeneity: A micromechanical proof for CrN/Cr and TiN/SiOx multilayers. *Materials & Design*, 104:227–234, 2016.

[14] K. Valleti, A. Jyothirmayi, M. Ramakrishna, and S. V. Joshi. Influence of substrate temperature and bias voltage on properties of chromium nitride thin films deposited by cylindrical cathodic arc deposition. *Journal of Vacuum Science & Technology A: Vacuum, Surfaces, and Films*, 29(5):051515, 2011.

[15] J. Romero, M. A. Gómez, J. Esteve, F. Montalà, L. Carreras, M. Grifol, and A. Lousa. CrAlN coatings deposited by cathodic arc evaporation at different substrate bias. *Thin Solid Films*, 515(1):113–117, 2006.

[16] M. Bartosik, M. Arndt, R. Rachbauer, C. Krywka, C. M. Koller, J. Keckes, and P. H. Mayrhofer. Cross-sectional X-ray nano-diffraction and -reflectivity analysis of multilayered AlTiN–TiSiN thin films: Correlation between residual strain and bi-layer period. *Scripta Materialia*, 107:153–156, 2015.

[17] A. Zeilinger, R. Daniel, M. Stefenelli, B. Sartory, L. Chitu, M. Burghammer, T. Schöberl, O. Kolednik, J. Keckes, and C. Mitterer. Mechanical property enhancement in laminates through control of morphology and crystal orientation. *Journal of Physics D: Applied Physics*, 48(29):295303, 2015.

[18] J. Lin, J. J. Moore, B. Mishra, M. Pinkas, X. Zhang, and W. D. Sproul. CrN/AlN superlattice coatings synthesized by pulsed closed field unbalanced magnetron sputtering with different CrN layer thicknesses. *Thin Solid Films*, 517(20):5798–5804, 2009.

[19] M. Schlögl, J. Paulitsch, J. Keckes, and P. H. Mayrhofer. Influence of AlN layers on mechanical properties and thermal stability of Cr-based nitride coatings. *Thin Solid Films*, 531:113–118, 2013.

[20] M. Schlögl, C. Kirchlechner, J. Paulitsch, J. Keckes, and P. H. Mayrhofer. Effects of structure and interfaces on fracture toughness of CrN/AlN multilayer coatings. *Scripta Materialia*, 68(12):917–920, 2013.

[21] J. Keckes, M. Bartosik, R. Daniel, C. Mitterer, G. Maier, W. Ecker, J. Vila-Comamala, C. David, S. Schoeder, and M. Burghammer. X-ray nanodiffraction reveals strain and microstructure evolution in nanocrystalline thin films. *Scripta Materialia*, 67(9):748–751, 2012.

[22] Christian Riekel, Manfred Burghammer, and Richard Davies. Progress in micro- and nano-diffraction at the ESRF ID13 beamline. *IOP Conference Series: Materials Science and Engineering*, 14:012013, 2010.

[23] A. P. Hammersley, S. O. Svensson, M. Hanfland, A. N. Fitch, and D. Hausermann. Two-dimensional detector software: From real detector to idealised image or two-theta scan. *High Pressure Research*, 14(4-6):235–248, 1996.

[24] J. Almer, U. Lienert, R. L. Peng, C. Schlauer, and M. Odén. Strain and texture analysis of coatings using high-energy x-rays. *Journal of Applied Physics*, 94(1):697–702, 2003.

[25] A. J. Wang, S. L. Shang, Y. Du, Y. Kong, L. J. Zhang, L. Chen, D. D. Zhao, and Z. K. Liu. Structural and elastic properties of cubic and hexagonal TiN and AlN from first-principles calculations. *Computational Materials Science*, 48(3):705–709, 2010.

[26] L. Vegard. Die Konstitution der Mischkristalle und die Raumfuellung der Atome. *Zeitschrift fur Physik*, 1921(5):17–26, 1921.

[27] C. Sabitzer, J. Paulitsch, S. Kolozsvári, R. Rachbauer, and P. H. Mayrhofer. Influence of bias potential and layer arrangement on structure and mechanical properties of arc evaporated Al–Cr–N coatings. *Vacuum*, 106:49–52, 2014.

[28] F. Lomello, F. Sanchette, F. Schuster, M. Tabarant, and A. Billard. Influence of bias voltage on properties of AlCrN coatings prepared by cathodic arc deposition. *Surface and Coatings Technology*, 224:77–81, 2013.

[29] A. Anders. *Cathodic Arcs*, volume 50. Springer New York, New York, NY, 2008.

[30] M. Pohler, R. Franz, J. Ramm, P. Polcik, and C. Mitterer. Cathodic arc deposition of (Al,Cr)2O3: Macroparticles and cathode surface modifications. *Surface and Coatings Technology*, 206(6):1454–1460, 2011.

[31] V. Edlmayr, M. Pohler, I. Letofsky-Papst, and C. Mitterer. Microstructure and thermal stability of corundum-type (Al0.5Cr0.5)2O3 solid solution coatings grown by cathodic arc evaporation. *Thin Solid Films*, 534:373–379, 2013.

[32] L. Zhou, D. Holec, and P. H. Mayrhofer. First-principles study of elastic properties of cubic Cr 1− x Al x N alloys. *Journal of Applied Physics*, 113(4):043511, 2013.

[33] ICDD. Card 00-035-0803.

[34] ICDD. Card 00-046-1200.

[35] ICDD. Card 01-070-2543.

[36] ICDD. Card 03-065-2899.

[37] K. J. Martinschitz, R. Daniel, C. Mitterer, and J. Keckes. Elastic constants of fibre-textured thin films determined by X-ray diffraction. *Journal of applied crystallography*, 42(Pt 3):416–428, 2009.

[38] G. Abadias. Stress and preferred orientation in nitride-based PVD coatings. *Surface and Coatings Technology*, 202(11):2223–2235, 2008.

[39] W. Ernst, J. Neidhardt, H. Willmann, B. Sartory, P. H. Mayrhofer, and C. Mitterer. Thermal decomposition routes of CrN hard coatings synthesized by reactive arc evaporation and magnetron sputtering. *Thin Solid Films*, 517(2):568–574, 2008.

[40] M. Stefenelli, J. Todt, A. Riedl, W. Ecker, T. Müller, R. Daniel, M. Burghammer, and Keckes. X-ray analysis of residual stress gradients in TiN coatings by a Laplace space approach and cross-sectional nanodiffraction: a critical comparison. *Journal of applied crystallography*, 46(Pt 5):1378–1385, 2013.

[41] Y. Sun, Y. H. Wang, and H. P. Seow. Effect of substrate material on phase evolution in reactively sputtered Cr-Al-N films. *Journal of Materials Science*, 2004(39):7369–7371.

[42] R. Daniel, K. J. Martinschitz, J. Keckes, and C. Mitterer. Texture development in polycrystalline CrN coatings: The role of growth conditions and a Cr interlayer. *Journal of Physics D: Applied Physics*, 42(7):075401, 2009.

[43] J. Lin, J. J. Moore, B. Mishra, M. Pinkas, and W. D. Sproul. Nanostructured CrN/AlN multilayer coatings synthesized by pulsed closed field unbalanced magnetron sputtering. *Surface and Coatings Technology*, 204(6-7):936–940, 2009.

[44] D. R. McKenzie and M.M.M. Bilek. Thermodynamic theory for preferred orientation in materials prepared by energetic condensation. *Thin Solid Films*, 382(1-2):280–287, 2001.

[45] S. Khan, M. Shahid, A. Mahmood, A. Shah, Ishaq Ahmed, Mazhar Mehmood, U. Aziz, Q. Raza, and M. Alam. Texture of the nanocrystalline AlN thin films and the growth conditions in DC magnetron sputtering. *Progress in Natural Science: Materials International*, 25(4):282–290, 2015.

[46] B. K. Gan, M. M. M. Bilek, D. R. McKenzie, M. B. Taylor, and D. G. McCulloch. Effect of intrinsic stress on preferred orientation in AlN thin films. *Journal of Applied Physics*, 95(4):2130–2134, 2004.

[47] N. Schalk, C. Mitterer, J. Keckes, M. Penoy, and C. Michotte. Influence of residual stresses and grain size on the spinodal decomposition of metastable Ti1−xAlxN coatings. *Surface and Coatings Technology*, 209:190–196, 2012.

[48] H. Willmann, P. H. Mayrhofer, L. Hultman, and C. Mitterer. Hardness evolution of Al–Cr–N coatings under thermal load. *Journal of Materials Research*, 23(11):2880–2885, 2008.

[49] I. Petrov, P. B. Barna, L. Hultman, and J. E. Greene. Microstructural evolution during film growth. *Journal of Vacuum Science & Technology A: Vacuum, Surfaces, and Films*, 21(5):S117–S128, 2003.

[50] R. Daniel, J. Keckes, I. Matko, M. Burghammer, and C. Mitterer. Origins of microstructure and stress gradients in nanocrystalline thin films: The role of growth parameters and self-organization. *Acta Materialia*, 61(16):6255–6266, 2013.

13

Publication II

N. Jäger, M. Meindlhumer, S. Spor, H. Hruby, J. Julin, A. Stark, F. Nahif, J. Keckes, C. Mitterer, R. Daniel

Publication II

Microstructural evolution and thermal stability of AlCr(Si)N hard coatings revealed by in-situ high-temperature high-energy grazing incidence transmission X-ray diffraction

N. Jäger[a], M. Meindlhumer[a], S. Spor[a,b], H. Hruby[b], J. Julin[c], A. Stark[d], F. Nahif[b], J. Keckes[e,f], C. Mitterer[f], R. Daniel[a]

[a]*Christian Doppler Laboratory for Advanced Synthesis of Novel Multifunctional Coatings at the Department of Materials Science, Montanuniversität Leoben, Austria*
[b]*voestalpine eifeler Vacotec GmbH, Düsseldorf, Germany*
[c]*Institute of Ion Beam Physics and Materials Research at the Helmholtz-Zentrum Dresden-Rossendorf, Dresden, Germany*
[d]*Helmholtz Zentrum Geesthacht, Centre for Materials and Coastal Research, Geesthacht, Germany*
[e]*Erich Schmid Institute for Materials Science, Austrian Academy of Sciences, Austria*
[f]*Department of Materials Science, Montanuniversität Leoben, Austria*

Abstract

An extensive understanding about the microstructural evolution and thermal stability of the metastable AlCr(Si)N coating system is of considerable importance for applications facing high temperatures, but it is also a challenging task since several superimposed processes simultaneously occur at elevated temperatures. In this work, three AlCr(Si)N coatings with 0 at.%, 2.5 at.% and 5 at.% Si were investigated by in-situ high-temperature high-energy grazing incidence transmission X-ray diffraction (HT-HE-GIT-XRD) and complementary differential scanning calorimetry and thermogravimetric analysis measurements combined with conventional ex-situ X-ray diffraction. The results revealed (i) a change in the microstructure from columnar to a fine-grained nano-composite, (ii) a reduced decomposition rate of CrN to Cr_2N, also shifted to higher onset temperatures from ∼ 1000 °C to above 1100 °C and (iii) an increase of lattice defects and micro strains resulting in a significant increase of compressive residual strain with increasing Si content. While the Si-containing coatings in the as-deposited state show a lower hardness of 28 GPa compared to AlCrN with 32 GPa, vacuum annealing at 1100 °C led to an increase in hardness to 29 GPa for the coatings containing Si and a decrease in hardness to 26 GPa for AlCrN. Furthermore, the in-situ HT-HE-GIT-XRD method allowed for simultaneously accessing temperature-dependent variations of the coating microstructure (defect density, grain size), residual strain state and phase stability up to 1100 °C. Finally, the results established a deeper understanding about the relationships between the elemental composition of the materials, the resulting microstructure including crystallographic phases and residual strain state, and the coating properties from room temperature up to 1100 °C.

Keywords: AlCrSiN, nano-composite, cathodic arc, thermal stability,

1. Introduction

Transition metal nitrides find widespread use as hard protective coatings in applications with surfaces exposed to wear. The rising demand on wear-protective hard coatings for severe applications has stimulated the development of advanced coatings with sophisticated microstructural and compositional design [1–5]. Besides substantial requirements on mechanical properties, also thermal stability and oxidation resistance of such materials play a key role in modern high-temperature applications like dry cutting or high speed cutting. The temperatures of cutting tools operating under harsh conditions may exceed 1000 °C [6], especially near to the cutting edge.

Nowadays, ternary metal nitride coatings such as AlCrN are frequently used in industry [7, 8] due to their high hardness, wear and oxidation resistance [9–11]. The AlCrN system can be synthesized with face-centered cubic structure up to an Al content of 75 at.% on the metal sublattice [12]. By exceeding this critical solubility limit, an additional phase with hexagonal crystallographic structure forms, becoming dominant at higher Al contents [13]. Since cubic (c-)AlCrN is a thermodynami-

cally metastable solid solution, hexagonal (h-)Al(Cr)N forms at elevated temperatures and the CrN-enriched matrix decomposes in a two-step reaction into Cr_2N and finally Cr [14]. Especially the decomposition into Cr_2N is highly undesirable, as the associated release of N_2 yields a porous structure and deteriorates mechanical properties.

One approach to further improve the performance of hard coatings is to enhance the material's properties by alloying. A promising candidate as alloying element in AlCrN coatings is Si, as shown by several successful attempts enhancing the mechanical properties, the behaviour at high-temperatures and the tribological performance of AlCrN by adding Si [15–17]. Since the solubility limit of Si in AlCrN is low [18], Si tends to segregate along grain boundaries where it forms an additional amorphous (a-)Si_xN_y phase [19–21]. A typical MeN/a-Si_xN_y (Me = Al/Cr) nano-composite structure is formed [22, 23], composed of crystallites embedded in an amorphous tissue, which results in a material with completely new properties. Benefits may arise from the nano-composite hardening effect, where dislocation movement is hindered at grain boundaries and at the interface with the a-Si_xN_y tissue [24], or by suppressed inter-

granular diffusion and thus restricted propagation of oxidation [20].

While AlCr(Si)N coating systems in various compositions have been investigated in terms of microstructure [15, 18], mechanical [17] and tribological [25] properties or cutting performance [23, 26], a detailed study of the thermal stability is still missing. In this work, the influence of Si content on the thermal stability of three AlCr(Si)N coatings with a fixed Al/Cr atomic ratio of 70/30 and 0 at.%, 2.5 at.% and 5 at.% Si, respectively, is studied. The recently developed approach [27, 28] using in-situ high-temperature high-energy grazing-incidence transmission X-ray diffraction (HT-HE-GIT-XRD) at the German Synchrotron (DESY) at PETRA III was used to analyse the coatings. This method relies on a cross-sectional approach investigating the coating-substrate system in transmission geometry, providing simultaneously access to temperature-dependent variations of the coating microstructure (defect density, grain size), residual strain state, thermal expansion coefficients of coating and substrate material and phase stability. Complementary differential scanning calorimetry (DSC) and thermogravimetric analysis (TGA) measurements combined with conventional ex-situ X-ray diffraction were performed on powdered coatings to determine structural changes occurring at elevated temperatures up to 1450 °C.

The results reveal a fundamental change in microstructure and thus material's properties when Si is added to the AlCrN system. A considerably grain refinement is observed for the coatings containing Si, originating from the formation of a nano-composite structure. Additionally, Si reduces the solubility limit of AlN in CrN, resulting in a purely cubic-phased AlCrN coating and a dual-phase (hexagonal and cubic) microstructure of the AlCrSiN coatings. The in-situ HT-HE-GIT-XRD measurements reveal a shift of the decomposition (CrN into Cr_2N and N_2) to higher temperatures from 1050 °C to slightly below 1100 °C for AlCrN and $AlCrSi_{2.5}N$, respectively, and a totally suppressed Cr_2N formation for $AlCrSi_5N$ up to the maximum applied temperature of 1100 °C. Furthermore, the development of defect density, grain size and residual strains as a function of temperature is evaluated. Complementary DSC and TG measurements confirm this positive influence of Si, demonstrated by a retarded onset of Cr_2N formation from 950 °C in the case of Si-free AlCrN to 1080 °C with increasing Si content. Above 1200 °C, the N_2 aggravates, which results in the formation of pure Cr and Cr_3Si in the case of the Si containing coatings. The in-situ HT-HE-GIT-XRD approach and complementary DSC/TG analysis of the investigated AlCr(Si)N coating-systems reveal the influence of Si on microstructure, phase composition and thermal stability and allow for a comprehensive understanding of the underlying structure-stress-property relations.

2. Experimental methods

2.1. Film deposition

For this study three AlCr(Si)N coatings with varying Si-content and a fixed Al/Cr atomic ratio of 70/30 were deposited by cathodic arc evaporation using an industrial-sized coating system (alpha400P, voestalpine eifeler Vacotec) equipped with sets of six $Al_{70}Cr_{30}$, $Al_{66.5}Cr_{28.5}Si_5$ and $Al_{63}Cr_{27}Si_{10}$ cathodes, respectively. The coatings were grown on mirror-polished cemented carbide substrates (WC, 6 wt.% Co) and on mild steel foil. Prior to deposition, the substrates were plasma-etched to remove all contaminants and to activate the surface for better adhesion. The substrate temperature of 480 °C, the arc current on each cathode of 100 A and the N_2 pressure of 4 Pa were kept constant during deposition. A substrate bias voltage of −100 V was applied and onefold planetary substrate rotation with 2 min^{-1} was used.

2.2. Film characterisation

Fracture cross-sections of the coatings were investigated in terms of coating thickness and morphology using a Zeiss Leo1525 scanning electron microscope (SEM). The elemental composition of the coatings was measured by Elastic Recoil Detection Analysis (ERDA) in an area of approximately 1.5 mm × 1.5 mm per sample using a 43 MeV $^{35}Cl^{7+}$ ion beam. The angle between the sample normal and the incoming beam was 75°, the scattering angle was 31° and the recoiling ions were detected using a Bragg Ionization Chamber.

DSC and TG measurements of the coatings were performed using a Setaram Setsys Evo 2400 system. To obtain a sufficient DSC signal from the coatings without an influence of the substrate material, the steel foil was removed chemically in 10 % nitric acid. After filtering and washing with ethanol, the remaining coating material was ground in an agate mortar to obtain a fine powder. At first, 20 mg of each powdered sample was heated in Ar atmosphere up to 1450 °C using a heating rate of 20 K min^{-1} and cooled down at a cooling rate of 50 K min^{-1} after an isothermal holding time of 30 min. Each run was performed two times under the same conditions and the second run served as a baseline. Additionally, further powder samples (20 mg each) were annealed up to 520 °C, 850 °C, 950 °C, 1000 °C, 1080 °C, 1200 °C, 1280 °C and 1360 °C, respectively. All annealed powders were investigated using a Bruker D8 Advance diffractometer equipped with an energy-dispersive Sol-X detector and applying Cu-Kα radiation (8.04 keV). The comparison of XRD data of the samples annealed at various temperatures with the DSC and TG measurements allowed for a better understanding of the different partially overlapping reactions during annealing.

A detailed in-situ analysis of microstructure and strain state as a function of temperature was performed at the German Electron Synchrotron (DESY) at PETRA III, beamline P07B. An X-ray energy of 87.1 keV and a pencil-like shaped beam with a size of 400 μm × 100 μm allowed for measuring the entire coating-substrate system in transmission geometry, using rectangular blocked cemented carbide samples with a size of 10 mm × 5 mm × 5 mm and a coating thickness > 11 μm. The annealing was performed in vacuum with a total pressure of 2 Pa to avoid oxidation during heating, using a dilatometer Bähr DIL 805. The samples were heated up to 1100 °C at a heating rate of 1 K s^{-1} and cooled down to room temperature (RT) by an Ar flow with a cooling rate of 1 K s^{-1} after a holding

segment of 300 s at maximum temperature. The actual temperature during the experiment was recorded using a thermocouple brazed to the sample surface. A two-dimensional Perkin-Elmer detector with a pixel size of 200 μm^2, positioned at a distance of 1950 mm behind the samples, collected Debye-Scherrer diffraction frames at each temperature step. The detector was calibrated using LaB$_6$-powder and the software package Fit2D [29]. The evaluation of the measurements of the coatings was performed using a pyFAI software package [30]. For more information about the method and a detailed description of the data evaluation see [28].

Hardness and elastic modulus of the coatings were determined by nanoindentation using an ultra-micro indentation system (UMIS, Fischer-Cripps Laboratories) equipped with a Berkovich diamond tip. To get a sufficient surface quality for the indentation experiments, the samples were locally mechanically polished. The load-displacement curves were recorded under thermal equilibrium to avoid the effect of thermal drift. The indentations were performed in the load controlled mode in the range from 10 mN to 30 mN and the average values were evaluated according to the Oliver and Pharr method [31]

The coated samples used for nanoindentation measurements and as fracture cross-sections of the annealed state were annealed at 1100 °C for 30 min in an HTM Reetz vacuum furnace.

3. Results

3.1. Elemental composition

The elemental composition of the coatings obtained by ERDA is presented in Table 1. The measurements reveal nearly stoichiometric nitrides and a slight loss of Al during deposition compared to the initial cathode composition ($Al/Cr = 2.3$) due to preferred gas scattering of the lighter Al atoms in the plasma discharge during deposition [15]. The Si content of the coatings corresponds to the composition of the particular cathodes. The oxygen contamination of all coatings is ≤ 0.4 at.%. For simplicity, the coatings are denoted as AlCrN, AlCrSi$_{2.5}$N and AlCrSi$_5$N throughout the paper, corresponding to the used Al$_{70}$Cr$_{30}$, Al$_{66.5}$Cr$_{28.5}$Si$_5$ and Al$_{63}$Cr$_{27}$Si$_{10}$ cathodes, respectively.

Table 1: Elemental composition of the coatings obtained by ERDA.

Cathode composition	Coating composition [at. %]				
	Al	Cr	Si	N	Al/Cr
Al$_{70}$Cr$_{30}$	32.6	16.0	0	51.0	2.0
Al$_{66.5}$Cr$_{28.5}$Si$_5$	32.6	14.0	2.6	50.6	2.3
Al$_{63}$Cr$_{27}$Si$_{10}$	30.8	13.7	4.7	50.5	2.2

3.2. Coating morphology and microstructure

SEM micrographs of fracture cross-sections of the coatings in the as-deposited state of the samples and after vacuum annealing at 1100 °C for 30 min are shown in Figure 1. The

coating thickness is 11 μm, 11.8 μm and 12.8 μm for AlCrN, AlCrSi$_{2.5}$N and AlCrSi$_5$N, respectively, revealing an increasing deposition rate with increasing Si content in the cathodes. While the AlCrN coating without Si (Figure 1a) exhibits coarse columnar grains, the morphology transforms towards a more glassy and featureless structure with increasing Si content (Figure 1b,c), which is an indication for the formation of a fine-grained nano-composite structure [17, 22]. After vacuum annealing at 1100 °C for 30 min, the coating microstructure of AlCrN in Figure 1d appears to be slightly coarser grained, while it remains glassy and featureless for the Si-containing coatings in Figure 1e and f.
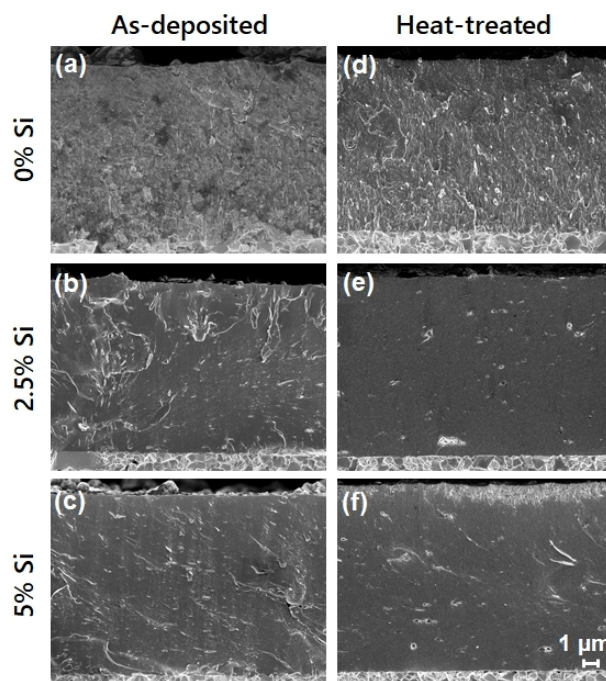

Figure 1: SEM micrographs of fracture cross-sections of (a and d) AlCrN, (b and e) AlCrSi$_{2.5}$N and (c and f) AlCrSi$_5$N on cemented carbide substrates in the (a-c) as-deposited state and (d-f) after annealing at 1100 °C.

3.3. Thermal stability

3.3.1. DSC and TG measurements of powdered samples

Figure 2 shows the heat flow and the corresponding mass change of the AlCr(Si)N coatings as a function of annealing temperature. The variations in the heat-flow curves indicate that various reactions occur during annealing, corresponding to diffusion-driven structural changes, reflected also by changes of the sample mass. The superimposed signal in relatively small temperature ranges suggests a variety of structural changes, which occur almost simultaneously. In order to better understand the changes, XRD analysis of powders was performed after various annealing steps at temperatures indicated by vertical lines in Figure 2. The obtained X-ray diffractograms are presented in Figure 3.
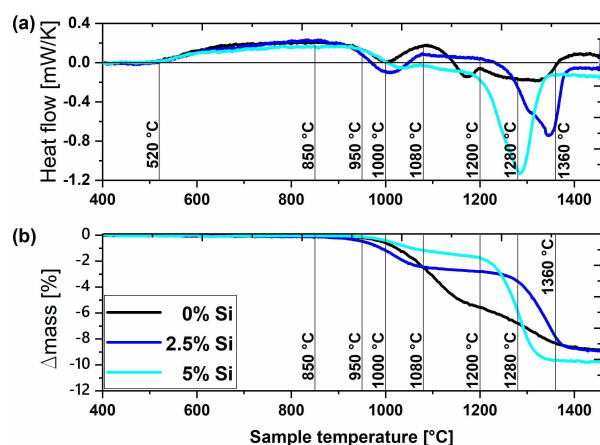
Figure 2: (a) DSC and (b) TG curves of AlCrN, AlCrSi$_{2.5}$N and AlCrSi$_5$N in Ar atmosphere. Annealing temperatures for ex-situ XRD measurements of powders are inserted.

The formation of a nano-composite microstructure, composed of AlCrN crystallites embedded in an a-Si$_x$N$_y$ matrix, also results in a substantial grain refinement. This is reflected by broad peaks with low intensity in the X-ray diffractograms of the Si-containing coatings at RT in Figure 3. Furthermore, the addition of Si to AlCrN shifts the transition between cubic and hexagonal crystal structure to lower Al-contents (Al/Cr ratio is kept constant for all coatings) and thus an additional hexagonal phase forms for AlCrSi$_{2.5}$N and AlCrSi$_5$N already during deposition.

During annealing, the first exothermic reaction visible in Figure 2 starts 40 °C above deposition temperature (480 °C) at 520 °C for all coatings and is related to recovery processes of deposition induced lattice defects [32]. This is also reflected by decreasing FWHM with increasing annealing temperatures in Figure 3). Since the cubic AlCrN solid solution is a thermodynamically metastable phase, it decomposes into an Al-rich h-Al(Cr)N and a Cr-rich c-Cr(Al)N phase at elevated temperatures [14]. Nucleation and growth of the h-AlN precipitates starts at grain boundaries [14] and are associated with heat formation reflected by an exothermic contribution to the DSC signal (Figure 2) with a peak maximum at 850 °C. At this temperature, first small fractions of h-AlN precipitates are detected for the AlCrN coating without Si (Figure 3a), and the corresponding peak intensity continuously increases with rising annealing temperature. The same trend is observed for the Si-containing coatings, where, however, the formation of the h-AlN precipitates occurs already at lower annealing temperatures.

At temperatures of about 900 °C, the decomposition of Cr-rich Cr(Al)N regions into Cr$_2$N and pure nitrogen releasing the coatings results in a decreasing sample mass (Figure 2b) and is accompanied by an endothermic contribution to the DSC signal (Figure 2a). The peak maximum of this endothermic reaction is at 1000 °C for the AlCrN coating without Si and shifted to slightly higher temperatures with increasing Si content (Figure 2a). An overall mass loss of 6 %, 3 % and 2 % at 1200 °C for

AlCrN, AlCrSi$_{2.5}$N and AlCrSi$_5$N, respectively, indicates that the amount of formed Cr$_2$N decreases with increasing Si content. The retarded decomposition of the Si-containing coatings is also reflected in the X-ray diffractograms in Figure 3. While the first Cr$_2$N diffraction peaks at 2θ angles of 42.6° and 43.4° can be seen for the powders annealed at 950 °C for AlCrN and AlCrSi$_{2.5}$N, they appear at 1000 °C for AlCrSi$_5$N. Additionally, the intensity of the Cr$_2$N signal is much lower for AlCrSi$_5$N compared to the AlCrSiN coatings with 2.5 at.% and without Si.

A changing slope of the mass signal of the AlCrN coating without Si at about 1140 °C (Figure 2b) marks the onset of the decomposition of Cr$_2$N into Cr and N$_2$, which is accompanied by an exothermic contribution to the DSC signal (Figure 2a). While decomposition of Cr$_2$N is observed at 1250 °C in the case of AlCrSi$_{2.5}$N, it decomposes already at 1200 °C for AlCrSi$_5$N. Simultaneously with the kink in the mass signals, a considerably strong (compared to AlCrN) endothermic peak appears in the DSC scans. The substantial mass loss and the large endothermic reaction of the Si containing coatings originates from the decomposition of Si$_x$N$_y$, which significantly contributes to the heat-flow. Although pure Si$_3$N$_4$ is thermally stable up to 1900 °C, it reacts in the presence of Cr forming Cr$_3$Si at temperatures considerably below 1300 °C [33].

The decomposition of Cr$_2$N is also indicated by XRD, where a Cr peak ($2\theta \sim 44.1°$) emanates at the expense of the Cr$_2$N peaks (Figure 3). The first evidence for Cr can be seen at 1200 °C for the AlCrN coating and at 1280 °C for AlCrSi$_5$N and AlCrSi$_{2.5}$N, in each case at temperatures slightly above the kink in the mass signal of the TG measurements. Simultaneously with the rising Cr and diminishing Cr$_2$N reflections an additional peak at 39.5° develops with increasing annealing temperature, which stems from the Cr$_3$Si phase formed in both Si containing coatings. Since there is more Si disposed in the AlCrSi$_5$N coating, the amount of formed Cr$_3$Si phase is higher than that for AlCrSi$_{2.5}$N, resulting in a higher intensity of the Cr$_3$Si peak.

The constant sample mass and a constant heat flow at temperatures above 1400 °C indicate fully completed structural changes. The X-ray diffractograms of the coating powders measured after the DSC experiments (orange lines in Figure 3 at 1450 °C) reveal exclusively h-Al(Cr)N and Cr, plus the Cr$_3$Si phase in the case of the Si-containing coatings. High peak intensities and small FWHM indicate a microstructure with less lattice defects and significant coarser grain structure after annealing [14].

3.3.2. In-situ high-temperature high-energy grazing-incidence transmission X-ray diffraction

DSC and TG measurements typically provide information about exothermic and endothermic reactions and decomposition processes of materials at dedicated temperatures during annealing. The methods are commonly limited to the use of powdered samples to get a sufficient signal from the coating when analysing coated samples. Furthermore, complementary investigations such as ex-situ XRD are often necessary to obtain a deeper understanding of the ongoing processes and structural
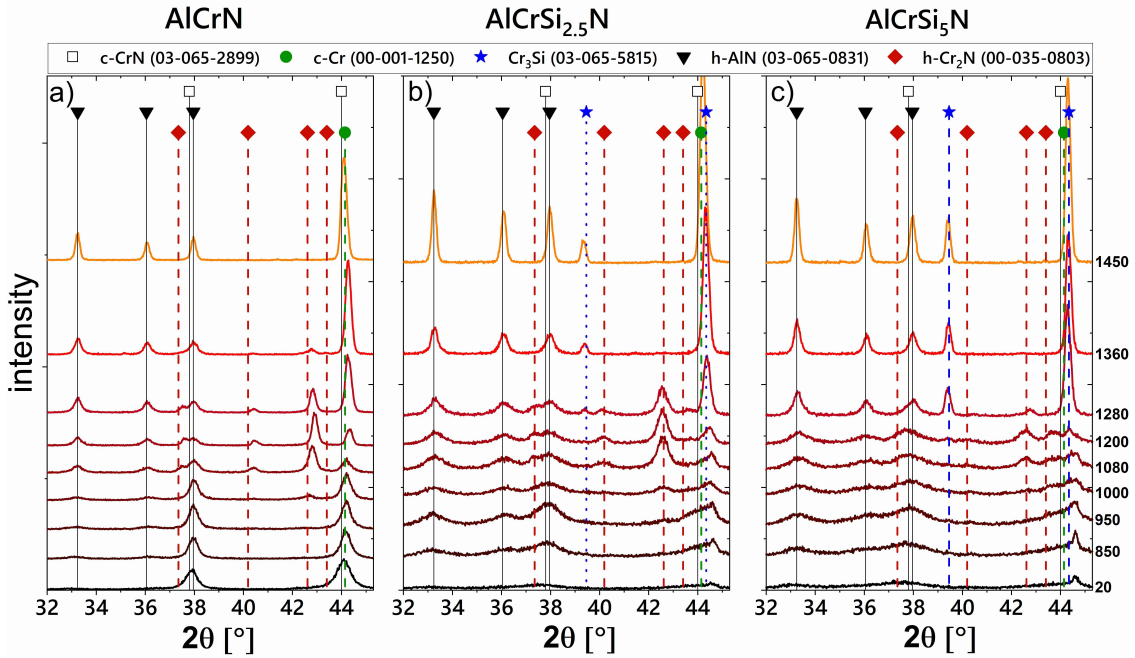
4

Figure 3: X-ray diffractograms of (a) AlCrN, (b) AlCrSi$_{2.5}$N and (c) AlCrSi$_5$N coatings in the as-deposited state and after annealing at various temperatures in Ar atmosphere. A zoom-in from 42° to 45.5° is shown in Supplementary Figure A.1 to show more details.

changes during annealing. On the contrary, in-situ HT-HE-GIT-XRD using a 400 µm × 100 µm X-ray beam in transmission geometry facilitates a structural analysis of coated samples with the possibility to separate the signals from coating and substrate. The main advantage of this method arises from the capability to analyse the whole coating-substrate system in contrast to the investigation of powdered samples. For the latter case, the coatings are strongly affected by the sample preparation, as residual stress relaxes during powdering and grinding. The impact of stress release due to sample preparation will be discussed in more details in section 4. Furthermore, in-situ HT-HE-GIT-XRD allows for determination of numerous independent material characteristics of coating and substrate and their variation as a function of annealing temperature such as phase composition, FWHM, texture, intrinsic and thermal residual stress components and thermal expansion coefficients.

The phase evolution of the coatings during annealing is shown in Figure 4. Besides reflections emanating from the coating, corresponding to h-Al(Cr)N, c-Cr(Al)N and h-Cr$_2$N, also WC and Co reflections stemming from the substrate are visible. A slight peak shift to lower angles with increasing temperature and back to higher angles with decreasing temperature corresponds to the changing lattice parameter attributed to the thermal expansion. Especially the position of the Co peak strongly varies with the annealing temperature due to the metallic nature of Co and its greater thermal expansion coefficient with respect to the other phases.

The diffraction patterns in the as-deposited state of all coatings on the cemented carbide substrates (inserted in Figure 4) match with those of the powdered samples in Figure 3. They

only differ concerning the WC and Co substrate peaks at 3.25° and 3.95°, respectively, present only in the measured spectra of coated samples in Figure 4. While the AlCrN coating consists of exclusively cubic phase in the as-deposited state, the Si-containing coatings exhibit a dual-phase crystallographic structure comprising of c-Cr(Al)N and h-Al(Cr)N. Furthermore, a much finer grain size of the Si containing coatings is reflected by very broad peaks (also resulting in a brighter appearance of the phase plots in Figure 4b and c, while maintaining the same colour-scaling compared to Figure 4a). The texture development of the coatings with the annealing temperature is shown in Figure A.2. While the single-phase cubic crystal structure of AlCrN exhibits a (111) fibre texture, the cubic crystallites of the dual-phase Si-containing coatings are predominantly (110)-oriented, and the hexagonal crystallites exhibit a (110) fibre texture too. The crystallites of the h-Al(Cr)N formed during annealing of AlCrN exhibit a less pronounced texture.

The Si-free c-AlCrN coating starts to decompose into h-Al(Cr)N and c-Cr(Al)N at about 750 °C. The further decomposition of the Cr-enriched c-Cr(Al)N into Cr$_2$N is evidenced by additional reflexes at 3.6° and 3.8°. While the first Cr$_2$N peaks arise at 1050 °C for AlCrN, Cr$_2$N formation is retarded to 1100 °C for AlCrSi$_{2.5}$N. Finally, the formation of Cr$_2$N is completely suppressed within the measured temperature range with a maximum of 1100 °C for the AlCrSi$_5$N coating. Interestingly, despite the multiple phase decomposition, the orientation of the cubic and hexagonal crystallites has not changed during annealing (Figure A.2).

Since the FWHM of X-ray diffraction peaks is generally sensitive to the presence of lattice defects, size of coherently
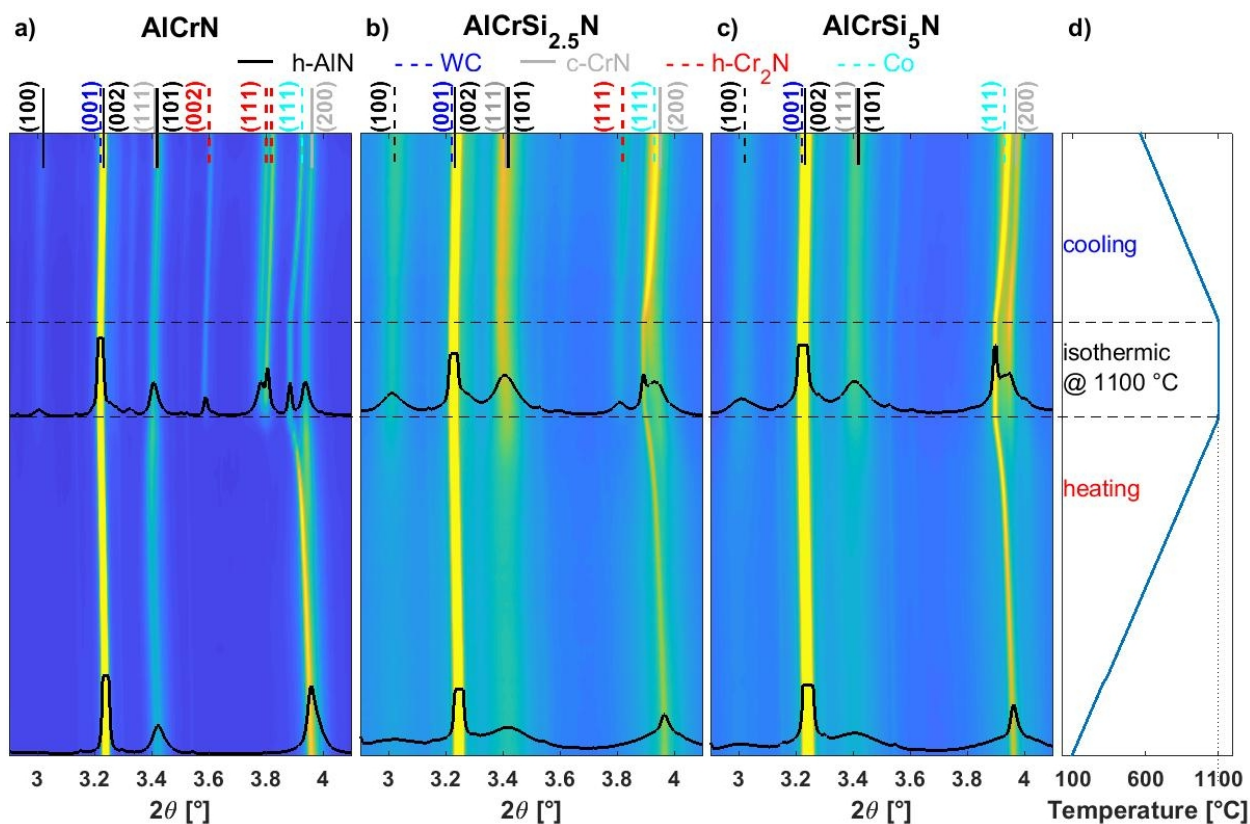
5

Figure 4: Diffraction intensities I(θ,T) along the annealing temperature showing the development of the crystallographic structure of the (a) AlCrN, (b) AlCrSi$_{2.5}$N and (c) AlCrSi$_5$N coating, together with (d) the applied temperature including heating from RT to 1100 °C with 10 K min^{-1}, isothermal holding at 1100 °C for 5 min and cooling back to RT with 10 K min^{-1}. Diffractograms of each coating at RT and at 1100 °C are inserted for ancillary visualization.
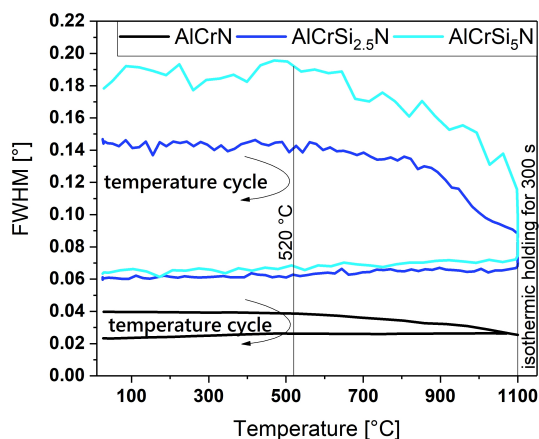

Figure 5: Development of the FWHM as a function of annealing temperature. The values were assessed from the representative CrN(111) peak having the highest intensity without an overlap with any reflection from the substrate.

diffracting domains and micro-strains of second and third order, the FWHM values plotted in Figure 5 thus reflect the temperature-dependent variations of structural defect densities and grain sizes of the corresponding coatings. The FWHM were evaluated by fitting the CrN (111) diffraction peaks using the Pseudo-Voigt function. The higher scattering in the FWHM of the Si-containing coatings (Figure 5) originated from the fitting of the generally broader diffraction peaks with respect to AlCrN and a partial overlap with the Co-peaks stemming from the substrate (Figure 4). Due to the typical columnar growth of crystallites in physical vapour deposition (PVD) coatings in the normal direction with respect to the substrate surface, the evaluation of the Debye-Scherrer rings is restricted to a corresponding range of $\delta = \pm 10°$ around the out-of-plane diffraction vector (for better understanding see Figure 1 in [1]). Thus, only crystal planes oriented approximately parallel to the surface contribute to the evaluated signal, which allows concluding particularly about the elongation of the grains in growth direction.

The analysis of the FWHM of the dominant reflections of the coatings in Figure 5 reveals its increase with an increasing Si. The encapsulation of the grains by the Si$_x$N$_y$ tissue limited the grain growth resulting in a fine-grained nano-composite structure, compared to the larger grains developing during the columnar grain growth of AlCrN without Si (also seen in Figure 1). Almost no variation of the FWHM up to tem-

6

peratures slightly above the deposition temperature at 520 °C further reflects stability of the microstructure of all coatings in terms of process-induced lattice defects and grain size in this temperature range. Above this temperature, recovery processes and possible grain growth are observed as indicated by continuously decreasing FWHM. Defect annihilation, grain growth and reduction of micro-strains during annealing occur intensified with increasing Si content in the coatings, reflected by a higher difference of the FWHM between the as-deposited state and after annealing with respect to the Si free coating (Figure 5). The FWHM is reduced by 50 %, 57 % and 67 % for AlCrN, AlCrSi$_{2.5}$N and AlCrSi$_5$N, respectively. This may most probably be due to a higher driving force for structural changes because of the smaller grain size and a higher defect density of the initial state of the nano-composite structure.

For the AlCrN coating, the FWHM does not change during the isothermal holding segment at the maximum temperature of 1100 °C. This documents no further ongoing defect annihilation or grain growth occurring at that temperature. On the contrary, both Si-containing coatings exhibit decreasing FWHM during the isothermal holding segment, which indicates a sufficiently high driving force for ongoing recovery processes and possible grain growth of the crystallites of the nano-composite structure. Lower thermal stability of the microstructure in terms of defect annihilation is observed for AlCrSi$_5$N compared to AlCrSi$_{2.5}$N. The FWHM of all coatings remains constant between 1100 °C and RT, indicating no further structural changes during cooling (Figure 5).
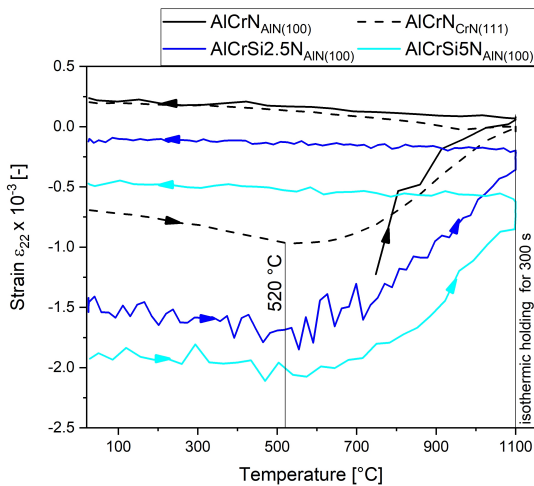

Figure 6: Development of the in-plane residual strains along annealing temperature. The strains were evaluated from the h-AlN (100) peak of the particular coatings. Since there is no hexagonal phase for the AlCrN coating without Si up to 750 °C, strains evaluated from the c-CrN (111) peak are presented additionally. Note, that the Si-containing coatings obtain more scattering, which can again be referred to the broader diffraction peaks (Figure 4).

The evolution of in-plane elastic residual strain as a function of temperature is shown in Figure 6. The strain for all coatings is obtained by evaluating the ellipticity of the corresponding h-AlN (100) Debye-Scherrer rings, which were chosen as

they are less overlapping with a diffraction signal stemming either from the cubic AlCrN phase or the substrate. Since AlCrN is composed exclusively of the cubic phase up to 750 °C, the c-CrN (111) ring is additionally evaluated to get information about strain variation for the whole temperature range. (A detailed description of the methodology used for the strain evaluation including the equations used for the calculations is given in [28].)

The evaluation of strains via the ellipticity of the Debye-Scherrer rings provides information about the overall residual strain state comprising of two dominant components: intrinsic and thermal strain. Extrinsic strains stemming from structural misfits between substrate and coating, precipitations and plastic or creep deformation are neglected here, since they play only a minor role compared to the other two components [34].

All coatings exhibit compressive residual strain in the as-deposited state, reflecting formation of a high number of deposition induced lattice defects. The compressive strain increases with increasing Si content from -0.7×10^{-3} for AlCrN to -1.5×10^{-3} for AlCrSi$_{2.5}$N and -2.0×10^{-3} for AlCrSi$_5$N.

With the supplemental information about the TECs of substrate and coating materials, a statement whether the state of the thermal strain component is tensile or compressive is determined. The TECs, determined from the unstrained lattice parameters of the particular phase (for more detail see [28]), are 5.5×10^{-6} K^{-1} for the tungsten carbide, and 11.1×10^{-6} K^{-1} and 6.3×10^{-6} K^{-1} for the cubic and the hexagonal phase of the coatings, respectively. Because of the smaller TEC of the substrate compared to the coatings, a tensile thermal strain contribution develops for all coatings when the samples are cooled down after deposition to room temperature.

A reduction of the tensile thermal strain contribution leads to an increase of the overall compressive residual strain in the temperature range between RT and 520 °C, as shown in Figure 6. At 520 °C, which is slightly higher than the deposition temperature, lattice defects start to anneal out as indicated by the variation of the FWHM in Figure 5. This results in a reduction of the intrinsic (compressive) strain component leading to a continuous decrease of the overall compressive residual strain [14]. At the maximum temperature of 1100 °C, compressive strain is reduced to -0.3×10^{-3} and -0.8×10^{-3} for AlCrSi$_{2.5}$N and AlCrSi$_5$N, respectively, and completely relaxes for Si-free AlCrN.

The strain relaxation of AlCrSi$_{2.5}$N and AlCrSi$_5$N continues during the isothermal holding segment at 1100 °C, while the strain state of AlCrN remains unchanged (Figure 6). This can be correlated with the ongoing recovery processes of the Si-containing coatings described above and indicated in Figure 5. As a consequence of the decreased intrinsic (compressive) strain component associated with defect annihilation, the residual strain state after the annealing is determined as -0.2×10^{-3} and -0.5×10^{-3} for AlCrSi$_{2.5}$N and AlCrSi$_5$N, respectively, and becomes even tensile for AlCrN with $+0.3 \times 10^{-3}$.

3.4. Hardness and elastic modulus

The hardness and elastic modulus values of the coatings as a function of Si content in the as-deposited state and after vac-

uum annealing at 1100 °C for 30 min are presented in Figure 7. In the as-deposited state, the AlCrN coating exhibits the highest hardness of 32 GPa. The addition of Si into AlCrN is accompanied by a reduction of hardness to about 28 GPa. The elastic modulus follows a similar trend and decreases from 423 GPa for AlCrN to 345 GPa and 333 GPa for $AlCrSi_{2.5}N$ and $AlCrSi_5N$, respectively. These findings will be discussed in more details in section 4.

The mechanical properties change significantly after vacuum annealing reflecting the structural changes of the coatings. While annealing results in a drop in hardness down to 26 GPa for AlCrN, a slight increase above 29 GPa occurs for both Si containing coatings. The elastic modulus of AlCrN also decreases after annealing to 423 GPa, whereas $AlCrSi_{2.5}N$ and $AlCrSi_5N$ obtain an increase up to ~ 360 GPa.
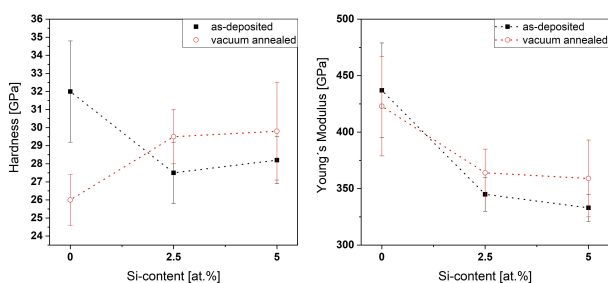

Figure 7: Development of (a) hardness and (b) elastic modulus of the AlCr(Si)N coatings as a function of Si content in the as-deposited state and after vacuum annealing at 1100 °C for 30 min.

4. Discussion

The thermal stability of a material is generally related to changes of its properties at elevated temperatures. In the case of protective hard coatings, the property variations are related to changes in microstructure given by recovery processes, phase transformations, etc. Coatings synthesised by PVD techniques generally grow under conditions far from the thermodynamic equilibrium. The apparent kinetic limitations as a result of rapid cooling at the atomic scale during deposition allow for formation of phases in metastable states and coatings with unique properties, which are otherwise not accessible in their bulk material counterparts. The metastable nature of such materials, however, often limits their application at elevated temperatures, as microstructural changes typically deteriorate their mechanical properties. Since the properties of ceramic hard coatings are mainly governed by their microstructure, a comprehensive understanding of their phase composition, defect density and residual stress state as a function of temperature is required. To analyse the thermal stability of the AlCr(Si)N coatings and its underlying mechanisms (defect recovery, recrystallisation, phase transformations, decomposition, strain relaxation, etc.), a newly developed in-situ HT-HE-GIT-XRD method combined with conventional DSC, TGA and XRD was used for investigation of three AlCr(Si)N coatings with 0 at.%, 2.5 at.% and 5 at.% Si and a fixed Al/Cr atomic ratio of 70/30. While

DSC/TG measurements together with the X-ray diffractograms of coating powders annealed at specific temperatures give detailed information about chemical reactions, phase transitions and decomposition up to a temperature of 1450 °C, the in-situ HT-HE-GIT-XRD method allows to study the whole coating-substrate system (instead of a powdered coating) and to simultaneously access the phase composition, defect density and grain size and residual strain state as a function of temperature up to 1100 °C. By combination of the advanced in-situ HT-HE-GIT-XRD method with conventional DSC/TG, the influence of the residual stress state on the thermal stabilty of the coatings became accessible, as discussed later in this section.

An effect of Si on the coating microstructure and its properties has been demonstrated for the TiN [35], AlTiN [36], CrN [37] and AlCrN [17] coating systems. Already at small Si contents, a complete change of the coating's microstructure from a columnar grain morphology to a nano-composite structure has been observed. In AlCrSiN, the Si-N bonds are preferred compared to Cr-Si or Al-Si bonds, resulting in a low solubility of Si in AlCrN crystallites and a lower free energy of separated phases in comparison to AlCrSiN compounds [15, 18]. Due to the near-complete immiscibility of MeN_x metal nitride and the Si_xN_y phase, the nano-composite structure forms as a result of spinodal decomposition, comprising of MeN crystallites in an a-Si_xN_y matrix [38–40]. To assure the formation of the nano-composite structure during deposition, a sufficiently high activity of nitrogen and a sufficiently high temperature to allow diffusion during film growth is necessary. The nitrogen pressure of 4 Pa and the deposition temperature of 480 °C meet these conditions stated in [35]. Hence, the formation of a nano-composite microstructure is observed for the AlCrSiN coatings studied in this work, accompanied by a strong decrease in crystallite size, as indicated by large FWHM in Figure 3, Figure 4 and Figure 5, and also corroborated by the glassy and featureless appearance of the fracture cross-sections in Figure 1.

Although theoretical predictions report a critical AlN content of ~ 75 at.% [41] for the formation of the cubic crystal structure, AlCrN coatings composed exclusively of cubic phase were experimentally synthesized by PVD techniques only up to a maximum AlN fraction of 71 at.% [12]. Since the amount of AlN of the coatings analysed in this work is relatively close to this critical AlN content (in the range of 61 at.% to 65 at.%, see Table 1), only the coating without supplemental Si is stabilized in the purely cubic modification (Figure 3 and Figure 4). $AlCrSi_{2.5}N$ and $AlCrSi_5N$ exhibit a dual-phase hexagonal and cubic crystal structure with a similar content of hexagonal phase for both coatings. Since the Al/Cr ratio is constant for all investigated coatings, the formation of the hexagonal phase can be related to the addition of Si with consequential changes in the microstructure (grain size, defect density) and residual stress state. Moreover, former studies have revealed that, besides elemental composition, also compressive stress [42], vacancies [43] and the Al distribution on the metal sublattice [44] affect the formation of a hexagonal phase in the AlCrN or AlTiN systems. Recently, Hans et al. [45] have shown that also surface energy and therefore the crystallite size has a major influence on the phase formation of metastable materials. They calculated stability ranges

8

for the cubic and hexagonal phases in AlTiN as a function of crystallite size and found that the hexagonal phase becomes favoured for small grain sizes. These findings may also explain the destabilisation of the cubic phase in AlCrN when adding Si, as the encapsulation of the AlCr(Si)N crystallites by the amorphous Si_xN_y tissue results in a considerably grain refinement (Figure 5) with a subsequent increase of the surface energy. If this contribution to the total energy becomes dominant, a stabilisation of the hexagonal phase may be expected. Furthermore, Si affects the character of the chemical bondings in the AlCrN system. Contrary to CrN, where the metallic bonding character dominates, the Si-N bonds have, similarly to Al-N, a strong covalent bonding character. The consequent changes in electronic structure when adding Si to AlCrN go along with the structural transformation from cubic to hexagonal [46].

The incorporation of Si atoms into the AlCrSiN matrix also results in a larger defect density and greater stress of second order with an increasing Si content, indicated by larger FWHM in Figure 5 and higher compressive residual strain in Figure 6. Although a larger number of defects leads to a higher driving force for recovery and thus decreased thermal stability of defects [47], recovery processes for all coatings start at the same temperature of 520 °C, i.e. 40 °C above deposition temperature. The first phase transformation taking place at elevated temperatures is the decomposition of the metastable c-AlCrN phase into h-Al(Cr)N and c-Cr(Al)N. It occurs to a similar extent for all three coatings, with a maximum exothermic contribution to the DSC signal at ~ 850 °C. Since the formation of the hexagonal phase is accompanied by a volume expansion of 26 % [44], the metastable cubic phase can be stabilized by a compressive residual stress state [48]. Once the substrate is removed and a free-standing coating is received (e.g. powdered coating), the compressive residual stresses in the coatings relax and only the intrinsic stresses of second and third order are left. Therefore, the measured properties of a coating on a substrate differ from the measured properties of a free-standing coating, e.g. observed for fracture toughness in [49] or phase stability in [50]. The effect of the state of the coating (coated substrate versus powder) and its resulting residual stress state on the measured material's properties is reflected by the decomposition of CrN into Cr_2N at elevated temperatures. The onset for the decomposition of CrN is observed at higher temperatures for coating-substrate systems than for stress free powders, at 1050 °C compared to 950 °C, at 1100 °C compared to 950 °C and above 1100 °C compared to 1000 °C for AlCrN, AlCrSi$_{2.5}$N and AlCrSi$_5$N, respectively. As synchrotron radiation provides an X-ray beam with high brilliance and thus superior signal-to-noise ratio and much better detection limit for small amounts of phases compared to a conventional XRD, it can be expected that the difference in the onset temperature of decomposition is even higher and the impact of the relaxed stresses is underestimated.

Furthermore, the decomposition of CrN into Cr_2N in the AlCrN-based systems, accompanied by a release of nitrogen, is critical for the behaviour of the coatings at elevated temperatures, since the associated formation of pores deteriorate the mechanical properties. Here, a positive impact of Si becomes

evident since the onset temperature is retarded to higher temperatures and the decomposition is decelerated with increasing Si content (Figure 2 and Figure 4). The impeded formation of Cr_2N can be attributed to the nano-composite structure of the AlCrSiN coatings, where the AlCr(Si)N crystals are embedded by the dense Si_xN_y tissue, which restricts the segregation of atoms to small distances within the separated nano-grains [24]. Similar to the prohibited diffusion of oxygen in AlTiN coatings alloyed with yttrium [51] or nc-TiN/a-Si_xN_y coatings [52] during oxidation, the strong and dense interface of the a-Si_xN_y hinders diffusion of nitrogen along the grain boundaries. Therefore, nitrogen can not be released from the crystal when CrN decomposes into Cr_2N, which effectively suppresses the further decomposition of CrN.

As a final step, Cr_2N starts to decompose at 1140 °C for AlCrN and, at 1280 °C and 1200 °C for AlCrSi$_{2.5}$N and AlCrSi$_5$N, respectively. The decomposition of Cr_2N is accompanied by the decomposition of Si_xN_y in the case of the Si containing coatings. Although the amount of Si in both Si containing coatings is relatively low, the endothermic peaks above 1200 °C are considerably high compared to AlCrN and all other reactions occurring during annealing (Figure 2). This is due to the superimposed contribution to the DSC signal of the decomposition reactions of Cr_2N and Si_xN_y. Additionally, the large enthalpy of formation of $\Delta H^0_{Si_xN_y} = -760\,\mathrm{kJ\,mol^{-1}}$ [53] compared to $\Delta H^0_{CrN} = -123\,\mathrm{kJ\,mol^{-1}}$ [54] and $\Delta H^0_{Cr_2N} = -234\,\mathrm{kJ\,mol^{-1}}$ [55] results in a considerably high endothermic heat flow when it decomposed.

Besides the thermal stability of the microstructure, the associated evolution of mechanical properties as a function of temperature is of major importance for the functionality of coatings at elevated temperatures. Obtaining a remarkable high hardness of ceramic hard coatings, representing a key property determining together with elastic modulus its wear resistance, can be approached by: (i) selecting materials with intrinsically high hardness (e.g. diamond, hydrogen-free diamond-like carbon, cubic boron nitride); (ii) the effect of ion bombardment during deposition; and (iii) microstructural design of coatings with heterogeneous microstructure such as nano-composites [39]. While a hardness enhancement by energetic ion bombardment is associated with a decrease in crystallite size, densification and the generation of high defect densities accompanied by the development of compressive residual stress, enhanced hardness of nanostructured materials is a result of hindered dislocation movement among fine-grained constituents with different lattice structures [47]. The high hardness of coatings obtained by an intense ion bombardment during deposition is typically not maintained at temperatures significantly above deposition temperature, since recovery effects lead to a reduction of compressive residual stress. Contrary, the high hardness of nano-composite materials can be preserved to temperatures above 1000 °C [56], as crystallite growth is suppressed by the amorphous tissue embedding the nano-crystallites. Within the AlTiN and AlCrN systems, many attempts have been made to stabilize the material in its cubic configuration [12, 57, 58] due to the enhanced mechanical properties compared to its hexagonal con-

9

figuration. Although the cubic modification may be favoured in terms of mechanical properties for applications at moderate temperatures, considerable constraints may arise from its metastable nature at elevated temperatures, as hardness drops with the formation of hexagonal phase fractions.

In the case of the AlCr(Si)N coatings studied in this work, the hardness at room temperature and after annealing can be attributed to (i) the formed phases, (ii) the amount of residual stress and (iii) the microstructural design focused on the formation of a nano-composite. At room temperature, AlCrN exhibits the highest hardness, since it is the only coating with purely cubic phase. The reduced hardness of the Si-containing coatings is mainly related to the formation of an additional hexagonal phase. Neither the nano-composite structure (and thus smaller grain size), nor the increased compressive residual strain can compensate the loss of hardness resulting from the formation of larger fractions of the much softer hexagonal phase. However, the advantage of Si as an alloying element in the AlCrN system becomes evident while looking at the hardness development of the coatings after vacuum annealing at 1100 °C. While AlCrN without Si suffers from a large drop in hardness of 5 GPa, mainly due to the phase transformation of the metastable cubic into the thermodynamically more stable hexagonal phase (Figure 3a and Figure 4) and a simultaneous reduction of the compressive residual strain towards slight tensile strain (Figure 6), the hardness of both Si-containing coatings increases of about 2 GPa after annealing. Similar to AlCrN, lattice defects and compressive residual strain are not stable above deposition temperature and vanish to a large extent (Figure 5 and Figure 6). Therefore, the stabilized (or even increasing) hardness can be related to the nano-composite microstructure, where mainly two processes should be considered as an explanation for the increase after annealing. At first, an incomplete phase segregation during deposition is completed upon annealing [39]. Secondly, additional hexagonal AlN precipitates form during annealing, accompanied by coherency strains hindering plastic deformation with a subsequent increase in hardness [9]. While the coherency strains in single-phase AlCrN contribute to age hardening limited to a maximum in hardness at 700 °C [9], the enhanced hardness of $AlCrSi_{2.5}N$ and $AlCrSi_5N$ in this work is still observed at 1100 °C. Finally, the suppressed formation of Cr_2N in the Si-containing coatings (accompanied by the release of nitrogen and the formation of pores) to temperatures above 1100 °C is an important factor to preserve the hardness. Summarized, while a single-phase cubic crystal structure seems beneficial in terms of mechanical properties at a first glance, the nano-composite and dual-phase cubic and hexagonal structure outperforms its mono-phase counterparts at elevated temperatures and makes the AlCrSiN coatings studied in this work promising candidates for high-temperature applications.

5. Summary and Conclusions

Three arc evaporated coatings, AlCrN, $AlCrSi_{2.5}N$ and $AlCrSi_5N$, were investigated and the impact of Si on (i) the phase formation, (ii) thermal stability and (iii) mechanical properties as a function of temperature was studied. Using the novel in-situ HT-HE-GIT-XRD allowed for measuring the temperature-dependent variations of the coating microstructure of the coating on a substrate (in contrast to powdered coatings). The unique combination of the in-situ HT-HE-GIT-XRD method with conventional DSC and TG revealed a significant impact of sample preparation in stress-free powders, resulting in a 100 °C lower onset temperature of the decomposition of CrN into Cr_2N when measuring powdered samples compared to the coating-substrate systems. The addition of Si resulted in the formation of (i) a nano-composite and (ii) dual-phase cubic and hexagonal structure with enhanced thermal stability and improved mechanical properties at elevated temperatures. This is evident by the shift of the onset temperature for the decomposition of CrN into Cr_2N of 100 °C, related to encapsulated AlCr(Si)N crystals in an $a\text{-}Si_xN_y$ tissue phase, where nitrogen diffusion is suppressed. Furthermore, the dual-phase crystal structure reveals its benefits at elevated temperatures, since the hardness of the Si containing coatings increased by ∼ 2 GPa to almost 30 GPa after annealing at 1100 °C, while the hardness of AlCrN dropped from 32 GPa to 26 GPa. The hardness increase after annealing is related to a thermally much more stable nano-composite structure (suppressed grain growth) with hindered dislocation movement due to the $a\text{-}Si_xN_y$ tissue phase, and to age hardening effects of a dual-phase cubic and hexagonal structure at temperatures above 1100 °C. The findings emphasize the potential of Si as an eminently suitable alloying element to enhance the thermal stability of the AlCrN system. The formation of a nano-composite structure, consisting of dual-phase cubic and hexagonal crystallites embedded in an $a\text{-}Si_xN_y$ tissue, and the enhanced mechanical properties at elevated temperatures make the AlCrSiN coatings promising candidates for high-temperature applications.

6. Acknowledgements

References

[1] J. Keckes, R. Daniel, J. Todt, J. Zalesak, B. Sartory, S. Braun, J. Gluch, M. Rosenthal, M. Burghammer, C. Mitterer, et al. 30 nm X-ray focusing correlates oscillatory stress, texture and structural defect gradients across multilayered TiN-SiOx thin film. *Acta Materialia*, 144:862–873, 2018.

[2] J. Zalesak, M. Bartosik, R. Daniel, C. Mitterer, C. Krywka, D. Kiener, PH. Mayrhofer, and J. Keckes. Cross-sectional structure-property relationship in a graded nanocrystalline Ti1- xAlxN thin film. *Acta Materialia*, 102:212–219, 2016.

[3] R. Daniel, M. Meindlhumer, W. Baumegger, J. Zalesak, B. Sartory, M. Burghammer, C. Mitterer, and J. Keckes. Grain boundary design of thin films: using tilted brittle interfaces for multiple crack deflection toughening. *Acta Materialia*, 122:130–137, 2017.

[4] S. Klima, N. Jäger, H. Hruby, C. Mitterer, J.F. Keckes, M. Burghammer, and R. Daniel. Structure-stress relationships in nanocrystalline multilayered Al0.7Cr0.3N/Al0.9Cr0.1N coatings studied by cross-sectional X-ray nanodiffraction. *Materials & Design*, 170:107702, 2019.

[5] N. Jäger, S. Klima, H. Hruby, J. Julin, M. Burghammer, J.F. Keckes, C. Mitterer, and R. Daniel. Evolution of structure and residual stress of a fcc/hex-AlCrN multi-layered system upon thermal loading revealed by cross-sectional X-ray nano-diffraction. *Acta Materialia*, 162:55 – 66, 2019.

[6] G. List, G. Sutter, and A. Bouthiche. Cutting temperature prediction in high speed machining by numerical modelling of chip formation and its dependence with crater wear. *International Journal of Machine Tools and Manufacture*, 54-55:1–9, 2012.

[7] U. Schleinkofer, C. Czettl, and C. Michotte. Coating Applications for Cutting Tools. In *Comprehensive Hard Materials*, pages 453–469. Elsevier, 2014.

[8] C. Mitterer. PVD and CVD Hard Coatings. In *Comprehensive Hard Materials*, pages 449–467. Elsevier, 2014.

[9] H. Willmann, P. H. Mayrhofer, L. Hultman, and C. Mitterer. Hardness evolution of Al–Cr–N coatings under thermal load. *Journal of Materials Research*, 23(11):2880–2885, 2008.

[10] H. Willmann, P. H. Mayrhofer, L. Hultman, and C. Mitterer. Thermal stability and age hardening of supersaturated AlCrN hard coatings. *International Heat Treatment and Surface Engineering*, 1(2):75–79, 2013.

[11] C. Sabitzer, J. Paulitsch, S. Kolozsvári, R. Rachbauer, and P. H. Mayrhofer. Influence of bias potential and layer arrangement on structure and mechanical properties of arc evaporated Al–Cr–N coatings. *Vacuum*, 106:49–52, 2014.

[12] A. E. Reiter, V. H. Derflinger, B. Hanselmann, T. Bachmann, and B. Sartory. Investigation of the properties of Al1−xCrxN coatings prepared by cathodic arc evaporation. *Surface and Coatings Technology*, 200(7):2114–2122, 2005.

[13] M. Kawate, A. Kimura, and T. Suzuki. Microhardness and lattice parameter of Cr1−xAlxN films. *Journal of Vacuum Science & Technology A: Vacuum, Surfaces, and Films*, 20(2):569–571, 2002.

[14] H. Willmann, P. H. Mayrhofer, P.O.Å. Persson, A. E. Reiter, L. Hultman, and C. Mitterer. Thermal stability of Al–Cr–N hard coatings. *Scripta Materialia*, 54(11):1847–1851, 2006.

[15] J. Soldán, J. Neidhardt, B. Sartory, R. Kaindl, R. Čerstvý, P. H. Mayrhofer, R. Tessadri, P. Polcik, M. Lechthaler, and C. Mitterer. Structure–property relations of arc-evaporated Al–Cr–Si–N coatings. *Surface and Coatings Technology*, 202(15):3555–3562, 2008.

[16] T. Polcar, T. Vitu, J. Sondor, and A. Cavaleiro. Tribological Performance of CrAlSiN Coatings at High Temperatures. *Plasma Processes and Polymers*, 6(S1):S935–S940, 2009.

[17] C. Tritremmel, R. Daniel, M. Lechthaler, P. Polcik, and C. Mitterer. Influence of Al and Si content on structure and mechanical properties of arc evaporated Al–Cr–Si–N thin films. *Thin Solid Films*, 534:403–409, 2013.

[18] J. L. Endrino, S. Palacín, A. Gutiérrez, F. Schäffers, and J. E. Krzanowski. Low and increased solubility of silicon in metal nitrides: Evidence by X-ray absorption near edge structure. *J Mater Sci*, 42(17):7607–7610, 2007.

[19] S. Veprek and M. Jilek. Super- and ultrahard nanocomposite coatings: generic concept for their preparation,properties and industrial applications. *Vacuum*, 67:443–449, 2002.

[20] L. Castaldi, D. Kurapov, A. Reiter, V. Shklover, P. Schwaller, and J. Patscheider. High temperature phase changes and oxidation behavior of Cr–Si–N coatings. *Surface and Coatings Technology*, 202(4-7):781–785, 2007.

[21] J. Musil, R. Daniel, J. Soldán, and P. Zeman. Properties of reactively sputtered W–Si–N films. *Surface and Coatings Technology*, 200(12-13):3886–3895, 2006.

[22] K. Lukaszkowicz, K. Labisz, M. Basiaga, and E. Jonda. Nano-Scale Structure Investigation of Vapour Deposited AlCrSiN Coating Using Transmission Electron Microscope Techniques. *Archives of Metallurgy and Materials*, 61(2):837–842, 2016.

[23] W. Wu, W. Chen, Shubao Yang, Y. Lin, S. Zhang, T. Cho, G. H. Lee, and S. Kwon. Design of AlCrSiN multilayers and nanocomposite coating for HSS cutting tools. *Applied Surface Science*, 351:803–810, 2015.

[24] S. Veprek, H.-D. Männling, M. Jilek, and P. Holubar. Avoiding the high-temperature decomposition and softening of (Al1−xTix)N coatings by the formation of stable superhard nc-(Al1−xTix)N/a-Si3N4 nanocomposite. *Materials Science and Engineering: A*, 366(1):202–205, 2004.

[25] T. Polcar and A. Cavaleiro. High temperature properties of CrAlN, CrAlSiN and AlCrSiN coatings – Structure and oxidation. *Materials Chemistry and Physics*, 129(1-2):195–201, 2011.

[26] T. Vopát, M. Haršáni, M. Kuruc, V. Šimna, R. Zaujec, J. Peterka, and L. Čaplovič. Effect of Substrate Bias and Coating Thickness on the Properties of nc-AlCrN/a-SixNy Hard Coating and Determination of Cutting Parameters. In *Solid State Phenomena*, volume 261, pages 229–236. Trans Tech Publ, 2017.

[27] M. Meindlhumer, J. Zalesak, R. Pitonak, J. Todt, B. Sartory, M. Burghammer, A. Stark, N. Schell, R. Daniel, J. F. Keckes, et al. Biomimetic hard and tough nanoceramic Ti–Al–N film with self-assembled six-level hierarchy. *Nanoscale*, 2019.

[28] M. Meindlhumer, S. Klima, N. Jäger, A. Stark, H. Hruby, C. Mitterer, J. Keckes, and R. Daniel. Stress-controlled decomposition routes in cubic AlCrN films assessed by in-situ high-temperature high-energy grazing incidence transmission X-ray diffraction. *Scientific Reports*, 9(1):18027, December 2019.

[29] A. P. Hammersley, S. O. Svensson, M. Hanfland, A. N. Fitch, and D. Hausermann. Two-dimensional detector software: From real detector to idealised image or two-theta scan. *High Pressure Research*, 14(4-6):235–248, 1996.

[30] J. Kieffer and D. Karkoulis. PyFAI, a versatile library for azimuthal regrouping. *Journal of Physics: Conference Series*, 425(20):202012, 2013.

[31] W.C. Oliver and G.M. Pharr. Measurement of hardness and elastic modulus by instrumented indentation: Advances in understanding and refinements to methodology. *J. Mater. Res.*, 2004(19):3–20, 2004.

[32] A. Hörling, L. Hultman, M. Odén, J. Sjölén, and L. Karlsson. Thermal stability of arc evaporated high aluminum-content Ti1-xAlxN thin films. *Journal of Vacuum Science & Technology A: Vacuum, Surfaces, and Films*, 20(5):1815–1823, 2002.

[33] T. Shimoo and K. Okamura. Interaction of Si3N4 with Cr. *Journal of Materials Science*, 1994(29):2231–2237, 1994.

[34] R. Daniel, J. Keckes, I. Matko, M. Burghammer, and C. Mitterer. Origins of microstructure and stress gradients in nanocrystalline thin films: The role of growth parameters and self-organization. *Acta Materialia*, 61(16):6255–6266, 2013.

[35] S. Vepřek. The search for novel, superhard materials. *Journal of Vacuum Science & Technology A: Vacuum, Surfaces, and Films*, 17(5):2401–2420, sep 1999.

[36] S. Q. Wang, L. Chen, B. Yang, K. K. Chang, Y. Du, J. Li, and T. Gang. Effect of Si addition on microstructure and mechanical properties of Ti–Al–N coating. *International Journal of Refractory Metals and Hard Materials*, 28(5):593–596, sep 2010.

[37] E. Martinez, R. Sanjinés, A. Karimi, J. Esteve, and F. Lévy. Mechanical properties of nanocomposite and multilayered Cr–Si–N sputtered thin films. *Surface and Coatings Technology*, 180-181:570–574, mar 2004.

[38] J. Patscheider. Nanocomposite hard coatings for wear protection. *MRS bulletin*, 28(3):180–183, 2003.

[39] S. Veprek, M. GJ Veprek-Heijman, P. Karvankova, and J. Prochazka. Different approaches to superhard coatings and nanocomposites. *Thin solid films*, 476(1):1–29, 2005.

[40] J. Musil, J. Vlček, and P. Zeman. Hard amorphous nanocomposite coatings with oxidation resistance above 1000°C. *Advances in Applied Ceramics*, 107(3):148–154, may 2008.

[41] P.H. Mayrhofer, D. Music, Th. Reeswinkel, H.-G. Fuß, and J.M. Schneider. Structure, elastic properties and phase stability of Cr1−xAlxN. *Acta Materialia*, 56(11):2469–2475, jun 2008.

[42] D. Holec, F. Florian Rovere, P. H. Mayrhofer, and P. B. Barna. Pressure-dependent stability of cubic and wurtzite phases within the TiN–AlN and CrN–AlN systems. *Scripta Materialia*, 62(6):349–352, mar 2010.

[43] H. Euchner and P.H. Mayrhofer. Vacancy-dependent stability of cubic and wurtzite Ti1-xAlxN. *Surface and Coatings Technology*, 275:214–218, aug 2015.

[44] P. H. Mayrhofer, D. Music, and J. M. Schneider. Influence of the Al distribution on the structure, elastic properties, and phase stability of supersaturated Ti1-xAlxN. *Journal of Applied Physics*, 100(9):094906, nov 2006.

[45] M. Hans, D. Music, Y. Chen, L. Patterer, A. O. Eriksson, D. Kurapov, J. Ramm, M. Arndt, H. Rudigier, and J. M. Schneider. Crystallite size-dependent metastable phase formation of TiAlN coatings. *Scientific Reports*, 7(1):16096, November 2017.

[46] P.H. Mayrhofer, R. Rachbauer, D. Holec, F. Rovere, and J.M. Schneider. Protective Transition Metal Nitride Coatings. In *Comprehensive Materials Processing*, pages 355–388. Elsevier, 2014.

11

[47] C Mitterer, P.H Mayrhofer, and J Musil. Thermal stability of PVD hard coatings. *Vacuum*, 71(1-2):279–284, may 2003.

[48] M. Bartosik, R. Daniel, Z. Zhang, M. Deluca, W. Ecker, M. Stefenelli, M. Klaus, C. Genzel, C. Mitterer, and J. Keckes. Lateral gradients of phases, residual stress and hardness in a laser heated Ti0.52Al0.48N coating on hard metal. *Surface and Coatings Technology*, 206(22):4502 – 4510, 2012.

[49] M Bartosik, C Rumeau, R Hahn, ZL Zhang, and PH Mayrhofer. Fracture toughness and structural evolution in the TiAlN system upon annealing. *Scientific reports*, 7(1):16476, 2017.

[50] N. Schalk, C. Mitterer, J. Keckes, M. Penoy, and C. Michotte. Influence of residual stresses and grain size on the spinodal decomposition of metastable Ti1-xAlxN coatings. *Surface and Coatings Technology*, 209:190 – 196, 2012.

[51] LA. Donohue, DB. Lewis, WD. Münz, MM. Stack, SB. Lyon, HW. Wang, and D. Rafaja. The influence of low concentrations of chromium and yttrium on the oxidation behaviour, residual stress and corrosion performance of TiAlN hard coatings on steel substrates. *Vacuum*, 55(2):109–114, 1999.

[52] J. Musil and P. Zeman. Hard a-Si3N4/MeNx Nanocomposite Coatings with High Thermal Stability and High Oxidation Resistance. *Solid State Phenomena*, 127:31–36, sep 2007.

[53] I. Tomaszkiewicz. Thermodynamics of Silicon Nitride. Standard molar enthalpy of formation of amorphous Si3N4 at 298.15 K. *Journal of Thermal Analysis and Calorimetry*, 65(2):425–433, 2001.

[54] S. Hofmann and H. A. Jehn. Oxidation behavior of CrNx and (Cr,Al)Nx hard coatings. *Werkstoffe und Korrosion*, 41(12):756–760, 1990.

[55] M. Widenmeyer, E. Meissner, A. Senyshyn, and R. Niewa. On the Formation Mechanism of Chromium Nitrides: An in situ Study. *Zeitschrift für anorganische und allgemeine Chemie*, 640(14):2801–2808, 2014.

[56] H.-D. Männling, D.S. Patil, K. Moto, M. Jilek, and S. Veprek. Thermal stability of superhard nanocomposite coatings consisting of immiscible nitrides. *Surface and Coatings Technology*, 146-147:263 – 267, 2001. Proceedings of the 28th International Conference on Metallurgic Coatings and Thin Films.

[57] NE. Christensen and I. Gorczyca. Calculated structural phase transitions of aluminum nitride under pressure. *Physical Review B*, 47(8):4307, 1993.

[58] M. Schlögl, J. Paulitsch, J. Keckes, and PH. Mayrhofer. Influence of AlN layers on mechanical properties and thermal stability of Cr-based nitride coatings. *Thin Solid Films*, 531:113–118, 2013.

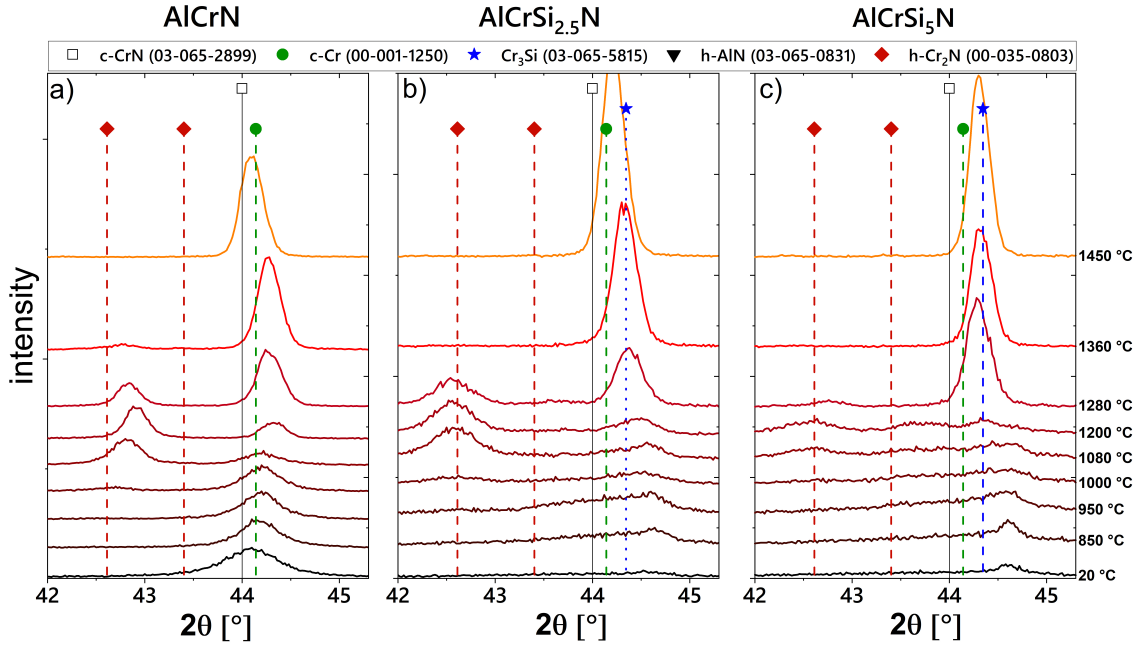12

Appendix A. Supplemental Material

Figure A.1: Detailed view of the X-ray diffractograms in the range from 42° to 45.5° of the (a) AlCrN, (b) AlCrSi$_{2.5}$N and (c) AlCrSi$_5$N coatings in the as-deposited state and after annealing at various temperatures in Ar atmosphere.
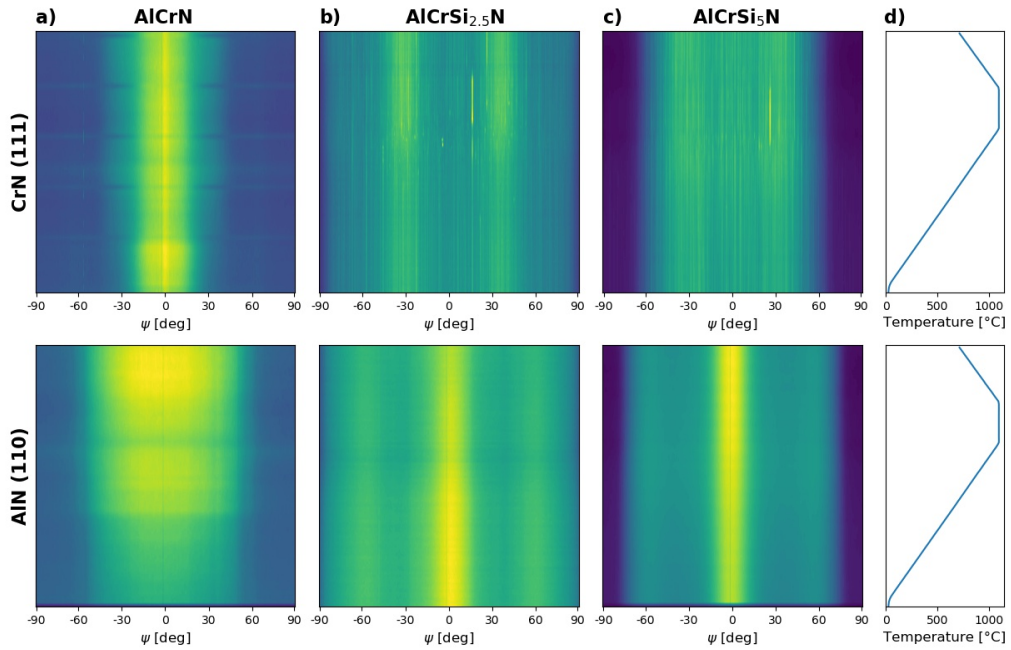

Figure A.2: Intensity of the CrN (111) and the AlN (110) diffractions peaks along the ψ angle as a function of temperature of (a) AlCrN, (b) AlCrSi$_{2.5}$N and (c) AlCrSi$_5$N, together with the (d) annealing temperature.

13

Publication III

Impact of Si on the high-temperature oxidation of AlCr(Si)N coatings

N. Jäger, M. Meindlhumer, M. Zítek, S. Spor, H. Hruby, F. Nahif, J. Julin, M. Rosenthal, J. Keckes, C. Mitterer, R. Daniel

Manuscript submitted to Journal of Materials Science & Technology.

Impact of Si on the high-temperature oxidation of AlCr(Si)N coatings

Jäger N.[a], Meindlhumer M.[a], Zítek M.[a], Spor S.[a,b], Hruby H.[b], Nahif F.[b], Julin J.[c,d], Rosenthal M.[e], Keckes J.[f,g], Mitterer C.[g], Daniel R.[a,g]

[a]*Christian Doppler Laboratory for Advanced Synthesis of Novel Multifunctional Coatings at the Department of Materials Science, Montanuniversität Leoben, Austria*
[b]*voestalpine eifeler Vacotec GmbH, Düsseldorf, Germany*
[c]*Institute of Ion Beam Physics and Materials Research, Helmholtz-Zentrum Dresden-Rossendorf, Dresden, Germany*
[d]*Department of Physics, University of Jyväskylä, Finland*
[e]*European Synchrotron Radiation Facility, Grenoble, France*
[f]*Erich Schmid Institute for Materials Science, Austrian Academy of Sciences, Austria*
[g]*Department of Materials Science, Montanuniversität Leoben, Austria*

Abstract

The resistance of wear protective coatings against oxidation is crucial for their use at high temperatures. Here, three nanocomposite AlCr(Si)N coatings with a fixed Al/Cr atomic ratio of 70/30 and a varying Si-content of 0 at.%, 2.5 at.% and 5 at.% were analyzed by differential scanning calorimetry, thermogravimetric analysis and X-ray diffraction in order to understand the oxidation behavior depending on their Si-content. Additionally, a partially oxidized AlCrSiN coating with 5 at.% Si was studied depth-resolved across the coating thickness by cross-sectional X-ray nanodiffraction and scanning transmission electron microscopy to investigate the elemental composition, morphology, phases and residual stress evolution of the oxide scale and the non-oxidized coating underneath. The results reveal enhanced oxidation properties of the AlCr(Si)N coatings with increasing Si-content, as demonstrated by a retarded onset of oxidation to higher temperatures from 1100 °C for AlCrN to 1260 °C for the Si-containing coatings and a simultaneous deceleration of the oxidation process. After annealing of the AlCrSiN sample with 5 at.% Si at an extraordinary high temperature of 1400 °C for 60 min in ambient air, three zones developed throughout the coating strongly differing in their composition and structure: (i) a dense oxide layer comprising an Al-rich and a Cr-rich zone formed at the very top, followed by (ii) a fine-grained transition zone with incomplete oxidation and (iii) a non-oxidized zone with a porous structure. The varying elemental composition of these zones is furthermore accompanied by micro-structural variations and a complex residual stress development revealed by cross-sectional X-ray nanodiffraction. The results establish a deeper understanding of the oxidation behavior of AlCr(Si)N coatings depending on their Si-content and the associated elemental, microstructural and residual stress evolution during high-temperature oxidation.

Keywords: AlCrSiN, nanocomposite, cathodic arc, oxidation behaviour, cross-sectional X-ray nanodiffraction

1. Introduction

Ceramic hard coatings are widely used in industry to protect the surface of tools in various machining and forming applications. Ternary transition metal nitrides find widespread use due to their good mechanical properties, thermal stability and oxidation resistance. However, modern applications like high speed cutting or dry cutting demand for wear-protective coatings resisting high temperatures beyond 1000 °C in oxidative atmospheres [1] and stimulate the development of superior coatings with advanced microstructural and compositional design.

AlCrN coatings are widely used in industry due to their high hardness, thermal stability and oxidation properties resulting in an overall good resistance against wear [2, 3, 4, 5]. The AlCrN system can be stabilized in its face-centered cubic structure up to an Al-content of about 70 at.% on the metal sublattice, and exhibits an additional hexagonal close packed phase exceeding this critical solubility limit [6]. As the cubic AlCrN phase is thermally metastable, it decomposes at elevated temperatures into hexagonal Al(Cr)N and a Cr-enriched cubic Cr(Al)N phase[7]. In another step, c-Cr(Al)N decomposes into Cr_2N and finally Cr, accompanied by the release of nitrogen yielding a porous structure with undesirable mechanical properties [7, 8]. Several attempts

have been made to stabilize the AlCrN system in its cubic structure also at high temperatures by alloying [9, 10], applying a multi-layered structure [11, 12] or using a dedicated residual stress design [13, 14].

Besides thermal stability, also the resistance against corrosion and oxidation is important as the coatings are often exposed to aggressive lubricants and coolants and face high temperatures in ambient air. Regarding oxidation, AlCrN is superior to CrN, resulting from the formation of an Al-rich oxide layer slowing down the diffusion of oxygen into the coating [15]. The oxidation behavior can be further improved by alloying using various elements [16, 17, 18], of which Si is a promising candidate [19]. The solubility of Si in AlCrN is low [20] and Si segregates along grain boundaries to form an amorphous (a-)Si_xN_y phase [21]. The resulting MeN/a-Si_xN_y (Me = Al/Cr) nanocomposite structure is beneficial for the oxidation resistance as no continuous diffusion path along grain boundaries exists and intergranular diffusion of oxygen is suppressed [22].

While AlCrSiN coatings have been investigated in terms of oxidation resistance or tribological behaviour in ambient air, a detailed study about the elemental and microstructural changes during high-temperature oxidation including the residual stress development and the properties after oxidation is still missing. In our previous work, we investigated the thermal stability of three AlCr(Si)N coatings excluding oxidation processes [23]. In this work, the same coatings (AlCr(Si)N coatings with a fixed Al/Cr atomic ratio of 70/30 and a Si-content of 0 at.%, 2.5 at.% and 5 at.%) were investigated in terms of oxidation behavior. In a first step, the coatings were analysed by differential scanning calorimetry (DSC), thermogravimetric analysis (TA) and ex-situ X-ray diffraction (XRD) in order to understand the oxidation behavior as a function of Si-content. In a second step, the AlCrSiN coating with the highest oxidation resistance in the powdered state (5 at.% Si) was chosen to study the elemental and microstructural changes after high-temperature oxidation. For this purpose, the coating was partially oxidized by annealing it at 1400 °C for 60 min in ambient air. After oxidation, the sample comprising a 1.1 μm-thick oxide layer with a 3 μm-thick non-oxidized coating underneath was studied depth-resolved by cross-sectional X-ray nanodiffraction and scanning transmission electron microscope (STEM). The results reveal an increase of the onset of oxidation from 1100 °C to 1260 °C and a significantly slowed down oxidation for the AlCrSiN coatings compared to AlCrN. The beneficial oxidation behavior is mainly associated with a fundamental change in microstructure from columnar grains to a nanocomposite structure with

an a-Si_xN_y grain boundary phase embedding AlCr(Si)N crystallites. A detailed depth-resolved analysis of the partially oxidized AlCrSiN sample with 5 at.% Si revealed the formation of a dense oxide layer comprising an Al-rich followed by a Cr-rich zone at the very top of the coating, a transition zone with incomplete oxidation and relatively fine grains comprising mainly mullite, SiO_2 and AlN underneath, and a non-oxidized coating with some pores closest to the substrate. The separation of the partially oxidized coating into zones with completely different elemental composition and microstructures is associated with the formation of different crystal phases and a fluctuating residual stress development across the coating thickness, as shown by cross-sectional X-ray nanodiffraction and STEM experiments. The approach comparing AlCr(Si)N coatings with varying Si-content using DSC/TG and ex-situ XRD combined with depth-resolved analysis of the partially oxidized AlCrSiN sample using advanced cross-sectional X-ray nanodiffraction and STEM allows for a comprehensive understanding of the oxidation behavior of AlCrSiN coatings and the underlying diffusion processes and changes in elemental composition, residual stress and microstructure.

2. Experimental methods

2.1. Coating deposition

Three AlCr(Si)N coatings with varying Si-contents were deposited by cathodic arc evaporation using an industrial scale coating system (alpha400P, voestalpine eifeler-Vacotec) equipped with sets of six cathodes with a fixed Al/Cr atomic ratio of 70/30 and an elemental composition of $Al_{70}Cr_{30}$, $Al_{66.5}Cr_{28.5}Si_5$ and $Al_{63}Cr_{27}Si_{10}$, respectively. The coatings were deposited onto WC-Co, polished sapphire substrates and on mild steel foil mounted in onefold planetary rotation with a turning speed of 2 rpm. Prior to the deposition, the substrates were heated and plasma-etched to remove contaminants and activate the surface to promote coating adhesion. For all coatings, a pure reactive nitrogen atmosphere with a pressure of 4 Pa, a substrate temperature of 480 °C, an arc current on each cathode of 100 A and a substrate bias voltage of −100 V were used.

2.2. Coating characterization

While the oxidation behaviour of all three coatings was analysed by DSC and TG analysis and ex-situ XRD, the coating with the highest oxidation resistance deposited from the $Al_{63}Cr_{27}Si_{10}$ cathodes (denoted as

2

AlCrSi$_5$N) was selected to study the elemental and microstructural changes depth-resolved along the coating cross-section after high-temperature oxidation. For this purpose, an AlCrSi$_5$N sample on a sapphire substrate was oxidized at 1400 °C for 60 min in ambient air, aiming for a partially oxidized sample consisting of a distinct oxide layer and a still preserved underlying coating.

Fracture cross-sections of all coatings in the as-deposited state were analysed in terms of coating thickness and morphology using a scanning electron microscope (SEM) (Zeiss Leo1525, with 3 kV accelerating voltage, 30 μm aperture and an inLens detector). The elemental composition of the coatings in the as-deposited state were measured by Elastic Recoil Detection Analysis (ERDA) with a 43 MeV $^{35}Cl^{7+}$ ion beam. The analysed area was approximately 1.5 mm × 1.5 mm , the angle of the incoming beam was 75° with respect to the sample normal and the scattering angle was and the scattering angle was 31° with respect to the beam. The recoiling atoms and scattered $^{35}Cl^{7+}$ ions were detected using a Bragg Ionization Chamber. Additionally, a cross-section of the partially oxidized AlCrSi$_5$N coating was prepared by focused ion beam (FIB) microscopy in a ZEISS LEO 1540XB Crossbeam using decreasing currents from 500 pA to 20 pA for polishing while minimizing the Ga^+-ion damage. The sample was analyzed along the cross-section by energy dispersive X-ray spectroscopy (EDX) using 10 kV, a 60 μm aperture and the built-in Bruker Quantax standards for quantification.

For DSC and TG analysis, the coated steel foil was chemically removed using 10 mol % nitric acid and the remaining coating material was ground in an agate mortar to obtain a fine powder. The DSC and TG experiments were carried out in synthetic air using a Setaram Setsys Evo 2400 system. 20 mg of each powdered sample was heated up to 1460 °C using a heating rate of 20 K min^{-1} and cooled down at a cooling rate of 50 K min^{-1} after an isothermal holding time of 30 min. A second run with an empty crucible was performed under the same conditions to serve as a baseline. Furthermore, additional samples (20 mg each) were annealed at 900 °C, 1100 °C, 1200 °C, 1260 °C, 1320 °C and 1390 °C, respectively, applying the same heating/cooling rates without isothermal holding. X-ray diffractograms of the annealed powders were recorded using a diffractometer (Bruker D8 Advance) equipped with an energy-dispersive Sol-X detector and applying Cu-Kα radiation (8.04 keV).

In order to gain depth-resolved information about the coating microstructure, phases, defect density and resid-

ual stress development across the coating thickness of the partially oxidized AlCrSi$_5$N, a 30 μm thick lamella of the coating on a sapphire substrate was investigated by cross-sectional synchrotron X-ray nanodiffraction [24] performed at the nanofocus extension of the ID13 beamline at the European Synchrotron Radiation Facility (ESRF) in Grenoble, France [25]. A monochromatic, point focusing X-ray beam (E = 12.7 keV) with dimensions of 25 nm × 35 nm adjusted by Multilayer Laue Lenses [26] was used in transmission geometry. The sample was moved along the whole coating thickness in steps of 20 nm and the diffraction data for each position were collected by a Dectris Eiger 4M detector. Detector calibration was performed by a NIST corundum powder and the sample-to-detector distance was evaluated as 134.927 mm. The resulting data were processed using the PyFAI software package [27, 28]. For every ring, 24 radial data sets were obtained by the azimuthal integration within 15° wide sections. The full width at half maximum (FWHM) values were evaluated by fitting the diffraction peaks using a Pseudo-Voigt function. The X-ray elastic stress depth distribution was received by analysing the elliptical shape of the Debye-Scherrer rings [24]. The elastic constants $\frac{1}{2}s_2^{113}$ of 0.3252×10^{-5} MPa^{-1} for Al$_2$O$_3$, $\frac{1}{2}s_2^{113}$ of 0.4142×10^{-5} MPa^{-1} for Cr$_2$O$_3$ [29], $\frac{1}{2}s_2^{110}$ of 0.2848×10^{-5} MPa^{-1} for mullite [30] and $\frac{1}{2}s_2^{100}$ of 0.3903×10^{-5} MPa^{-1} for AlN [31] were used. All X-ray elastic constants were calculated using the Hill-type grain interaction model [32].

To study the microstructure and local variations in elemental composition of the individual regions of the partially oxidized AlCrSi$_5$N coating, high resolution and analytical scanning transmission electron microscopy investigations were performed using a probe-corrected STEM (FEI Titan^3 G2 60–300) operated at 300 kV, equipped with a silicon drift detector X-ray spectrometer (Super-X). The sample for TEM were prepared by focused ion beam (Orsay Physics Cobra Z-05) column attached to a field emission gun scanning electron microscope (Zeiss Auriga).

3. Results

3.1. Elemental composition

The elemental composition of the coatings in the as-deposited state obtained by ERDA is reported already in [23] and given in Table 1 for completeness. The Al/Cr ratio of the coatings is slightly lower compared to the cathodes (Al/Cr = 2.3), revealing an Al loss during deposition due to preferred gas scattering of the

3

Table 1: Elemental composition of the coatings obtained by ERDA.

Cathode composition	Coating composition [at.%]				
	Al	Cr	Si	N	Al/Cr
$Al_{70}Cr_{30}$	32.6	16.7	0	51.0	2.0
$Al_{66.5}Cr_{28.5}Si_5$	32.6	14.0	2.6	50.6	2.3
$Al_{63}Cr_{27}Si_{10}$	30.8	13.7	4.7	50.5	2.2

lighter Al atoms within the plasma [21]. In contrast, the Si-content in the coatings corresponds to its content in the particular cathodes. The nitrogen content in all coatings is close to 50 at.% and the contamination with oxygen is below 0.4 at.% for all coatings. For easier reading, the coatings are denoted as AlCrN, $AlCrSi_{2.5}N$ and $AlCrSi_5N$ throughout the paper, corresponding to the $Al_{70}Cr_{30}$, $Al_{66.5}Cr_{28.5}Si_5$ and $Al_{63}Cr_{27}Si_{10}$ cathodes used for deposition, respectively.

3.2. Impact of the Si-content on the oxidation behavior

SEM micrographs of fracture cross-section of AlCrN, $AlCrSi_{2.5}N$ and $AlCrSi_5N$ in the as-deposited state are shown in Figure 1. While AlCrN has a fine-grained columnar structure, the Si-containing coatings exhibit a more glassy and featureless morphology resulting from their nanocomposite structure with an even smaller grain size. The DSC signals and corresponding mass changes during annealing in ambient air to 1460 °C are presented in Figure 2. Additionally, X-ray diffractograms of powders annealed at selected temperatures (indicated by vertical lines in Figure 2) are shown in Figure 3. Additionally, a schematic showing the formation of the various phases as a function of temperature summarizing the results of the DSC/TG and the XRD experiments is presented in Figure 4. In the as-deposited state, the AlCrN coating is stabilized in the thermodynamically metastable cubic phase, as it is typical for an Al/Cr ratio of 2.3 [6, 33]. $AlCrSi_{2.5}N$ and $AlCrSi_5N$ exhibit a nanocomposite microstructure with dual-phase (hexagonal and cubic) crystallites embedded in an $a\text{-}Si_xN_y$ matrix [23]. The formation of the nanocomposite microstructure also resulted in a substantial grain refinement and a higher defect density reflected by broader diffraction peaks with lower intensity and hence a more noisy signal of the normalised diffractograms at RT in Figure 3. Up to 1100 °C, the only reactions taking place are recovery processes and the decomposition of the thermodynamically metastable c-AlCr(Si)N into the more stable h-Al(CrSi)N phase and a Cr-enriched c-Cr(AlSi)N phase. While recovery processes result in peaks with increasing intensity and decreasing FWHM with increasing annealing temperature,

the formation of h-Al(CrSi)N is evidenced by an increased intensity of the reflections stemming from the hexagonal phase (Figure 3). The contribution of both of these reactions to the DSC signal is relatively small compared to the oxidation processes at higher temperatures and hence results in only marginal buckles between 800 °C and 1100 °C in Figure 2a. A more detailed description of processes related to thermal stability excluding oxidation can be found in our previous paper [23].

A distinct deviation of the DSC signal from the baseline at 1100 °C for AlCrN marks the onset of oxidation for the coating without Si. An evidence of oxidation detected also by XRD is visible at 1200 °C in Figure 3a, where signals of Cr_2O_3 and Al_2O_3 emanate at 34° and 35°, respectively. The onset of oxidation is shifted to ~ 1260 °C for both Si containing coatings, indicated by the exothermic contribution to the DSC signal in Figure 2a. The oxidation of $AlCrSi_{2.5}N$ and $AlCrSi_5N$ proceeds relatively slowly up to 1300 °C, as indicated by a shallow increase of the DSC signal and very small peaks of oxide phases at 1320 °C in Figure 3b and c. Additionally, peaks corresponding to the Cr_2N phase at 40.2° and 43.6° emanating at 1200 °C in the X-ray diffractograms of all coatings reveal the decomposition of Cr-rich Cr(AlSi)N into Cr_2N, accompanied by the release of nitrogen. The nitrogen release partially compensates for the mass gain during oxidation, resulting in an almost constant mass signal up to 1260 °C in Figure 2b. A large exothermic contribution to the DSC signal with a maximum at 1260 °C for AlCrN (Figure 2a) can be related to the formation of h-Al(CrSi)N and accelerated oxidation of the coating. The latter is demonstrated by an increasing sample mass above 1260 °C (Figure 2b). The oxidation of $AlCrSi_{2.5}N$ and $AlCrSi_5N$ accelerates at 1300 °C as evidenced by a kink in the DSC signal (Figure 2a), a pronounced mass gain (Figure 2b) and an increasing contribution of the oxide phases to the X-ray diffractograms (Figure 3b and c). Since Si_xN_y is not stable at temperatures above 1300 °C in the presence of pure Cr, it decomposes and reacts with Cr while forming Cr_3Si [34]. This endothermic reaction leads to the buckles in the DSC signal obtained for $AlCrSi_{2.5}N$ and $AlCrSi_5N$ at ~ 1400 °C, as shown in Figure 2a. Additionally, the subsequent release of nitrogen results in a considerable mass loss for $AlCrSi_5N$ at 1400 °C (Figure 2b). The Cr_3Si phase formed in $AlCrSi_{2.5}N$ and $AlCrSi_5N$ above 1390 °C is also detected by XRD with peaks emanating at 39.5° and 44.3° (Figure 3b and c).

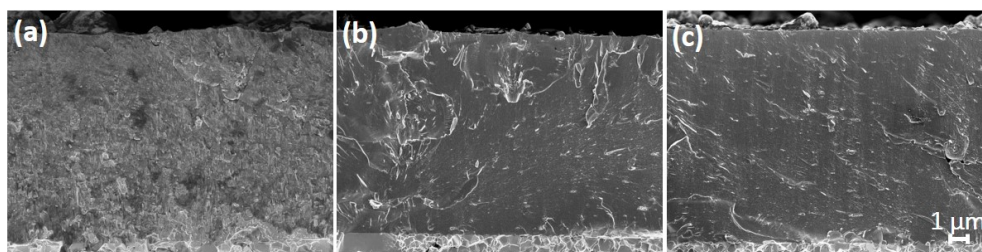During the isothermal holding period at the maximum temperature of 1460 °C, the heat flow declines and con-

Figure 1: SEM fracture cross-section images of (a) AlCrN, (b) AlCrSi$_{2.5}$N and (c) AlCrSi$_5$N coatings on a WC-Co substrates.
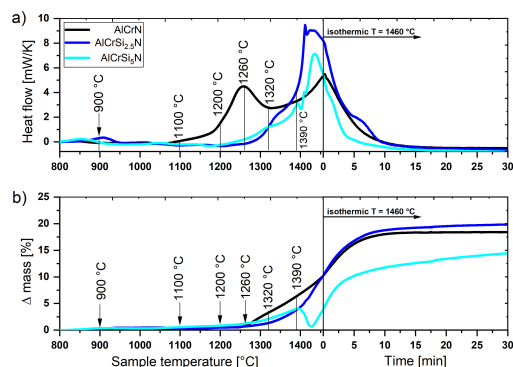

Figure 2: (a) DSC and (b) TG curves of AlCrN, AlCrSi$_{2.5}$N and AlCrSi$_5$N coating powders in ambient air. Annealing temperatures for ex-situ XRD measurements of powders are given.

verges to zero, which indicates a deceleration of the oxidation processes. While the AlCrN coating is fully oxidized after the annealing in ambient air (Figure 3a), oxidation processes are still not completed for AlCrSi$_{2.5}$N and AlCrSi$_5$N (Figure 3b and c). These findings are supported by the TG analysis (Figure 2b). While the mass of the AlCrN sample remains unchanged after 10 min of annealing at 1460 °C, the Si containing coatings changed their mass during the whole isothermal holding period (Figure 2b). The uncomplete oxidation of the Si-containing coatings is also confirmed by XRD, where small fractions of h-Al(CrSi)N are still observed at 1460 °C (Figure 3b and c). After annealing at the maximum temperature of 1460 °C, AlCrN consists only of an (Al/Cr)$_2$O$_3$ phase, while AlCrSi$_{2.5}$N and AlCrSi$_5$N are composed of a small h-Al(CrSi)N fraction and Al$_2$O$_3$, Cr$_2$O$_3$, SiO$_2$ and aluminosilicate phase (e.g. mullite, 3Al$_2$O$_3$·2SiO$_2$). While evenly shaped peaks located between the nominal peak positions corresponding to Al$_2$O$_3$ and Cr$_2$O$_3$ are visible for AlCrN (Figure 3a), peak splitting of the reflections stemming

from the oxide indicates a separation into Al-rich and Cr-rich oxide phases for AlCrSi$_{2.5}$N and AlCrSi$_5$N. The formation of the various phases as a function of temperature of the AlCrN, AlCrSi$_{2.5}$N and AlCrSi$_5$N coatings is summarized in Figure 4, illustrating the main differences in phase evolution during oxidation. While AlCrN is purely cubic in the as-deposited state, the Si-containing coatings exhibit a dual phase hexagonal and cubic structure, also resulting in a diminished formation of Cr$_2$N at elevated temperatures. Finally, AlCrSi$_{2.5}$N and AlCrSi$_5$N benefit form the formation of Cr$_3$Si and an oxide layer comprising Al$_2$O$_3$, Cr$_2$O$_3$, Si$_x$O$_y$ and some aluminosilicate, which results in overall reduced oxidation up to 1460 °C.

3.3. Cross-sectional characterisation of a partially oxidized AlCrSi$_5$N coating

In order to better understand local elemental and structural changes occurring during oxidation, a partially oxidized sample of AlCrSi$_5$N was studied depth-resolved across the coating thickness by cross-sectional X-ray nanodiffraction and TEM. AlCrSi$_5$N was selected as it showed the highest oxidation resistance during DSC/TG investigations. Due to its outstanding oxidation resistance, the coating had to be annealed at 1400 °C for 60 min in ambient air to induce oxidation to an extent, which allowed for formation of an oxide layer with sufficient thickness for further investigations. The partially oxidized sample consisted of an about 1.1 μm-thick oxide layer with a 3 μm-thick non-oxidized coating underneath (Figure 5a).

3.3.1. Cross-sectional X-ray nanodiffraction

In Figure 5, a cross-sectional SEM micrograph of the partially oxidized AlCrSi$_5$N coating is shown together with the evolution of phases, residual stress and the FWHM as a function of coating depth. Throughout the coating, three zones developed differing in their composition and structure: at the very top, a dense oxide
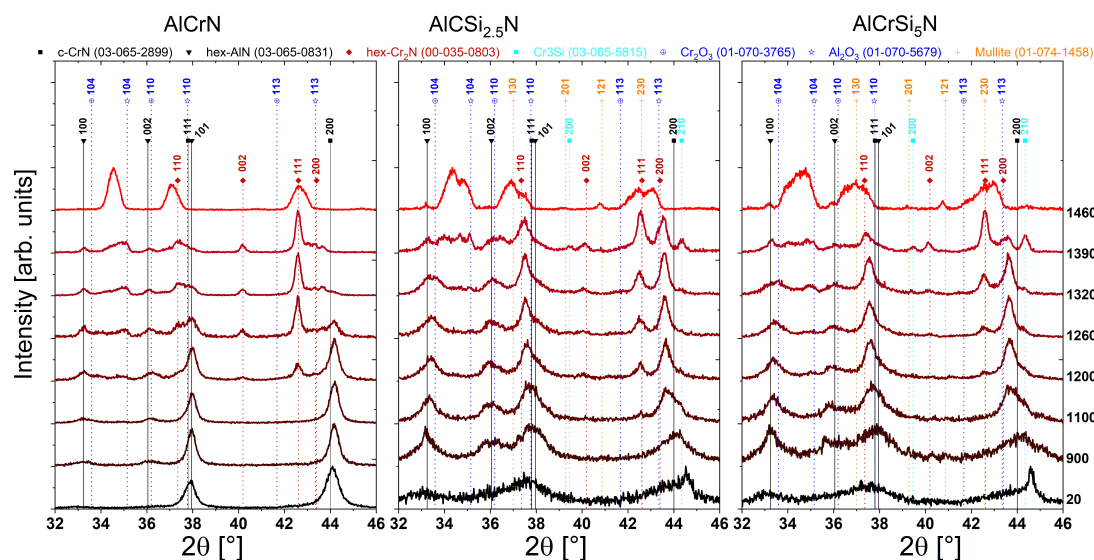
5

Figure 3: X-ray diffractograms of (a) AlCrN, (b) AlCrSi$_{2.5}$N and (c) AlCrSi$_5$N coatings in the as-deposited state and after annealing at various temperatures in ambient air. Diffractograms with extended 2θ angle are given in the supplementary Figure A.2 showing more details about the oxides formed in the Si-containing coatings after the DSC/TG experiment at 1460 °C.

layer with a thickness of about 1.1 μm formed, followed by a 1 μm thick transition zone with incomplete oxidation. Finally, a non-oxidized 2 μm-thick zone close to the substrate with some pores is formed.

The oxidation progress across the coating depth is documented by the elemental variations across the coating thickness shown in Figure 5a. The oxygen content of the oxide layer is between 55 at.% and 66 at.%, strongly decreasing throughout the transition zone reaching a minimum of about 7 at.% in the non-oxidized coating. Simultaneously, while almost no nitrogen is present in the oxide layer, the nitrogen content rises to about 35 at.% within the transition zone and is then constant for the non-oxidized coating underneath. The oxide layer is separated into an Al-rich part at the very top with a thickness of 400 nm and a Cr-rich, 700 nm-thick part below. Hardly any Si except close to the surface (~2 at.%) can be found in the oxide layer. While the Al-content increases within the transition zone to be constant at about 50 at.% for the non-oxidized coating, hardly any Cr can be found in the transition zone and the non-oxidized coating underneath. Only close to the substrate small amounts of Cr (2 at.%) can be found (Figure 5a). While an enrichment of Si in the transition zone with a maximum of about 15 at.% can be observed, it is constant for the non-oxidized coating at about 6 at.%.

The variation of the elemental composition is strongly

related to the phase evolution and corresponds to the formation of the three zones differing in their phase composition and microstructure (Figure 5b). The oxide layer is separated in Al$_2$O$_3$ at the very top and Cr$_2$O$_3$ underneath, both oxide phases exhibiting a trigonal crystal structure but a difference in their lattice constant. The transition zone below the oxide layer comprise numerous diffraction patterns with low intensity indicating the presence of phases varying in their elemental composition and oxidation state. They can be assigned to Al$_2$O$_3$, Cr$_2$O$_3$, mullite (3Al$_2$O$_3$·2SiO$_2$), SiO$_2$ and AlN. Finally, the non-oxidized part of the coating consists mainly of the h-Al(CrSi)N phase with the absence of c-Cr(AlSi)N, Cr$_2$N or c-Cr. Some chromium silicide phases (mainly Cr$_3$Si, but also minor amounts of CrSi and Cr$_5$Si$_3$) can be found close to the substrate at a coating depth between 3 μm and 4 μm. These findings (together with the EDX measurement) suggest that the Cr almost completely diffused into the oxide layer at the very top of the coating during oxidation. In Figure 5c, the residual stress development across the coating depth evaluated from the AlN 100, the Cr$_2$O$_3$ and Al$_2$O$_3$ 113 and the mullite 110 peak is depicted. The whole coating is compressively stressed with stresses ranging from −0.1 GPa to −1.5 GPa. A decrease of compressive residual stress with increasing distance from the surface from −1 GPa to −0.1 GPa is observed for Al$_2$O$_3$. The Cr$_2$O$_3$ phase
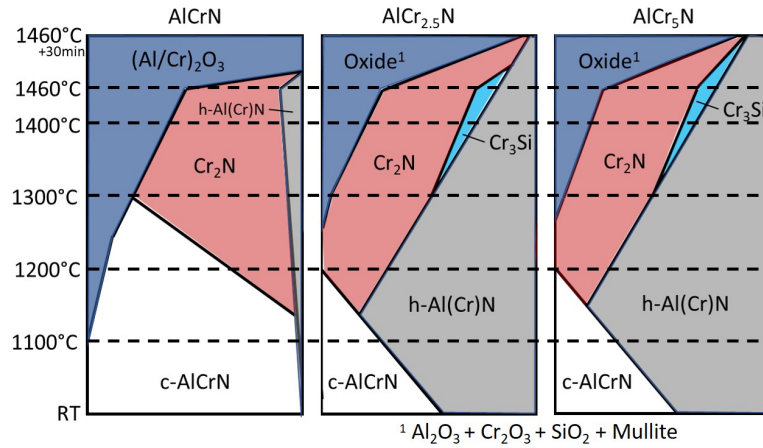
Figure 4: Evolution of phases of AlCrN, AlCrSi$_{2.5}$N and AlCrSi$_5$N coatings as a function of temperature.
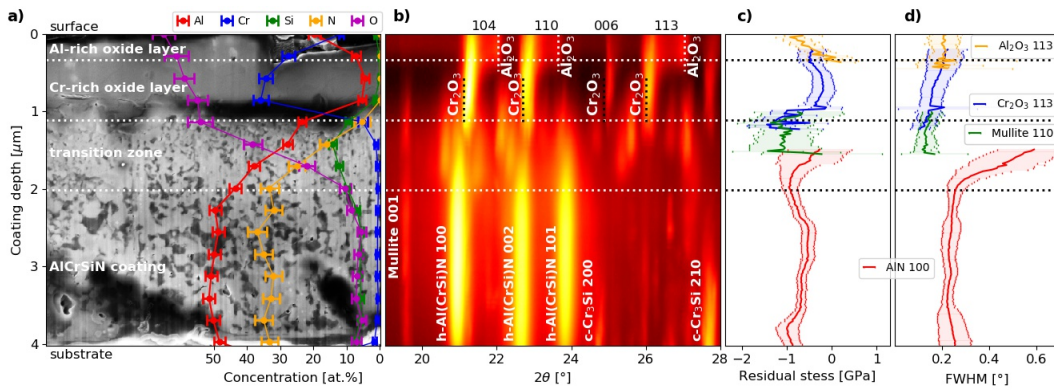

Figure 5: (a) SEM micrograph of the partially oxidized AlCrSi$_5$N sample on a sapphire substrate (with included EDX line-scans), (b) phase evolution, (c) the residual stress development and (d) the FWHM values as a function of coating depth.

exhibits a compressive stress of about $-0.2\,\mathrm{GPa}$, which is increasing to $-0.6\,\mathrm{GPa}$ and $-1.3\,\mathrm{GPa}$ towards the interfaces to the oxide layer and the transition zone, respectively. The highest compressive residual stress of the entire coating is found in the transition zone at about $-1.1\,\mathrm{GPa}$. Finally, the h-Al(CrSi)N phase is characterized by a constant compressive stress of $-0.6\,\mathrm{GPa}$ for the major part of the non-oxidized coating, rising up to $-1\,\mathrm{GPa}$ close to the transition zone and to the substrate. In Figure 5d, the FWHM is plotted as a function of coating depth. The FWHM of an X-ray diffraction peak correlates with the crystallite size and stresss of second and third order [35] and its changes, thus attributed to microstructural variations across the coating thick-

ness. The Al$_2$O$_3$, the Cr$_2$O$_3$ and the mullite phase exhibit FWHM values decreasing from 0.2° to 0.1° with increasing distance from the surface. FWHM values up to 0.6° for the h-Al(CrSi)N phase within the transition zone decreasing to 0.2° and being constant at this value for the non-oxidized coating indicate a smaller grain size of the transition zone compared to the non-oxidized coating underneath.

3.3.2. *TEM analysis of partially oxidized AlCrSi$_5$N*

For a better understanding of the microstructural and elemental variations along the cross-section of the partially oxidized AlCrSi$_5$N coating, STEM investigations including qualitative EDX measurements were performed. An overview of the sample cross-section

7

by high-angle annular dark field (HAADF) STEM is shown in Figure 6a, together with EDX mappings from selected areas at a higher magnification (Figure 6b-d). From top to bottom, three different zones of the coating can be clearly distinguished: a dense oxide layer at the very top, a transition zone between the fully oxidized and non-oxidized part of the coating and a non-oxidized $AlCrSi_5N$ coating at the bottom (Figure 6a). The oxide layer consists of an Al-rich layer (darker) and a Cr-rich layer below (brighter). The contrast can be referred to elements differing in their mass (atoms with higher atomic mass appear brighter). The elemental distribution of the oxide layer as determined by EDX (Figure 6b) reveals an Al-rich oxide layer with slightly lower oxygen content at the very top of the coating and an oxide layer consisting almost exclusively of Cr-oxide with a higher amount of oxygen underneath. A Si-rich domain containing hardly any Al and Cr and with less oxygen compared to the surrounding Al and Cr oxide phases can be found between the Al-rich and Cr-rich oxide layers (Figure 6b). An abrupt change in the composition from a high oxygen content towards a very low oxygen- and a high nitrogen-content indicates the interface between the oxide layer and the transition zone underneath. Besides the different composition, the transition zone is characterized by a slightly finer grained microstructure. A pronounced segregation of Al and Si during annealing resulted in the formation of Al- and Si-rich domains. Furthermore, the transition zone is strongly depleted of Cr, which is obviously concentrated only in macroparticles stemming from the deposition process. The non-oxidized coating underneath the transition zone exhibits a coarser grained microstructure, with an elemental composition similar to the one of the transition zone (Figure 6c). Cr in this region can be found also exclusively in macroparticles, which exhibit an increased amount of oxygen compared to the surrounding coating. During annealing, Al- and Si-rich domains were formed. Additionally, pores (originating from the N-release during decomposition of CrN into Cr_2N) surrounded by a dark, grey rim can be clearly seen in the HAADF STEM micrograph (Figure 6b). The rim of the pores is characterized by a low Al-, Cr- and N-content and consists mainly of Si and O.

4. Discussion

The oxidation resistance of ceramic hard coatings at high temperatures depends not only on their elemental composition but is also strongly affected by their crystallographic phases and their microstructure. The latter have a major impact on the oxidation behavior as oxidation is a highly diffusion-controlled process. Physical vapor deposited coatings typically exhibit a columnar grain structure and thus suffer from continuous diffusion paths along the grain boundaries directly connecting surface and substrate, a downside which can be overcome by an advanced microstructural design like multi-layered architectures or amorphous grain boundary phases [36]. Two main diffusion-related mechanisms are decisive for high-temperature oxidation: (i) the relative outward diffusion of coating elements, like Al, Cr, Si and N for the coatings in this work, and (ii) the relative inward diffusion of oxygen. The diffusion of substrate elements across the coating-substrate interface may also play a role but is neglected here as only powders and coatings on thermally highly stable sapphire substrates were investigated. The formation of an oxide layer on the top of the coating during early stages of oxidation strongly affects the inward diffusion of oxygen as well as the outward diffusion of coating elements. In general, elements forming dense oxide layers at the surface of the coaings are preferable as they act as protective passivation layers. An example is the improved oxidation resistance of AlCrN compared to CrN coatings, which is associated with the formation of an Al-rich oxide layer inhibiting the inward diffusion of oxygen [15]. The addition of Si also has a beneficial effect on the oxidation behavior of AlCr(Si)N coatings. Referring to the coatings investigated in this work, the onset of oxidation is shifted to higher temperatures from 1100 °C to 1260 °C for the Si-containing coatings compared to AlCrN, and the oxidation progress in the temperature range from 1200 °C to 1460 °C is slowed down significantly (Figure 2 and Figure 3). Si, similar to Al, forms dense, stable oxides as well and SiO_2 can be found in both oxidized Si-containing coatings (Figure 3 and Figure A.2). Additionally, SiO_2 and Al_2O_3 form stable chemical compounds with much lower enthalpy of formation (e.g. $\Delta H^0_{mullite} = -6819\,\text{kJ}\,\text{mol}^{-1}$) than Al_2O_3 ($\Delta H^0_{Al_2O_3} = -1676\,\text{kJ}\,\text{mol}^{-1}$), Cr_2O_3 ($\Delta H^0_{Cr_2O_3} = -1140\,\text{kJ}\,\text{mol}^{-1}$) or SiO_2 ($\Delta H^0_{SiO_2} = -911\,\text{kJ}\,\text{mol}^{-1}$) [37]. Therefore, an oxide layer tends to form already in early stages of oxidation inhibiting the inward diffusion of oxygen and thus slowing down the subsequent oxidation process. Since the addition of Si to the AlCrN-system also results in the nanocomposite structure and the a-Si_xN_y grain boundary phase accompanied by a considerable grain refinement and densification of the microstructure (Figure 1), inward diffusion of oxygen and outward diffusion of coating elements is further reduced as no continuous diffusion path along grain
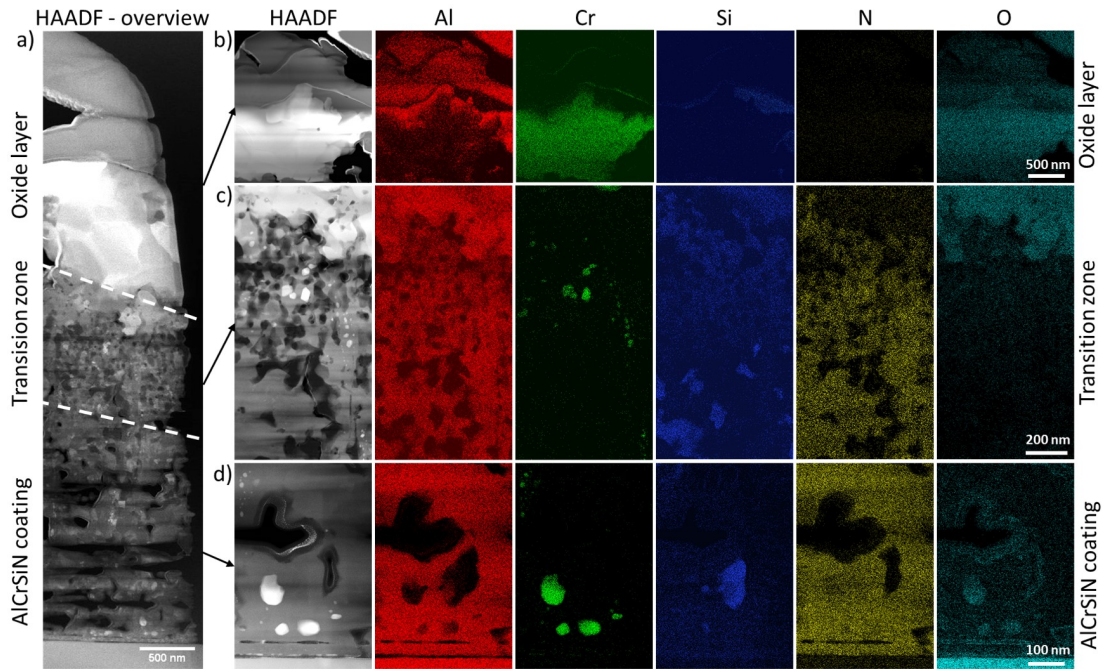
Figure 6: STEM micrographs of the partially oxidized AlCrSi$_5$N coating showing (a) an overview across the coating thickness as imaged by HAADF and EDX maps of (b) the oxide layer, (c) the transition zone and (d) the non-oxidized coating.

boundaries does exist anymore in contrast to the columnar microstructure of AlCrN [38]. This is also evident in the SEM micrographs of the powdered coatings after annealing at 1260 °C given in the supplementary Figure A.1. The surface morphology of areas where the top oxide layer chipped off allows for conclusions about the oxidation progress of the respective coatings. While the relatively rough surface morphology of AlCrN indicates that oxidation took place below the oxide layer too (Figure A.1a), the comparatively smooth surface morphology of the Si-containing coatings indicates a limitation of the oxidation process to a thin oxide layer at the top, protecting the coating underneath (Figure A.1b, c).

Another aspect influencing the oxidation behavior of the respective AlCr(Si)N coatings is the thermal stability of the individual phases of the AlCr(Si)N coatings. In general, thermally stable phases are preferable compared to those with undergoing phase transformations at elevated temperatures as changes in crystal structure are typically accompanied by volume changes resulting in new diffusion paths associated with a higher defect density or even formation of micro-cracks [39, 19]. The crystallographic structure of AlCrN strongly depends on the Al/Cr ratio and can be stabilized in the

thermodynamically metastable supersaturated face centered cubic solid solution phase up to an Al-content of ~ 70 at.% on the metallic sublattice [6, 33]. For higher Al-contents the hexagonal dense packed structure becomes more favorable. Si also promotes the formation of the hexagonal phase [23]. Since the coatings investigated in this work have an Al/Cr ratio close to the cubic-to-hexagonal transition, AlCrN is the only purely cubic coating while AlCrSi$_{2.5}$N and AlCrSi$_5$N exhibit a mixed hexagonal and cubic structure due to the additional Si (Figure 3). Due to the metastable nature of the c-AlCr(Si)N phase, it starts to decompose into Cr-rich c-Cr(AlSi)N and Al-rich h-Al(CrSi)N phases [23]. The formation of the hexagonal AlN phase is accompanied by a volume expansion of 26 % [40], which results in the above mentioned new diffusion paths. As this occurs to a much smaller extent for the Si-containing coatings (large amount of the hexagonal phase already present in the as-deposited state, Figure 3) and the individual crystallites are embedded in the a-Si$_x$N$_y$ matrix, AlCrSi$_{2.5}$N and AlCrSi$_5$N are much less affected by these phase changes at elevated temperatures and the oxidation progress is slowed down compared to AlCrN. At even higher temperatures, the Cr-enriched c-

9

Cr(AlSi)N phase starts to decompose into Cr_2N and finally into pure Cr, accompanied by the release of nitrogen [7]. These decomposition processes strongly affect the oxidation behavior in three different ways. Firstly, the release of nitrogen results in the formation of pores (Figure 5 and Figure 6) which facilitates enhanced diffusion (as surface diffusion is faster than bulk diffusion). Secondly, CrN has lower oxidation rates than those observed for Cr_2N [41]. The higher onset temperature and retarded progress for the decomposition of c-Cr(AlSi)N into Cr_2N and nitrogen, as shown in our previous work [23] and indicated by the X-ray diffractograms in Figure 3, therefore also contributes to the enhanced oxidation resistance of the Si-containing coatings. Finally, free, unbound Cr, as the final decomposition product, plays a major role in the oxidation process, as it was found to be more mobile compared to Al and thus diffuses faster to the surface where it forms surface oxides [42]. While Cr in AlCrN can easily diffuse to the surface where it forms Cr_2O_3, free Cr is limited in the Si-containing coatings as it is bound in form of Cr_3Si (Figure 3). Cr_3Si, as a chemical compound, can be assumed to have a much lower diffusivity than pure Cr, and thus outward diffusion of Cr is suppressed for the $AlCrSi_{2.5}N$ and $AlCrSi_5N$ coatings and the oxidation is slowed down. These findings are supported by X-ray reflections stemming from the Cr_3Si phase (at 2θ angles of $24.7°$ and $27.7°$ in Figure 5). The decreasing intensity of the X-ray reflections with increasing distance from the substrate towards the surface indicate that the outward diffusion of Cr is not fully completed yet and the Cr_3Si phase suppresses the diffusion.

The reduced Cr outward diffusion of the Si-containing coatings also affects the microstructure of the formed oxide layer. Usually, oxide layers with multi-layered structure are observed for AlCrN coatings [15, 43, 44]. Because of the higher mobility of Cr compared to Al, a Cr-rich oxide layer forms at the very top and an Al-rich oxide layer underneath. If the outward diffusion of Cr is prevented, for example by applying a TiN diffusion barrier as shown by Galindo et al. [42], the oxidation resistance of AlCrN coatings can be significantly enhanced. In the case of the Si-containing coatings of this work, the outwards diffusion of Cr is also strongly suppressed (as the free Cr is bonded to Si forming Cr_3Si which reduces its diffusion rate). As a result, a beneficial Al-rich oxide layer formed at the very top of the surface of the $AlCrSi_5N$ coating after annealing at $1400°C$ for one hour (Figure 6, Figure 5b), which is in contrast to AlCrN coatings of previous works where typically a Cr-rich oxide layer forms at the very top of the coatings [15, 43, 44].

The different oxidation behavior of the AlCr(Si)N coatings (suppressed outwards diffusion of Cr) also results in the formation of different oxides at the top of the coatings. While a mixed $(Al/Cr)_2O_3$ phase is observed for AlCrN, a separation into an Al_2O_3 and a Cr_2O_3 oxide is observed for $AlCrSi_{2.5}N$ and $AlCrSi_5N$ (Figure 3). Although the Al_2O_3-Cr_2O_3 system exhibits a distinctive miscibility gap below $1300°C$ [45], a solid solution of those oxides formed on AlCrN during oxidation at $1460°C$ and sustained during cooling to room temperature was found (Figure 3). In contrast, the additionally formed SiO_2 in the Si-containing coatings is highly soluble in Al_2O_3 [46] but not soluble in Cr_2O_3 in the whole temperature range [47]. This is the reason why Al_2O_3 and Cr_2O_3 separated and coexist in the oxide layer, as indicated by separated peaks emanating from each phase (Figure 3).

The annealing of the $AlCrSi_5N$ sample at the exceptional high temperature of $1400°C$ for 60 min in ambient air resulted in considerable diffusion of the respective coating elements, associated by the formation of an oxide layer and substantial phase changes of the non-oxidized coating underneath. Despite these extensive elemental and microstructural changes, a compressive residual stress state is preserved for the whole coating (Figure 5c) emphasizing the high thermal stability of the coating. The variations in the residual stress between $-0.1\,GPa$ and $-1.5\,GPa$ may originate from the thermal mismatch between the individual coating phases and/or coherency stresses between the different phases. Accordingly, the highest compressive stress within the whole coating can be found in the transition zone comprising the most different phases. Furthermore, slight pile-ups of heightened compressive stress can be found at the interfaces between the oxide layer and the transition zone, the transition zone and the non-oxidized coating and the coating-substrate interface.

The separation of the oxide at the top of the coating into phases with different elemental composition is accompanied by the formation of layers with different microstructures. While the Al-rich oxide layer seems to be finer grained (slightly larger FWHM in Figure 5d), the Cr-rich oxide and the mullite is a little bit coarser grained (indicated by smaller FWHM in Figure 5d). The Al(CrSi)N phase in the transition zone representing the oxidation front is relatively fine-grained as a result of the ongoing nucleation and formation of the oxide phases. The grain size increases towards the non-oxidized coating underneath and is constant for the $2\,\mu m$ thick part of the coating close to the substrate. The originally nanocomposite structure of the non-oxidized coating underneath has changed in favor of a relatively

coarse-grained microstructure. The coating elements strongly segregated and formed grains with individual high Al- and Si-content, while the Cr almost completely diffused to the top of the coating forming Cr_2O_3.

Summarized, Si has a beneficial impact on the oxidation behavior of the AlCrN-system already at relatively small concentrations up to 5 at.%. The main impact on the oxidation behavior has to be associated with the change in microstructure. While AlCrN has a two-dimensional microstructure with columnar grains allowing oxygen to diffuse along the grain boundaries, the addition of Si results in a three-dimensional nanocomposite microstructure where the AlCr(Si)N crystallites are embedded in an a-Si_xN_y tissue phase. The improved oxidation resistance of AlCrSiN coatings combined with their enhanced mechanical properties at high-temperatures (see our previous work [23]), makes the AlCrSiN coatings a perspective material for challenging high-temperature applications like high-speed or dry cutting.

5. Summary and conclusion

The oxidation behavior of arc evaporated AlCrN, $AlCrSi_{2.5}N$ and $AlCrSi_5N$ (fixed Al/Cr ratio of 70/30) was investigated by DSC/TG combined with ex-situ XRD. Additionally, a partially oxidized $AlCrSi_5N$ sample consisting of a 1.1 μm thick oxide layer on a 3 μm non-oxidized coating was cross-sectionally studied with respect to its elemental distribution, microstructure, formed phases and residual stress development by X-ray nanodiffraction and STEM. The beneficial effects rising from the addition of Si to the AlCrN-system can be summarized as follows:

- formation of a nanocomposite structure with a dense a-Si_xN_y grain boundary phase avoiding continuous diffusion paths along grain boundaries from the coating surface to the substrate

- pronounced grain refinement and densification of the microstructure

- retarded decomposition of CrN into Cr_2N and thus retarded formation of pores due to the released nitrogen

- diminished diffusion of chromium outwards due to the formation of Cr_3Si leading to a favored Al-rich oxide layer at the very top of the coating preventing oxygen from diffusing inward

- formation of dense, stable oxides (e.g. Si_xO_y and aluminosilicate) already during early stages of oxidation acting as passivation layers and slowing down oxidation

Cross-sectional X-ray nanodiffraction and STEM analysis after annealing an $AlCrSi_5N$ sample at 1400 °C for one hour revealed a partially oxidized coating consisting of a 1.1 μm thick oxide layer, a 1 μm thick transition zone below and a 2 μm thick non-oxidized coating below. The oxide layer is divided into an Al-rich part at the very top and a Cr-rich part underneath. The transition zone represents the area of ongoing oxidation and exhibits a finer grained microstructure. Finally, a 2 μm thick thick non-oxidized coating is still remaining, represented by completely segregated coating elements into individual grains and some pores.

Adding Si to the AlCrN-system results in the formation of a self-assembling nanocomposite microstructure with highly beneficial properties. This advanced microstructural design allows for controlling the diffusion paths of oxygen and coating elements through the coating and for governing the microstructure of the oxidation layer formed at the top protecting the coatings from further oxidation. As a result, the onset of oxidation was increased from 1100 °C to 1260 °C and the speed of the oxidation was slowed down significantly, which makes AlCrSiN coatings promising candidates for high-temperature applications such as high-speed or dry cutting.

6. Acknowledgments

References

[1] G. List, G. Sutter, and A. Bouthiche. Cutting temperature prediction in high speed machining by numerical modelling of chip formation and its dependence with crater wear. *International Journal of Machine Tools and Manufacture*, 54-55:1–9, 2012.

[2] E. Spain, JC. Avelar-Batista, M. Letch, J. Housden, and B. Lerga. Characterisation and applications of Cr–Al–N coatings. *Surface and Coatings Technology*, 200(5-6):1507–1513, 2005.

11

[3] L. Wang, X. Nie, J. Housden, E. Spain, JC. Jiang, EI. Meletis, A. Leyland, and A. Matthews. Material transfer phenomena and failure mechanisms of a nanostructured Cr–Al–N coating in laboratory wear tests and an industrial punch tool application. *Surface and Coatings Technology*, 203(5-7):816–821, 2008.

[4] Y. Benlatreche, C. Nouveau, R. Marchal, J-P F. Martins, and H. Aknouche. Applications of CrAlN ternary system in wood machining of medium density fibreboard (MDF). *Wear*, 267(5-8):1056–1061, 2009.

[5] T. Polcar and A. Cavaleiro. High-temperature tribological properties of CrAlN, CrAlSiN and AlCrSiN coatings. *Surface and Coatings Technology*, 206(6):1244–1251, 2011.

[6] M. Kawate, A. Kimura, and T. Suzuki. Microhardness and lattice parameter of Cr1−xAlxN films. *Journal of Vacuum Science & Technology A: Vacuum, Surfaces, and Films*, 20(2):569–571, 2002.

[7] H. Willmann, P. H. Mayrhofer, P. O. Å. Persson, A. E. Reiter, L. Hultman, and C. Mitterer. Thermal stability of Al–Cr–N hard coatings. *Scripta Materialia*, 54:1847–1851, 2006.

[8] M. Meindlhumer, S. Klima, N Jäger, A. Stark, H. Hruby, C. Mitterer, J. Keckes, and R. Daniel. Stress-controlled decomposition routes in cubic AlCrN films assessed by in-situ high-temperature high-energy grazing incidence transmission X-ray diffraction. *Scientific reports*, 9(1):1–14, 2019.

[9] Y. Feng, L. Zhang, R. Ke, Q. Wan, Z. Wang, and Z. Lu. Thermal stability and oxidation behavior of AlTiN, AlCrN and AlCrSiWN coatings. *International Journal of Refractory Metals and Hard Materials*, 43:241–249, 2014.

[10] R. Forsén, MP Johansson, M. Odén, and N. Ghafoor. Effects of Ti alloying of AlCrN coatings on thermal stability and oxidation resistance. *Thin Solid Films*, 534:394–402, 2013.

[11] Y. Chang, S. Weng, C. Chen, and F. Fu. High temperature oxidation and cutting performance of alcrn, tivn and multilayered alcrn/tivn hard coatings. *Surface and Coatings Technology*, 332:494–503, 2017.

[12] B. Xiao, J. Liu, F. Liu, X. Zhong, X. Xiao, T. Zhang, and Q. Wang. Effects of microstructure evolution on the oxidation behavior and high-temperature tribological properties of AlCrN/TiAlSiN multilayer coatings. *Ceramics international*, 44(18):23150–23161, 2018.

[13] N. Jäger, S. Klima, H. Hruby, J. Julin, M. Burghammer, JF. Keckes, C. Mitterer, and R. Daniel. Evolution of structure and residual stress of a fcc/hex-AlCrN multi-layered system upon thermal loading revealed by cross-sectional X-ray nano-diffraction. *Acta Materialia*, 162:55–66, 2019.

[14] S Klima, N Jäger, H Hruby, C Mitterer, JF Keckes, M Burghammer, and R Daniel. Structure-stress relationships in nanocrystalline multilayered Al0. 7Cr0. 3N/Al0. 9Cr0. 1N coatings studied by cross-sectional X-ray nanodiffraction. *Materials & Design*, 170:107702, 2019.

[15] A. E. Reiter, C. Mitterer, and B. Sartory. Oxidation of arc-evaporated Al1-xCrxN coatings. *J. Vac. Sci. Technol. A*, 25:711–720, 2007.

[16] JL. Endrino and V. Derflinger. The influence of alloying elements on the phase stability and mechanical properties of alcrn coatings. *Surface and Coatings Technology*, 200(1):988 – 992, 2005. PSE 2004.

[17] T. Polcar and A. Cavaleiro. Structure and tribological properties of alcrtin coatings at elevated temperature. *Surface and Coatings Technology*, 205:S107–S110, 2011.

[18] R. Franz, J. Neidhardt, C. Mitterer, B. Schaffer, H. Hutter, R. Kaindl, B. Sartory, R. Tessadri, M. Lechthaler, and P. Polcik. Oxidation and diffusion processes during annealing of AlCrVN hard coatings. *Journal of Vacuum Science & Technology A: Vacuum, Surfaces, and Films*, 26(2):302–308, 2008.

[19] C. Tritremmel, R. Daniel, C. Mitterer, P. H. Mayrhofer, M. Lechthaler, and P. Polcik. Oxidation behavior of arc evaporated Al-Cr-Si-N thin films. *J. Vac. Sci. Technol. A*, 30:061501, 2012.

[20] J. L. Endrino, S. Palacín, A. Gutiérrez, F. Schäffers, and J. E. Krzanowski. Low and increased solubility of silicon in metal nitrides: Evidence by X-ray absorption near edge structure. *J Mater Sci*, 42(17):7607–7610, 2007.

[21] J. Soldán, J. Neidhardt, B. Sartory, R. Kaindl, R. Čerstvý, P. H. Mayrhofer, R. Tessadri, P. Polcik, M. Lechthaler, and C. Mitterer. Structure–property relations of arc-evaporated Al–Cr–Si–N coatings. *Surface and Coatings Technology*, 202(15):3555–3562, 2008.

[22] J. Musil and P. Zeman. Hard a-Si3N4/MeNx Nanocomposite Coatings with High Thermal Stability and High Oxidation Resistance. *Solid State Phenomena*, 127:31–36, 2007.

[23] N. Jäger, M. Meindlhumer, S. Spor, H. Hruby, J. Julin, A. Stark, F. Nahif, J. Keckes, C. Mitterer, and R. Daniel. Microstructural evolution and thermal stability of AlCr(Si)N hard coatings revealed by in-situ high-temperature high-energy grazing incidence transmission X-ray diffraction. *Acta Materialia*, 186:545–554, 2020.

[24] J. Keckes, R. Daniel, J. Todt, J. Zalesak, B. Sartory, S. Braun, J. Gluch, M. Rosenthal, M. Burghammer, C. Mitterer, S. Niese, and A. Kubec. 30 nm x-ray focusing correlates oscillatory stress, texture and structural defect gradients across multilayered tin-siox thin film. *Acta Materialia*, 144:862 – 873, 2018.

[25] C. Riekel, M. Burghammer, and R. Davies. Progress in micro- and nano-diffraction at the ESRF ID13 beamline. *IOP Conference Series: Materials Science and Engineering*, 14:012013, nov 2010.

[26] A. Kubec, K.n Melzer, J. Gluch, S. Niese, S. Braun, J. Patommel, M. Burghammer, and A. Leson. Point focusing with flat and wedged crossed multilayer Laue lenses. *Journal of Synchrotron Radiation*, 24(2):413–421, Mar 2017.

[27] G. Ashiotis, A. Deschildre, Z. Nawaz, J. P. Wright, D. Karkoulis, F. E. Picca, and J. Kieffer. The fast azimuthal integration Python library: *pyFAI. Journal of Applied Crystallography*, 48(2):510–519, Apr 2015.

[28] J. Kieffer and D. Karkoulis. PyFAI, a versatile library for azimuthal regrouping. *Journal of Physics: Conference Series*, 425(20):202012, mar 2013.

[29] Y. Wang, H. Fang, C. L. Zacherl, Z. Mei, S. Shang, L. Chen, P. D. Jablonski, and Z. Liu. First-principles lattice dynamics, thermodynamics, and elasticity of Cr2O3. *Surface Science*, 606(17):1422 – 1425, 2012.

[30] B. Hildmann, H. Ledbetter, S. Kim, and H. Schneider. Structural Control of Elastic Constants of Mullite in Comparison to Sillimanite. *Journal of the American Ceramic Society*, 84(10):2409–2414, 2001.

[31] J. Almer, U. Lienert, R. L. Peng, C. Schlauer, and M. Odén. Strain and texture analysis of coatings using high-energy X-rays. *Journal of Applied Physics*, 94(1):697–702, 2003.

[32] I. C. Noyan and J. B. Cohen. *Residual stress: measurement by diffraction and interpretation*. Springer, 2013.

[33] A. E. Reiter, V. H. Derflinger, B. Hanselmann, T. Bachmann, and B. Sartory. Investigation of the properties of Al1−xCrxN coatings prepared by cathodic arc evaporation. *Surface and Coatings Technology*, 200(7):2114–2122, 2005.

[34] T. Shimoo and K. Okamura. Interaction of Si3N4 with Cr. *Journal of Materials Science*, 1994(29):2231–2237, 1994.

[35] E. J. Mittemeijer and U. Welzel. The "state of the art" of the diffraction analysis of crystallite size and lattice strain. *Crystalline Materials*, 223(9):552–560, 2008.

[36] J. Musil. Hard nanocomposite coatings: Thermal stability, oxi-

dation resistance and toughness. *Surface and Coatings Technology*, 207:50–65, 2012.

[37] John Aurie Dean et al. *Lange's handbook of chemistry*, volume 15. McGraw-Hill New York, 1992.

[38] J. Musil, J. Vlček, and P. Zeman. Hard amorphous nanocomposite coatings with oxidation resistance above 1000°C. *Advances in Applied Ceramics*, 107:148–154, 2008.

[39] L. Hultman. Thermal stability of nitride thin films. *Vacuum*, 57:1–30, 2000.

[40] PH. Mayrhofer, D. Music, and JM. Schneider. Influence of the Al distribution on the structure, elastic properties, and phase stability of supersaturated Ti 1- x Al x N. *Journal of Applied Physics*, 100(9):094906, 2006.

[41] T. Kacsich, K. P. Lieb, A. Schaper, and O. Schulte. Oxidation of thin chromium nitride films: kinetics and morphology. *J. Phys.: Condens. Matter*, 8:10703–10719, 1996.

[42] R. Escobar Galindo, J. L. Endrino, R. Martínez, and J. M. Albella. Improving the oxidation resistance of AlCrN coatings by tailoring chromium out-diffusion. *Spectrochimica Acta Part B*, 65:950–958, 2010.

[43] S. Hofmann and H.A. Jehn. Oxidation behavior of CrNx and (Cr,AI)Nx hard coatings. *Werkstoffe und Korrosion*, 41:756–760, 1990.

[44] Y. Ide, T. Nakamura, and K. Kishitake. Formation of Al-Cr-N films by a DC reactive sputtering method and evaluation of their properties. In B. Mishra, Yamauchi C, B. Mishra, and C. Yamauchi, editors, *Proceedings of the Second International Conference on Processing Materials for Properties*, Proceedings of the Second International Conference on Processing Materials for Properties, pages 291–296, December 2000. Proceedings of the Second International Conference on Processing Materials for Properties ; Conference date: 05-11-2000 Through 08-11-2000.

[45] W. Sitte. Investigation of the Miscibility Gap of the System Chromia-Alumina below 1300 C. *Materials Science Monographs*, 28:451–456, 1985.

[46] N. L. Bowen and J. W. Greig. The system: Al2O3.SiO2. *Journal of the American Ceramic Society*, 7:238–254, 1924.

[47] T. M. Besmann, N. S. Kulkarni, and K. E. Spear. Thermochemical Analysis and Modeling of the Al2O3-Cr2O3, Cr2O3-SiO2, and Al2O3-Cr2O3-SiO2 Systems Relevant to Refractories. *Journal of the American Ceramic Society*, 89(2):638–644, feb 2006.
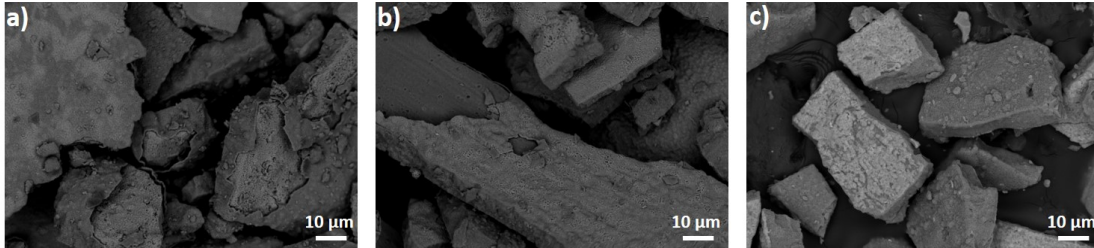
13

Appendix A. Supplemental Material

Figure A.1: SEM micrographs of powdered (a) AlCrN, (b) AlCrSi$_{2.5}$N and (c) AlCrSi$_5$N coatings after the DSC/TG experiments performed at 1260 °C in ambient air.
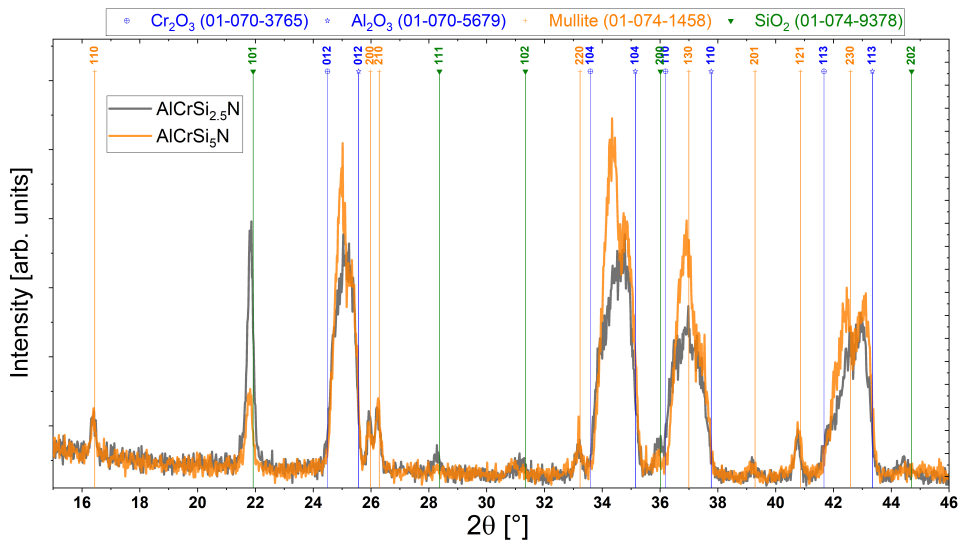

Figure A.2: X-ray diffractograms of the AlCrSi$_{2.5}$N and AlCrSi$_5$N coatings after the DSC/TG experiment (1460 °C in ambient air). The most important peaks of the occurring phases are indexed.

14